IEEE Access
Multidisciplinary | Rapid Review | Open Access Journal

Received March 16, 2020, accepted March 26, 2020, date of publication March 30, 2020, date of current version April 14, 2020.

Digital Object Identifier 10.1109/ACCESS.2020.2984204

A Comprehensive Survey on Millimeter Wave Communications for Fifth-Generation Wireless Networks: Feasibility and Challenges

ANTHONY NGOZICHUKWUKA UWAECHIA AND NOR MUZLIFAH MAHYUDDIN, (Member, IEEE)
School of Electrical and Electronic Engineering, Universiti Sains Malaysia, Nibong Tebal 14300, Malaysia

Corresponding author: Nor Muzlifah Mahyuddin (eemnmuzlifah@usm.my)

This work was supported in part by the Postdoctoral Fellowship Program of the School of Electrical and Electronic Engineering, Universiti Sains Malaysia, Malaysia, and in part by the Ministry of Education Malaysia through the Fundamental Research Grant Scheme under Grant FRGS 203/PELECT/6071373.

ABSTRACT Fifth-generation (5G) cellular networks will almost certainly operate in the high-bandwidth, underutilized millimeter-wave (mmWave) frequency spectrum, which offers the potentiality of high-capacity wireless transmission of multi-gigabit-per-second (Gbps) data rates. Despite the enormous available bandwidth potential, mmWave signal transmissions suffer from fundamental technical challenges like severe path loss, sensitivity to blockage, directivity, and narrow beamwidth, due to its short wavelengths. To effectively support system design and deployment, accurate channel modeling comprising several 5G technologies and scenarios is essential. This survey provides a comprehensive overview of several emerging technologies for 5G systems, such as massive multiple-input multiple-output (MIMO) technologies, multiple access technologies, hybrid analog-digital precoding and combining, non-orthogonal multiple access (NOMA), cell-free massive MIMO, and simultaneous wireless information and power transfer (SWIPT) technologies. These technologies induce distinct propagation characteristics and establish specific requirements on 5G channel modeling. To tackle these challenges, we first provide a survey of existing solutions and standards and discuss the radio-frequency (RF) spectrum and regulatory issues for mmWave communications. Second, we compared existing wireless communication techniques like sub-6-GHz WiFi and sub-6 GHz 4G LTE over mmWave communications which come with benefits comprising narrow beam, high signal quality, large capacity data transmission, and strong detection potential. Third, we describe the fundamental propagation characteristics of the mmWave band and survey the existing channel models for mmWave communications. Fourth, we track evolution and advancements in hybrid beamforming for massive MIMO systems in terms of system models of hybrid precoding architectures, hybrid analog and digital precoding/combining matrices, with the potential antenna configuration scenarios and mmWave channel estimation (CE) techniques. Fifth, we extend the scope of the discussion by including multiple access technologies for mmWave systems such as non-orthogonal multiple access (NOMA) and space-division multiple access (SDMA), with limited RF chains at the base station. Lastly, we explore the integration of SWIPT in mmWave massive MIMO systems, with limited RF chains, to realize spectrally and energy-efficient communications.

INDEX TERMS Millimeter wave communications, propagation, channel measurements, channel models, MIMO, hybrid precoding, non-orthogonal multiple access (NOMA), multiple access techniques, simultaneous wireless information and power transfer (SWIPT), RF energy harvesting.

NOMENCLATURE

2D	Two-dimensional.
3D	Three-dimensional
3GPP	3rd Generation Partnership Project
5G	Fifth Generation
5G-PPP	5G Public-Private Partnership
AGL	Above Ground Level
AoA	Angle of Arrival
ADC	Analog-to-Digital Converter

The associate editor coordinating the review of this manuscript and approving it for publication was Jiayi Zhang.

AoD	Angle of Departure
BER	Bit Error Rate
CBSM	Correlation-based Stochastic Modeling
CE	Channel Estimation
CCA	concentric circular array
CHA	concentric hexagonal array
CIR	Channel Impulse Response
CMRA	concentric multi-ring array
DAC	Digital-to-Analog Converter
EH	Energy Harvesting
EHFs	Extremely High Frequencies
eMBB	Enhanced Mobile Broadband
FCC	Federal Communications Commission
FSL	Free-Space Loss
GBSM	Geometry-based stochastic model.
ID	Information Decoding
IMT-2020	International Mobile Telecommunications 2020
IoT	Internet-of-Things
ITU-R	International Telecommunication Union (ITU) Recommendation
KBSM	Kronecker-Based Stochastic Model
LOS	Line-of-Sight
LTE	Long-Term Evolution
MAC	Medium Access Control
METIS	Mobile and wireless communications Enablers for the Twenty-twenty Information Society
MIMO	Multiple-Input Multiple-Output
MiWEBA	MmWave Evolution for Backhaul and Access
mmWave	Millimeter Wave
mmMAGIC	MmWave Based Mobile Radio Access Network for 5G Integrated Communications
MPCs	Multipath Components
NGSM	Non-geometry based Stochastic Models
NLOS	Non-Line-of-Sight
NOMA	Non-orthogonal Multiple Access
OFDM	Orthogonal Frequency Division Multiplexing
P2MP	Point-to-Multipoint
P2P	Point-to-Point
PL	Path-Loss
PLE	Path-Loss Exponent
PM	Propagation Model
QuaDRiGa	Quasi-Deterministic Radio Channel Generator
RATs	Radio Access Technologies
RF	Radio Frequency
RMS	Root Mean Square
SCM	Spatial Channel Model
SIMO	Single-Input Multiple-Output
SSCM	Statistical Spatial Channel Model
SWIPT	Simultaneous Wireless Information and Power Transfer
TCSL	Time Cluster-Spatial Lobe
TG3c	IEEE Task Group 802.15.3c
TGad	IEEE Task Group 802.11ad
UCA	Uniform Circular Array
UCyA	Uniform Cylindrical Array
UE	User Equipment
ULA	Uniform Linear Array
URA	Uniform Rectangular Array
USA	Uniform Spherical Array
UTD	Uniform Theory of Diffraction
WiGig	Wireless Gigabit
WLAN	Wireless Local Area Networks
WPAN	Wireless Personal Area Networks

I. INTRODUCTION

With the rapid growth of information globalization, like mobile cloud, ultra-high-definition (UHD) 3D video, virtual and augmented realities, internet-of-things (IoT), satellite communications, unmanned aerial vehicle (UAV) [1], has far scaled the capacity of wireless networks with increasing data traffic mainly because of improved area spectral efficiency (bits/s/Hz/m^2) [2]. Besides, satellite communication has recently been introduced as one of the enabling technologies to realize the envisioned 5G backhauling, which will enable new applications such as enhanced mobile broadband (eMBB), massive machine type, and mission-critical services. Recent studies find that data traffic is expected to experience a 1000-fold capacity increase in the coming decade [2], [3] and the microwave band (300 MHz to 3 GHz) where various radio access technologies (RATs) operate cannot provide this capacity demand [4]–[7]. Besides, the ever-increasing demand relies remarkably on spectral efficiency and bandwidth. As the physical layer (i.e., electronic circuit transmission) technology has since reached Shannon's capacity [8], the only unexplored alternative is the system bandwidth. Thus, exploring new less-congested spectrum bands of extremely high frequencies (EHFs) such as the millimeter wave (mmWave) bands (30 − 300 GHz) [6], [9], which corresponds to wavelength from 10 mm to 1 mm is a promising solution to increase network capacity.

Since radio signals are measured by their wavelengths, this implies that mmWave waves are remarkably longer than X-rays or infrared waves, by way of example, but shorter than radio-waves or microwaves [9]. The short wavelengths, narrow beamwidth and high interaction with atmospheric constituents $\left(\text{such as oxygen } (O_2) \text{ and water vapor } (H_2O)\right)$ characteristics of mmWave [1], [5], turns into both benefits and drawbacks. Some of the main benefits include: 1) The decrease in wavelength permits packing a large number of antenna elements into small form factors [2]; 2) Wide bandwidths centred around main carrier frequencies (35, 94, 140 and 220 GHz) [10] provide high data rates (up to 10 Gbps), ultra-low latency of around 1 ms [11], wideband spread-spectrum potential for reduced multipath, clutter, and high resistance to interference and jamming [10]; 3) relatively low atmospheric attenuation in the transmission windows over

moderate path lengths, which potentially support the application of optical sources at specific wavelengths (i.e., 800 nm, 1550 nm and 10 μm) [10], [12]. Some of the mmWave drawbacks include: 1) Manufacturing the small mmWave components requires more precision and hence, increased costs [2], [13], [14]; 2) It encounters low sensitivity in the receiving system resulting from the reduced energy managed by the small antenna size [15]. 3) The range is limited to a few kilometers (i.e., $10 - 20$ km) especially in the 60 GHz, 120 GHz, 180 GHz bands owing to the strong atmospheric absorption with signal attenuation up to 15 dB/km [15], [16]. While bandwidth efficiency is an essential metric in selecting candidate technologies for 5G, energy efficiency has become another significant performance evaluation metric for 5G wireless communication systems with some given bandwidth efficiency constraints [17]. To address these stringent 5G requirements and concurrently manage the energy-efficient design, hybrid precoding for mmWave is envisioned as an essential part of the 5G wireless communication networks.

A. BACKGROUND AND PRIOR WORK

The works of [18]–[22] on mmWave, discuss multi-Gigabit-per-second (Gbps) high-bandwidth communication links, for 5G mobile devices. Thus, the unique mmWave propagation characteristics over the sub-6 GHz bands [18], [20], cause mmWave channels to become more hostile to path-loss and shadowing effects as the frequency increases [23]. Thanks to the extremely short wavelengths of mmWave signals making it feasible to pack a large number of antenna elements into small form factor to enable high-gain beamforming [2], [15]. Beamforming manages increased antenna gain to overcome path loss by adjusting the signal power in the desired directions [2]. Multiple-input multiple-output (MIMO) technology has attracted considerable attention because of its potential to significantly increase data throughput and link range of wireless communications without requiring additional bandwidth or transmit power [1], [17], [24]. Hence, MIMO solutions are essential for mmWave frequencies [25]–[27], since it exploits beamforming gain to establish links with a reasonable signal-to-noise ratio (SNR) to combat path loss and extend the range [2]. Conventional MIMO precoding techniques require a dedicated radio frequency (RF) chain for each antenna element, which becomes impractical to realize with massive MIMO systems in mmWave bands, due to high hardware cost and high power consumption [2], [6], [28]–[30]. Hence, mmWave massive MIMO systems will almost certainly use hybrid precoding (HP) to realize beamforming with few numbers of RF chains to reduce hardware complexity and power consumption [6].

In 2015, the international telecommunication union (ITU) radiocommunication (ITU-R) sector for standards formally called 5G systems as international mobile telecommunications (IMT) 2020 (IMT-2020) [31] and issued recommendation on its framework and explicit description of objectives. Recently, the 3rd Generation Partnership Project (3GPP) has made rapid advancement into the standardization of 5G Phase 1 (i.e., 3GPP Release 15) and have achieved agreements for the 5G Phase 2 (i.e., 3GPP Release 16), which constitutes the IMT-2020 submission [32]. Nonetheless, only limited frequency bands of the proposed Phase 1 specification be open for commercial deployment in 2020 [1], [5]. To plan for spectrum needs, the U.S. federal communications commission (FCC) has repurposed spectrum and authorize its 2016 ''Spectrum Frontiers'' provision of high-band spectrum for use with 5G networks and applications [5]. Specifically, this rulemaking from FCC opens up a total of 10.85 GHz of spectrum, 3.85 GHz for licensed mobile use and 7 GHz for unlicensed use [33]. There are already various standards established for indoor wireless personal area networks (WPAN)/wireless local area networks (WLAN), such as IEEE 802.15.3c [34], IEEE 802.11ad [35], [36], and ECMA-387 [37], [38], which spurs growing interests in (mmWave) outdoor commercial cellular systems. While the mmWave standardization activities for commercial cellular networks are still ongoing, mmWave RATs are currently used for many applications, such for instance radar systems [39], point-to-point (PTP) communication [20], [40], satellite communications (SATCOM) applications [41], [42], radio astronomy [43] and military [44], [45]. Several critical challenges in the physical, medium access control (MAC) and network layers design impede the implementation of mmWave communications networks to full potential [46], [47]. In the physical layer, there have been considerable mmWave propagation campaigns on the 28GHz, 38GHz, 60GHz, and 73GHz bands for indoor and outdoor environments covering both line-of-sight (LOS) and non-line-of-sight (NLOS) scenarios [48]–[55]. The results obtained from these studies show that for mmWave circuit components and antenna designs [15], [56], [57], its high-frequency quadrature modulation/demodulation typically results in extreme distortion, like I/Q imbalances and local oscillator (LO) feedthrough [57]. Concurrently, the mmWave MAC layer for 5G is to be substantially redesigned to take advantage of the highly directional, ultra-low latency end-to-end service demands and high peak rates that are 20 times higher than 4G [58]–[65]. In the meanwhile, concerning the network layer, network coverage can be enhanced via relaying, by implementing a multi-hop routing and relay placement, where most of the current research works have focused [66]–[71]. Research on mmWave communication has been very active in both academia and industry in the past few decades to address the challenges of high-speed communication links and the spatial and temporal characteristics of the mmWave frequency bands. Most of the current research focused on characterizing the sub-100 GHz domain of mmWaves with interest on the 28 GHz band, 38 GHz band, 60 GHz band, and E-band (71 to 76 GHz and 81 to 86 GHz) envisioned to be employed by 5G for mobile cellular; as well as those frequency band around 30, 40, 50, 60, and 93 GHz.

Many other existing survey papers that discussed diverse aspects of mmWave technology have been presented [1], [4], [5], [15], [25], [72]–[80]. The survey work of [74],

performed extensive propagation measurement campaigns at 28 GHz and 38 GHz to better understand the angle of arrival (AoA), angle of departure (AoD), root mean square (RMS) delay spread, path loss, building penetration and reflection characteristics for future mmWave cellular systems design. However, recent topics on mmWave communication, for example, mmWave MIMO, non-orthogonal multiple access (NOMA), hybrid precoding, backhaul technologies and standardization were not addressed in [74]. In [75], a survey is presented based on mmWave propagation measurements at 28 GHz and 73 GHz in New York City with modest assumptions on beamforming. However, topics of mmWave MIMO, NOMA, hybrid precoding, simultaneous wireless information and power transfer (SWIPT) and standardization were not addressed. The survey conducted by [77] covers mmWave propagation characteristics, backhaul networks, channel modeling, and reported on an extensive measurement campaign in the $57-66$ GHz band, $71-76$ GHz band, and $81-86$ GHz band. However, as [77] is a magazine paper, topics like hybrid precoding, SWIPT, multiple access technologies, and mmWave technical aspects were not discussed. These works [7], [79], [80] have introduced valuable insights into the fundamental characteristics of energy harvesting (EH) and SWIPT techniques for mmWave wireless communication systems, as well as remarkable research challenges and recommendations. Yet, [7], [79], [80] focused mainly on mmWave MIMO and other topics like RF wireless power transfer, 5G communications, SWIPT, RF EH and interference exploitation. In [25], a survey is presented based on signal processing for mmWave MIMO systems, discussing the open research problems relating to channel modeling, precoding, receiver design, channel estimation, SWIPT, and broadband channels. Yet, while [25] focused on mmWave MIMO systems, topics regarding the current developments of channel modeling, NOMA, standardization, SWIPT, interference exploitation, RF energy harvesting are missing. The authors in [76], presented a survey addressing mmWave for ultra-dense networks, enhanced local area (eLA) technology, spectrum considerations, channel modeling, air-interface, multiantenna design, and network architecture. However, topics addressing the problems of mmWave MIMO, SWIPT, standardization, NOMA, and hybrid precoding, are not included in [76]. Reference [78] presents a comprehensive overview of mmWave cellular networks, mathematical models, and analytical frameworks based on stochastic geometry. Specifically, [78] utilized results from stochastic geometry to characterize blocking vulnerability and transmitter/receiver directionality. Yet, [78] did not cover topics on SWIPT, hybrid precoding, NOMA, which can further improve both spectral- and energy-efficiency of mmWave massive MIMO systems. Recently, [1] overviewed the technical progress in mmWave communications for mobile networks. Specifically, mmWave channel measurement campaigns, channel modeling, MIMO design, multiple access, performance analysis, backhauling, mmWave standardization, and deployment, were discussed. Yet, [1] did not cover topics on SWIPT, multiple access and standardization. In [5], a survey is presented based on mmWave propagation characteristics and channel modeling involving path loss, LoS probabilities, and building penetration loss and standardization. However, [5] topics on SWIPT, precoding, NOMA, and multiple access were not treated in [5]. In [4], a survey is presented based on extensive measurement campaigns at mmWave frequencies of 28 GHz, 38 GHz, 60 GHz, and 73 GHz on different mmWave channel models, systems design and challenges. However, [4] did not cover topics on SWIPT, precoding, NOMA, RF energy harvesting, and multiple access. The survey conducted by [73] covers topics on mmWave massive MIMO, including precoding, channel estimation, propagation characteristics, standardization, and fronthaul design. Yet, [73] did not cover topics on SWIPT, NOMA, RF energy harvesting and multiple access. Moreover, [15] presented a survey on mmWave communications, with topics mainly on research in the physical layer, MAC layer, network layer, cross-layer optimization, and use cases of mmWave communications. However, [15] did not cover topics on SWIPT, interference exploitation and RF energy harvesting. From the perspective of hybrid beamforming techniques, [72] tracked the development of massive MIMO system models with hybrid beamforming, hybrid transceivers structures, antenna configuration, and hybrid beamforming in heterogeneous wireless networks (HetNET). Yet, topics on NOMA, SWIPT, interference exploitation, and RF energy harvesting, were not discussed in [72]. In [81], a survey is presented based on mmWavw channel modeling requirements, mmWave massive MIMO channel measurements, channel models, and statistical properties. Yet, topics on hybrid precoding, multiple access, NOMA, SWIPT, interference exploitation, and RF energy harvesting, were not discussed in [81]. In [82], a survey that discusses the low-resolution hybrid analog-digital precoding hardware complexity, where it shows the one-bit resolution ADC to be significantly energy efficiency but results in a rate loss, particularly in the high SNR regime. In summary, Table 1 provides a brief comparison of our survey with existing survey papers.

B. PAPER CONTRIBUTION

In this survey, we describe the development and technical content of mmWave emerging technologies, relevant research issues, and challenges, and future directions to realize the energy-efficient and spectrum-efficient 5G and beyond. To the best of the authors' knowledge, a comprehensive survey paper which covers topics on 5G mmWave spectrum and regulatory issues, channel measurements and models incorporating several 5G technologies by different standardization organization, hybrid beamforming architectures, and approaches incorporating SWIPT emerging technologies and its integration with existing mmWave technologies, is still missing. This survey paper proposes to fill this

TABLE 1. A brief comparison of our study with existing survey papers on 5G cellular networks.

Survey Paper	Year	Topics Focused on and elaborated	Topics not discussed
[76]	2014	Conducted mmWave channel measurements campaign at frequencies of 28 GHz and 73 GHz bands.	Topics on mmWave MIMO, NOMA, hybrid precoding, SWIPT, RF energy harvesting and standardization, were not addressed.
[78]	2014	Conducted mmWave measurement campaigns at frequencies of $57-66$ GHz, $71-76$ GHz, and $81-86$ GHz band, mmWave access and backhauling infrastructure, antennas, and modulation schemes.	Topics on hybrid precoding, SWIPT, interference exploitation, RF energy harvesting and mmWave technical aspects, were not addressed.
[77]	2014	Topics discussed are: propagation characteristics and channel models at mmWave frequencies of 28 GHz, 38 GHz, $71-76$ GHz and $81-86$ GHz bands for a 5G eLA.	Topics on mmWave MIMO, SWIPT, interference exploitation, RF energy harvesting, standardization, NOMA, and hybrid precoding, were not discussed.
[25]	2016	Topics discussed are: mmWave MIMO, hybrid analog-digital precodin and channel estimation.	Topics regarding the current developments of channel modeling, NOMA, standardization, SWIPT, interference exploitation, RF energy harvesting, were not discussed
[79]	2016	Topics discussed are: mathematical models and analytical technique in mmWave, mmWave physical challenges, i.e., susceptibility to blocking and strong directionality requirement, large antenna array, hybrid precoding.	Topics on SWIPT, RF energy harvesting, hybrid precoding, NOMA, which can further improve both spectral- and energy-efficiency of mmWave massive MIMO systems, were not discussed.
[83]	2016	Topics discussed are: massive MIMO channels, hybrid precoding and channel estimation	Topics on channel models, channel measurements, standardization, hybrid precoding, multiple access, NOMA, SWIPT, interference exploitation, and RF energy harvesting, were not discussed
[75]	2017	Topics discussed are: channel measurement campaigns and modeling, MIMO transceiver design, multiple access and backhauling, coverage and connectivity, standardization and deployment.	mmWave MIMO, NOMA, hybrid precoding, backhaul technologies and standardization.
[1]	2017	Topics discussed are: mmWave channel measurement campaigns and models, MIMO transceiver design (i.e., MIMO architectures, channel estimation, channel tracking, hybrid precoding and combining), multiple access, backhauls, standardization and deployment.	Topics on SWIPT, RF energy harvesting, multiple access and standardization, were not discussed.
[5]	2017	Topics discussed are: mmWave air interface, propagation models and channel modeling.	Topics on SWIPT, RF energy harvesting, precoding, NOMA, and multiple access, were not discussed.
[4]	2017	MmWave propagation characteristics, channel models available for the 28 GHz, 38 GHz, 60 GHz, and 73 GHz bands, and mmWave system design i.e., system and antenna design considerations for mmWave and link budget of the network.	Topics on SWIPT, precoding, NOMA, RF energy harvesting, and multiple access, were not discussed.
[74]	2017	Topics discussed are: mmWave cellular network technologies, massive MIMO, mmWave massive MIMO system model, precoding, channel estimation, channel measurements and models, cross-layer designs and standardization.	Topics on SWIPT, NOMA, RF energy harvesting, interference exploitation and multiple access were not discussed.
[15]	2018	Topics discussed are: physical layer (i.e., circuit components, beam selection, precoding, MIMO, NOMA, channel model, modulation mode), MAC layer (protocols and scheduling schemes), network layer, cross layer allocation/optimization, mmWave use cases.	Topics on SWIPT, interference exploitation and RF energy harvesting, were not discussed.
[73]	2018	Topics discussed are: hybrid beamforming architecture, hybrid beamforming system model, hybrid beamforming resource management, antenna configuration and the hybrid beamforming in heterogeneous wireless networks (HetNET).	Topics on mmWave frequencies, channel models, massive MIMO, NOMA, SWIPT, interference exploitation, and RF energy harvesting, were not discussed.
[82]	2018	Topics discussed are: mmWave channel modeling requirements, mmWave massive MIMO channel measurements, channel models, and statistical properties.	Topics on hybrid precoding, multiple access, NOMA, SWIPT, interference exploitation, and RF energy harvesting, were not discussed

gap. For reasons of clarity, we summarize the contributions of this survey paper as:

- We provide a brief survey of the radio frequency (RF) spectrum and regulatory issues for 5G mmWave communications, including recent up-to-date developments.
- We compare the sub-6-GHz WiFi and Sub-6 GHz 4G LTE Technologies over mmWave technology.
- We describe the fundamental propagation characteristics of the mmWave band.
- We survey both the fundamental propagation characteristics of mmWaves, and the existing channel models, for mmWave Communications in the literature.
- We describe different hybrid beamforming architectures and approaches, for mmWave MIMO systems, and further discusses multiple-access technologies, channel estimation methods, beam alignment and selection algorithms, and switch based analog architecture for the considered system.
- In spite of the existing SWIPT related articles, limited survey contributions have been introduced for mmWave systems in the direction of presenting a comprehensive review incorporating SWIPT emerging technologies in and its integration with existing mmWave technologies. We present an overview of SWIPT technology, including

its combination with other mmWave technologies, and further discusses the different SWIPT-based receiver architectures.
- Finally, we present various 5G research activities and potential research topics, identifying issues and challenges.

C. PAPER ORGANIZATION

This paper is organized as follows: In Section II, We provide a brief survey of the radio frequency (RF) spectrum and regulatory issues for 5G mmWave communications, including recent developments. Section III compares the sub-6-GHz WiFi and sub-6 GHz 4G long-term evolution (LTE) technologies over mmWave Wireless Gigabit (WiGig). In Section IV, channel propagation characteristics and measurement campaigns, for different potential mmWave bands mainly in the sub-100 GHz band, are discussed. In Section V, channel models for mmWave communications covering several scenarios introduce by different organizations and standards groups, are presented. In Section VI, different hybrid beamforming architectures and approaches, multiple-access technologies, channel estimation methods, beam alignment and selection algorithms, and switch based analog architecture for mmWave MIMO systems, are presented. Section VII presents an overview of SWIPT technology with its integration with other mmWave technologies, and the different receiver architectures utilized in SWIPT. Section VIII identifies challenges, 5G research activities, and potential research topics, and Section IX concludes this survey paper.

D. NOTATION

We use a to denote a scalar, whereas lower- ($\mathbf{a}$) and upper-case boldface ($\mathbf{A}$) letters denote vectors and matrices, respectively. $\emptyset$ denotes the empty set. $\mathbb{C}$ denotes the complex field. We use $\mathbf{h}^H$, $\mathbf{h}^T$ and $\mathbf{h}^{-1}$ to denote the Hermitian transpose, transpose and inverse of $\mathbf{h}$, respectively. $\|\cdot\|$, $\|\cdot\|_2$ and $\mathbb{E}[\cdot]$ denote the absolute value, ℓ_2 norm and statistical expectation, respectively. $|\Omega|$ denotes the number of elements in set Ω. We use $[\mathbf{f}^{\mathrm{RF}}]_i$, $[\mathbf{F}^{\mathrm{RF}}]_{i,:}$, $[\mathbf{F}^{\mathrm{RF}}]_{:,j}$ and $[\mathbf{F}^{\mathrm{RF}}]_{i,j}$ to denote the ith entry of $\mathbf{f}^{\mathrm{RF}}$, the ith row, the jth column, and the entry in the ith row and the jth column of $\mathbf{F}^{\mathrm{RF}}$, respectively.

II. RADIO-FREQUENCY SPECTRUM AND REGULATORY ISSUES

The so-called licensed shared access (LSA) regime influenced in the European Union (EU) has focused on acquiring more spectrum at sub-6 GHz, to make available about 500 MHz of Federal and non-Federal spectrum by 2020 for mobile broadband. This allows third-party the use of underutilized spectrum resources exclusively on a licensed-basis between non-mobile network operator incumbents and a mobile network operator (MNO) sharer under permitted frequency location and time-sharing conditions. Yet, part of the mmWave spectrum from 6 GHz up to 100 GHz (i.e., $\sim$ 94 GHz), where continuous and broad spectra exist, which is substantially higher than those for sub-6 GHz spectrum, has stayed ignored. Enabling the added spectra of future mmWave cellular systems, higher data rates, improved connectivity, and higher system capacity can be realized compared to legacy sub-6 GHz cellular bands [18], [72], [83]–[85]. While oxygen absorption within the 60 GHz spectrum band severely limits range [15], [37], [86], [87], it permits spectrum reuse by multiple systems, which allow a high throughput network. However, shorter wavelength (5 mm at 60 GHz) significantly impacts the form-factor of the 60 GHz system to about 140 times smaller than those at sub-6 GHz, enabling much more compact hardware and making beamforming an attractive proposition. Besides generating mmWave signal in the 60 GHz frequency band, the international telecommunication union (ITU) has designated frequency bands around 60 GHz in different parts of the world [86]. For example, part of the RF spectrum between $28-80$ GHz is being investigated in the United Kingdom (UK) to improve coverage and data transfer [76].

The United States (US) federal communications commission (FCC) led by its Spectrum Frontiers proceedings have interest in the following sub-100 GHz mmWave spectrum bands, which it considers to be of high potential for mmWave technology [33].

- 28 **GHz local multipoint distribution service (LMDS) band** ($27.5--29.5$ **GHz band**): Mainly, LMDS was granted the primary name in the 850 MHz located in the $27.5-28.35$ GHz portion under FCC Part 101 rules and regulations for fixed microwave services. The portion of 150 MHz, that is $29.1-29.25$ GHz in the band is shared on a co-primary basis restricted to LMDS hub-to-subscriber transmission [33].
- 37 **GHz band** ($37-38.6$ **GHz band**): The 37 GHz band consists of 1 GHz of the contiguous, mmWave spectrum at $37.6-38.6$ GHz band, and presently holds no commercial terrestrial wireless incumbent licensees [33].
- 39 **GHz band** ($38.6-40$ **GHz band**): The 39 GHz band consists of 1.4 GHz of the contiguous, mmWave spectrum at $38.6-40$ GHz band [33]. Existing licenses in the 39 GHz band enclose unpaired 50 MHz blocks licensed via partial economic area (PEA), where several licenses do not fit cleanly within the suggested 39 GHz band layout of 100 MHz licenses via PEA, which leads to encumbered licenses. Best suited for backhaul or fixed wireless access. The $39.5-40$ GHz portion of the 39 GHz is currently allocated to the federal fixed-satellite service (FSS) and mobile satellite service (MSS) (space-to-Earth) co-primary basis, limited to space-to-Earth (downlink) operations.
- 60 **GHz Bands** ($57-64$ **GHz and** $64-71$ **GHz (extension)**: The 60 GHz or V-band is very attractive for license-exempt broadband services for high capacity transmissions over short distances [15], [37], [86], [87]. Notably, the 7 GHz of contiguous V-band spectrum, i.e., $57-64$ GHz, provides large capacity than those of the existing broadband spectrum. The Wireless

TABLE 2. Main regulation parameters in Chinese 45 GHz frequency band [88].

Item	Value
Frequency band	$42.3-47.0$ GHz, $47.2-48.4$ GHz
Bandwidth	540 MHz, 1080 MHz
Frequency tolerance	100×10^{-6}
Maximum transmit power at antenna port	20 dBm
Maximum	36 dBm

Gigabit (WiGig) Alliance, also known as IEEE 802.11ad, is standardized for the usage of the 60 GHz unlicensed band in contrast with Wi-Fi 6 and other "traditional" versions of Wi-Fi that employ spectrum in the 2.4GHz or 5GHz bands.

- 70/80 **GHz paired E band** ($71-76$ **GHz and** $81-86$ **GHz bands**): The E-band consists of 10 GHz of the contiguous, mmWave spectrum at $71-76$ GHz and $81-86$ GHz bands on a lightly-licensed basis, and permit the use of smaller antennas for backhauling applications [33].
- 90 **GHz band** ($92-95$ **GHz band**): The 90 GHz band or W-band consists of 3 GHz of the contiguous, mmWave spectrum at $92-95$ GHz band, suitable for very-short-range point-to-point (P2P) and point-to-multipoint (PmP) applications per FCC Part 101 regulations [33].

While we have presented the US FCC regulatory framework, which facilitates the so-called 5G cellular services as an instance, other nations are in the process of making high frequencies available to support the development and adoption of 5G technology.

In 2006, China set aside the $59-64$ GHz frequency band for wireless short-distance technologies [88]. Moreover, spectrum in bands between $40.5-42.3$ GHz and $48.4-50.2$ GHz, were planned in China for fixed point-to-point wireless access system (light license management), while for mobile point-to-point wireless access system (unlicensed management) spectrum in bands between 42.3-47 GHz and $47.2-48.4$ GHz were allocated [88]. In 2010, the Chinese wireless personal access network (CWPAN) standard working group, set up ITU-T Study Group 5 (SG5), also called SG5 QLINKPAN, to investigate the feasibilities of 45 GHz band for WLAN application. In China, the issued 60 GHz consists of 5 GHz of the contiguous, mmWave spectrum at $59-64$ GHz band. To develop the specific standards of 60 GHz and 45 GHz usage in China, IEEE founded the IEEE 802.11aj (45GHz) [88]. However, the already allocated 200 MHz spectrum between 47 GHz and 47.2 GHz band for the amateur radio application based on the ITU regulation, will not be used for 45 GHz unlicensed usage in China [88]. In Table 2, we present the main parameters of China 45 GHz frequency band.

In 2018, South Korea concluded its auction of mmWave 5G spectrum with 2400 MHz bandwidth in the 28 GHz band awarded to three mobile operators [90], [91]. In late 2018, the three national mobile network operators (MNOs) launched 5G services with mobile hotspots in South Korea (SK Telecom, Korea Telecom (KT), and LG UPlus) [89]–[91]. Early 2017, South Korea issued a national broadband plan which suggests the possibility to extend the spectrum in the 28 GHz band by up to 2 GHz to provide access to a total of 3 GHz, $26.5-29.5$ GHz.

The ITU Radio regulations body has allocated frequency bands around 60 GHz, which is the global unlicensed band in different regions of the world. The mmWave bands allocated through ITU Radio regulations are [86]:

- *For fixed and mobile services*: $55.78-66$ GHz, $71-76$ GHz, $81-86$ GHz, $92-94$ GHz and $94.1-100$ GHz.
- *For mobile except aeronautical Mobile*: $64-66$ GHz.

Notably, to secure the right 5G spectrum, significant efforts are required to align allocations among countries. In the meanwhile, countries have similar spectrum allocations in the 28 GHz and 37 GHz and 39 GHz bands. However, around the 60 GHz band, is a global unlicensed band with several subsets of spectrum bands among countries given as follows.

- The mmWave bands allocated by the European Conference of Postal and Telecommunication Administration (CEPT) regularity body, which consists of 46 European spectrum regulators are: $59-66$ GHz (for mobile services), $59-62$ GHz (for radio local area networks (RLANs)), $62-63$ GHz and $63-64$ GHz bands for broadband mobile systems and road transport informatics, and $58.2-59$ GHz and $64-65$ GHz bands for radio astronomy observing program (RAOP) [33].
- The mmWave bands allocated by the spectrum management and telecommunications (Canada) regularity body are: $59-64$ GHz assigned for low power license-exempt devices on non-interferences, non-protection basis [33].
- The mmWave bands allocated by the ministry of public management, home affairs, post and telecommunications (Japan) regularity body are [86]: $59-66$ GHz band for unlicensed utilization and $54.25-59$ GHz band for licensed use.
- The mmWave bands allocated by the Australian communications and media authority (ACMA) regulatory body of the radio frequency spectrum is $59.4-62.9$ GHz band for unlicensed usage [33], [92].

In the mmWave spectrum region, there are still growing interest in utilizing the bands for 5G. Besides, 5G radio emission fields are considerably different compared to legacy 4G generation mobile radio systems [1], [74]. This is mainly due to their complex beamformed transmissions, which further promotes new spectrum issues. The issues include new technology issues like the rulemakings at FCC, to modify specific rules or policies [92]. Specifically, in the rule-making proceeding, decisions based on the allocation of spectrum among different users and technical standards, which include geographical assignments, must be solved in parallel. Thus,

TABLE 3. Comparison of IEEE 802.11 WLAN standards.

WLAN Standard	Traditional IEEE 802.11	IEEE 802.11a	IEEE 802.11b	IEEE 802.11g	IEEE 802.11ad
Year	1997	1999	1999	2003	2013
Operating frequency	2.4 GHz	5 GHz	2.4 GHz	2.4 GHz	60 GHz
Modulation mode	FHSS or DSSS	OFDM	HR-DSSS	OFDM	OFDM or SC
Maximum data rate	2 Mbps	54 Mbps	11 Mbps	54 Mbps	$\approx$ 7 Gbps or 4.6 Gbps

regulators need to balance their objectives in their allocation of 5G spectrum.

III. COMPARISON OF SUB-6-GHz WiFi AND SUB-6 GHz 4G LTE TECHNOLOGIES OVER MILLIMETER WAVE

The sub-6-GHz WiFi and sub-6 GHz 4G Long-Term Evolution (LTE) cellular technologies are among the most appealing technologies in the sub-6 GHz band. MmWave communication is considered indispensable for 5G cellular and mmWave next-generation WLAN technologies [93]. WiFi technologies enable the transfer of data over short distances, such as a room. Increasingly, the need to transfer very high amounts of data extremely quickly arises. Hence, WiGig enables wireless multi-Gbps data rate transmission over the 60GHz band.

A. WiFi VERSUS 60GHz WiFi OR WiGig

WiFi or IEEE 802.11 is part of the IEEE standards that define the form of media access control (MAC) and physical layer (PHY) protocols for realizing wireless local area network (WLAN) [93].

In the meanwhile, there exist several wireless networking specifications in the IEEE 802.11 family:

- **Traditional IEEE 802.11**: The traditional IEEE 802.11 standard for WLAN technology issued in 1997 renders 1-or 2-Mbps transmission in the 2.4-GHz band (2400 − 2483.5 MHz range) employing either the frequency hopping spread spectrum (FHSS) or direct sequence spread spectrum (DSSS) modulation technique in its radio interface [94].
- **IEEE 802.11a**: This standard (issued in 1999) is a revision of the IEEE 802.11 standard, 1997 edition, which deals with WLANs and supports bandwidth up to 54 Mbps in the 5-GHz band using the orthogonal frequency division multiplexing (OFDM) encoding scheme rather than FHSS or DSSS [4], [94].
- **IEEE 802.11b**: This standard is a revision of the traditional IEEE 802.11 standard added in 1999 for WLAN technology and can support up to 11 Mbps transmission in the 2.4-GHz band. The IEEE 802.11b uses the high-rate DSSS (HR-DSSS) encoding scheme in its radio interface. Notably, depending on the signal strength, IEEE 802.11b has a fallback to 5.5, 2, and 1 Mbps [93].
- **IEEE 802.11g**: The IEEE 802.11g standard added in 2003 for WLAN technology can support up to 54 Mbps transmission in the 2.4-GHz band using the OFDM encoding scheme [93].

Rather than designing WiFi for spectrum in the 2.4GHz and 5GHz bands, IEEE 802.11ad (i.e., 60GHz WiFi or WiGig) technology adds 60 GHz frequency mmWave hardware that supports higher data transfer rate −albeit with weaker strength to penetrate walls [93]. Specifically, the 60 GHz Wi-Fi technology exploits the mmWave array antenna beamforming in the unlicensed 57-66 GHz frequency band. Thus, WiGig can support up to 7 GHz or 4.6 GHz transmission using either OFDM or single carrier modulation encoding scheme [4]. In contrast to the legacy Wi-Fi standards, the WiGig standard specification presents a complete makeover in the MAC and PHY layer specifications. In the IEEE 802.11ad standard, the MAC layer now combines beamforming, multi-band operation, and superframe structure architectures [95]. Moreover, the IEEE 802.11ad standard PHY layer, both single carrier (SC) modulation (which supports 4.62 Gbps (π/2-16QAM)) and OFDM modulation (which achieves 6.75 Gbps (64-QAM) maximum PHY throughput rate), have been adopted [96], [97]. The difference in the operating frequency band, modulation modes and maximum data rate for the IEEE 802.11 WLAN standards are summarized in Table 3.

B. 4G LTE VERSUS mmWave CELLULAR NETWORKS

Until recently, the bottleneck between spectrum constraints and capacity requirements of the conventional 4G LTE 20 MHz cellular networks that operate in the sub-6 GHz bands is becoming increasingly evident [4], [9], [13], [76]. Recently, network data communication has experienced rapid growth in wireless data traffic, which has led to explosive congestion in conventional 4G LTE networks, with limited capacity. Specifically, for conventional 4G LTE networks to support the exponential growth in mobile data traffic demand, the throughput per square meter in wireless networks (i.e., network capacity) must be increased. One possible means is by shifting the data transmissions into a new nonconventional spectrum, where huge bandwidths are available [76], namely the mmWave band, which can render multiple order-of-magnitude data rates improvement over 4G LTE. The foremost characteristics of mmWave communications are enormous bandwidth, severe path loss, susceptibility to misalignment of the wireless mmWave link, spatially limited (sparse) scattering environments [2], extensive beamforming, and potentially noise-limited operation. These characteristics establish a significant difference as against legacy 4G LTE networks and are constituting significant technical design challenges that have not been

sufficiently addressed. Based on architectural differences between conventional 4G LTE and mmWave communications technologies [98], mmWave contains several challenges in network, MAC and the PHY layers. *a) PHY Layer:* The transmission loss induced by the mmWave medium is very large, due to its shorter wavelengths than conventional 4G LTE, which constitutes a significant challenge in the mmWave antenna design. However, the appropriation of substrate integrated mmWave antennas installed in base stations is an efficient technique to reduce transmission loss [99]. As a significant ingredient in the PHY layer, entirely different from conventional 4G LTE signals [100], mmWave channels are more sensitive to blockage, directivity, and high propagation loss, particularly prevalent in indoor and dense urban environments, in addition to having highly directional links. However, beneath the premise of obtaining statistical CSI at transmitters, massive MIMO can be exploited in the beam domain to realize high spectrum efficiency and channel capacity for mmWave cellular networks [99]–[101]. On PHY Layer security (PLS), mmWave links are susceptible to wiretapping because the broadcast nature of the beam searching procedure makes the selected beam LOS region of the legitimate UEs easily estimated by an eavesdropper compared to conventional sub-6 GHz communications [99], [100]. However, mmWave precoding (beamforming) affords a beneficial mechanism to enhance wireless PLS and privacy, particularly for medium and long-range outdoor communications. *b) MAC Layer:* Since PHY layer techniques like non-orthogonal multiple access (NOMA) allow multiplexing multiple UEs on the same wireless PHY link, concurrent transmissions scheduling for interference/collision mitigation and capacity improvement techniques are required in the MAC layer [99]–[101]. That is, unlike conventional sub-6 GHz wireless transmissions, mmWave supports more concurrent transmissions because of its narrow beam. Moreover, initial access, mobility management, and handover in mmWave links pose some formidable challenges in cellular networks MAC protocol design induced by its highly directional links, compared to sub-6 GHz networks. *c) Network Layer:* The network layer of mmWave wireless networks needs to manage appropriate routing techniques (based on relay deployment) to mitigate the interference effects among these concurrent links [99]–[101], which furnishes mmWave networks noise-limited unlike conventional interference-limited sub-6 GHz networks.

IV. PROPAGATION CHARACTERISTICS OF MILLIMETER WAVE BAND

Typically, mmWave communication has distinctive fundamental characteristics as the wavelength is considerably shorter than the spectrum in the sub-6 GHz band [31]. Therefore, accurate and reliable knowledge of mmWave channel propagation characteristics is crucial for developing 5G wireless communication systems [4], [5]. Generally, propagation parameters namely, path loss, frequency-dependence material penetration loss, propagation mechanism (i.e., reflection, diffraction, scattering), delay spread, and the effect of rain, foliage, atmosphere, and other attenuation losses are adopted to characterize the radio propagation [4], [5]. These parameters can be acquired mainly by reviewing the measurement data obtained through several channel measurement campaigns conducted in diverse environments. In the following, we present a detail discussion on several mmWave channel measurement campaigns conducted, as well as useful theoretical backgrounds to gain insight on the propagation characteristics.

A. FREE-SPACE LOSS

The free space path loss (FSL) is the attenuation of signal strength between two isotropic radiators[1] in free space, formulated as a power ratio [102]. That is, the loss between two isotropic radiators unaffected by the Earth is termed the FSL and can be determined as follows. Consider a point source and sink with power P_t and P_r, respectively, bounded by a sphere, with a radius d. Let the effective area of the antenna be $\mathcal{A}_d = G\lambda^2/(4\pi)$ with receive power $P_r = \mathcal{A}_d \times (P_t/(4\pi d^2))$. Assuming that the source and sink antennas are isotropic radiators. We have: $G = 1$ (i.e., 0 dB, that is, zero gain and zero loss). If $\lambda = c/f$ is the wavelength, then the power ratio between the source and sink antennas [103], [104], at point d, governed by Friis's Law reads

$$\frac{P_t}{P_r} = \left(\frac{4\pi d}{\lambda}\right)^2 = \left(\frac{4\pi df}{c}\right)^2 = \left(\frac{4\pi}{c}\right)^2 + d^2 + f^2. \quad (1)$$

where c is the speed of light in vacuum (3×10^8 ms^{-1}) and f is the frequency of the radio carrier. Next, converting (1) to decibels. So, we have [31]:

$$10\log\left(\frac{P_t}{P_r}\right) = 10\log\left[\left(\frac{4\pi}{c}\right)^2 + d^2 + f^2\right] \text{dB}. \quad (2)$$

So, the FSL between the source and sink antennas reads

$$\begin{aligned} FSL &= 10\log\left(\frac{P_t}{P_r}\right) \text{dB} \\ &= 20\log\left(\frac{4\pi}{c}\right) + 20\log d_{[m]} + 20\log f_{[Hz]} \\ &= 20\log(4\pi) - 20\log(3\times 10^8) + 20\log d_{[km]} \\ &\quad -20\log 10^3 + 20\log f_{[GHz]} - 20\log 10^9 \\ &= 92.4 + 20\log d_{[km]} + 20\log f_{[GHz]} \text{ dB}. \end{aligned} \quad (3)$$

For a directional transmit antenna with effective area $\mathcal{A}^t_{\text{eff}}$ and gain $G_t = 4\pi\mathcal{A}^t_{\text{eff}}/\lambda^2$, the power ratio between the source and sink antennas [103], [104], at point d reads

$$\frac{P_t}{P_r} = \frac{4\pi d^2}{G_t\mathcal{A}^r_{\text{eff}}} = \frac{\lambda^2\, d^2}{\mathcal{A}^t_{\text{eff}}\mathcal{A}^r_{\text{eff}}} \quad (4)$$

where $\mathcal{A}^r_{\text{eff}}$ is the effective area of the receive antenna. Hence, from (4), we can conclude that, directional antennas have a higher system gain with decreasing wavelength (i.e., at higher

[1] An isotropic radiator is a hypothetical lossless antenna that radiates its energy uniformly in all directions [101].

TABLE 4. Summary of other mmWave rain attenuation measurement campaigns conducted at 0.01% per cent of the time, including potential mmWave cellular communication bands for spectrum mainly in the sub-100 GHz band.

Reference	Frequency	Path length and Location	Rain Rate	Rain-Induced Attenuation
[106]	28 GHz	0.0564 km link at rooftop of the Electrical Engineering Department building in the ITS campus area in Surabaya, Indonesia	∼	4 dB to 36 dB
[114]	28 GHz	0.2 km, 0.4 km, 0.6 km, 0.8 km, and 1 km in Hyderabad, Pakistan.	65 mm/hr	2.2 dB, 4.44 dB, 6.7 dB, 8.8 dB, and 11 dB
[115]	38 GHz	Icheon, Gyeonggi Province, South Korea, where the 3.2 km link is set between Khumdang tower and Icheon tower	50 mm/hr	20.89 dB
[116]	36 GHz and 55 GHz	4.1 km path across central London between Imperial College of Science and Technology and University College London.	12.5 mm/hr	13.8 dB and 14.8 dB
[117]	35 GHz	0.23 km communication link in tropical regions, Ajmer city, India	29 mm/hr	38 dB
[118]	52 GHz, 90.8 GHz	1.008 km link at Massachusetts Institute of Technology, Cambridge	0.3 mm/h to 20 mm/h 0.3 mm/h to 20 mm/h	0.2 dB to 17 dB 0.4 dB to 17 dB

frequencies) [4]. In [105], for a 56.4 m communication link, on the rooftop of Electrical Engineering Department building, Institut Teknologi Sepuluh (ITS), Surabaya, Indonesia, free-pace loss yielded 96.4 dB.

B. RAIN-INDUCED ATTENUATION

Rain attenuation is usually the dominant propagation impairment when dealing with wireless communications signals above 10 GHz operating frequency. The reason is that the size of the raindrops are approximately identical to radio wavelengths at mmWave frequencies and hence induce scattering effect of the signal propagation [31], [106]. Hence, mmWave signals are increasingly risked to blockage by raindrops than sub-6 GHz signals with longer wavelengths. The rain-induced attenuation A(dB) [31], [107], that corresponds to a rainfall rate that surpassed 0.01% of the time is of the form

$$A_{0.01\%[\mathrm{dB}]} = \gamma_{R[\mathrm{dB/km}]} d_{\mathrm{eff}[km]} = \gamma_{R[\mathrm{dB/km}]} d_{[km]} r_{0.01\%} \quad (5)$$

where γ_R denotes the specific attenuation expressed in dB/km, d_{eff} is the effective propagation path length or effective hop length expressed in kilometers. Notably, $d_{\mathrm{eff}} = d_{[km]} r_{0.01\%}$, where d is the real propagation path length and $r_{0.01\%} = 1/(1 + d/d_0)$ is the distance factor. Here, $d_0 = 35 e^{-0.015R}_{0.01\%}$ for $R_{0.01\%} \leq 100$ mm/hr. Consequently, for a given rain rate, R (mm/hr), we can derive specific attenuation utilizing the expression

$$\gamma_{R[\mathrm{dB/km}]} = k R^{\alpha}_{0.01\%} \quad (6)$$

where the regression constants k and α, determined as functions of frequency, $f_{[\mathrm{GHz}]}$ and the polarization type, can be derived from ITU references [31].

In the ITU-R global model for predicting the rain attenuation [31], the specific attenuation of rain rate at 60mm/hr for 200-meter, is observed to be up to 2 dB and 3 dB in 27 GHz and 38 GHz, respectively. In the 26 GHz frequency band of the mmWave spectrum considered in [108] at Universiti Teknologi Malaysia Johor Bahru, Malaysia, the authors find that with rain rate of 120 mm/hr at 0.01%, the specific attenuation observed is up to 26.2 dB/km. A tropical region down-pour where heavy rainfall occurs was considered by [106] with a rate of 50mm/hr, 100mm/hr and 150mm/hr, was observed to have specific attenuation up to 30 dB/km, 60 dB/km and 87 dB/km, respectively at 60 GHz frequency; and up to 7 dB/km, 8 dB/km and 10 dB/km, respectively at 40 GHz frequency. Specifically, the results in [106] show that specific attenuation rises gradually in the 30 GHz to 40 GHz regime, and rapidly in the 40 GHz to 60 GHz regime. In [109], a modified ITU-R rain attenuation model for Earth-to-space is introduced, utilizing the full rainfall rate cumulative distribution and the horizontal path length. Hence, the cumulative distribution of rain-induced attenuation was determined for the tropical and equatorial regions, leading to a better prediction than the ITU-R model. Table 4 summarizes other mmWave rain attenuation measurement campaigns conducted at 0.01% percent of the time, including potential mmWave cellular communication bands for spectrum mainly in the sub-100 GHz band.

C. ATMOSPHERIC-INDUCED ATTENUATION

Atmospheric-induced attenuation is the transmission loss experienced when mmWave signals traversing through the atmosphere are absorbed in the air [31]. Mainly by molecular resonances of oxygen (O_2), water vapor (H_2O) and other gaseous atmospheric constituents occurring at distinct frequencies (O_2 at 60 GHz and 119 GHz and H_2O at 22 GHz and 183 GHz [4], [110]). However, when signals at mmWave frequency change from the resonant frequency, the

atmospheric-induced attenuation decreases distinctly [110], at a rate governed by the air pressure and temperature. While atmospheric absorption at 60 GHz and 119 GHz is dominated mainly by molecular resonances of O_2 gas concentration, atmospheric absorption due to water vapor (i.e., H_2O) becomes the foremost contributor outside the 60 GHz and 119 GHz regimes [4], [31]. Thus, O_2 and H_2O form the most active gaseous absorption in the air for spectrum in bands between 10 GHz to over 100 GHz [31]. While the magnitude of absorption by oxygen is susceptible only to pressure height variation, absorption by water vapor is regulated mainly by temperature.

D. FOLIAGE-INDUCED ATTENUATION

Foliage-induced attenuation is one of the critical impairments in mmWave propagation [111]. According to the ITU-R recommendations [16], [31], [112], the experimental relationship that predicts foliage-induced attenuation γ_{Foliage} (dB) in scenarios with foliage depth less than 400 m is of the form:

$$\gamma_{\text{Foliage}_{[\text{dB}]}} = 0.2 f^{0.3}_{[\text{MHz}]} + D^{0.6}_{[m]}, \quad D < 400m. \tag{7}$$

where f denotes the frequency expressed in megahertz (MHz), and D denotes the foliage depth expressed in meters for $D < 400$ m. Specifically, (7) is viable for spectrum in bands between 200 MHz to over 95, 000 MHz [16]. For instance, the foliage-induced attenuation at 38 GHz for penetration of 12 m is approximately 21 dB. Hence, loss due to foliage is a non-negligible term. In [121], using both co- and cross-polarized antenna configurations, signal attenuation value per unit foliage depth of 0.4 dB/m at 73 GHz was presented. In [122], foliage attenuation at 28 GHz was reported to be 16 dB to 18 dB for bare trees and 26 dB to 28 dB for non-bare trees. In [123], the mmWave measurement campaign conducted at 20 GHz determined signal median attenuation coefficients per unit foliage depth of 4.4 dB/m for the Magnolia tree. The authors in [124], reported attenuation values per unit foliage depth of 1.3 dB/m and 2.0 dB/m at 28 GHz and 57.6 GHz, respectively, for foliage depth within 30m, and attenuation values per unit foliage depth that averages only 0.05 dB/m for foliage depths beyond 30 m. In [125], the mmWave measurement campaign conducted at 38 GHz showed 17-dB foliage attenuation over the thick covering of an oak tree. The authors in [126] conducted measurement campaign at mmWave band at 38 GHz, and reported low attenuation values per unit foliage depth of 2-4 dB/m for a variety of deciduous trees when dry and 6-8 dB/m of the same when wet. Recently, [127] published low attenuation values per unit foliage depth of 0.07 dB/m at 28 GHz.

E. MATERIAL PENETRATION LOSS

Penetration loss at mmWave frequencies may pose a significant challenge over sub-6 GHz frequencies [55], [83]. In the meanwhile, the penetration loss rate depends mainly on the material and rises with an increased spectrum in the mmWave band. In [55], the mmWave measurement campaign conducted at 28 GHz band finds that, compared to indoor building materials that are less reflective, outdoor building materials are better reflectors with the most significant measured reflection coefficient of 0.896 for tinted glass. Moreover, [55] finds that for spectrum in the 28 GHz bands, signal penetration loss through clear glass and tinted glass in different buildings vary around 3.6 dB to 3.9 dB and 20 to 40 dB, respectively. Studies conducted for the spectrum in the 73 GHz band in [83] indicated a similar trend in penetration losses for several general indoor building materials, and presented normalized penetration loss in dB/cm. In [128], continuous wave signal probes adopted to measure signal penetration loss at 9.6, 28.8, and 57.6 GHz on several outdoor building materials, show that the penetration loss was small for clear glass but increased by 25 to 50 dB for metal coating materials. Unfortunately, external building glass is frequently compounded or tinted with metal to block visible light and ultraviolet rays to improve the heat-insulating properties. Thus, mmWave signal degradation increases with increasing penetration loss. Table 5 compares measurement campaign results of mmWave material penetration loss, conducted for different materials in different environments.

F. RADIO CHANNEL PROPAGATION MECHANISMS

The main NLOS propagation mechanisms may generally be attributed mainly to reflection, diffraction and scattering [130]. Generally, for the NLOS path between the transmitter and the receiver, the signals can still propagate to the receiver through reflections from the receiver's proximity objects or through bending or diffraction [16]. Diffraction and scattering result when the obstructing object is large compared to the wavelength of the radio wave [16], [130]. Thus, mmWave signals with short wavelengths are exposed more to shadowing and reflection [16], since the extremely short wavelengths result in low diffraction. Let us consider a transmitter and receiver array antennas positioned to communicate with each other, as shown in Fig. 1. While the specular reflection of transmitted signal obeys Snell's law of refraction, other transmitted signals are called diffuse reflections [131]. In Fig. 1, mmWave signal reflection results in higher diffusion of the signal with less specular reflection due to shorter

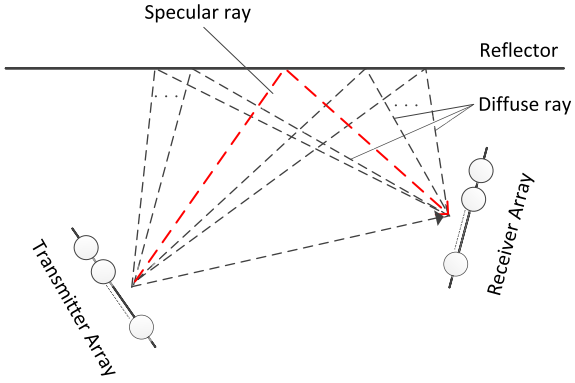

FIGURE 1. Short wavelength (i.e. high frequencies) of mmWave signals make the reflecting material to seem relatively rougher, which yield greater diffusion of the signal and less specular or direct reflection [132].

TABLE 5. Comparison of other mmWave material penetration loss measurement campaigns, conducted for different materials in different environments.

Reference	Frequency GHz	Environment	Material under Test (MUT)	Penetration Loss
[119]	45	Indoor	Concrete slab	4.38 dB/cm (H-H), 4.64 dB/cm (V-V)
	45	Indoor	Solid wood	2.42 dB/cm (H-H), 4.19 dB/cm (V-V)
[56]	28	Outdoor -Othmer Residence Hall, Brooklyn	Tinted Glass	40.1 dB,
	28	Outdoor -Warren Weaver Hall, Manhattan	Brick	28.3 dB,
	28	Indoor - MetroTech Center, Brooklyn	Clear Glass	3.9 dB,
	28	Indoor - Warren Weaver Hall, Manhattan	Tinted Glass	24.5 dB,
	28	Indoor - Warren Weaver Hall, Manhattan	Clear Glass	3.6 dB
	28	Indoor - Warren Weaver Hall, Manhattan	Wall	6.8 dB
[120]	60	Indoor- structures of an office building	glass door	2 dB
	60	Indoor- structures of an office building	plasterboard wall with metallic studs	9 dB,
	60	Indoor- structures of an office building	metal-backed blackboard	35.5 dB
[121]	26	Indoor- KeySight office, Beijing	Wooden door of the laboratory	5.50 dB
	26	Indoor- KeySight office, Beijing	Transparent glass door of the hall	3.95 dB
	26	Indoor- KeySight office, Beijing	Frosted glass door of the small office	4.10 dB
	26	Indoor- KeySight office, Beijing	Wooden door of the cabinet	4.16 dB
	39	Indoor- KeySight office, Beijing	Wooden door of the laboratory	9.69 dB
	39	Indoor- KeySight office, Beijing	Transparent glass door of the hall	4.59 dB
	39	Indoor- KeySight office, Beijing	Frosted glass door of the small office	4.65 dB
	39	Indoor- KeySight office, Beijing	Wooden door of the cabinet	5.59 dB
[90]	73	Indoor office environments, 9th floor.	Glass door	5.1 dB (V-V), 23.4 dB (V-H)
	73	Indoor office environments, 9th floor.	Clear Glass	7.1 dB (V-V), 18.3 (V-H)
	73	Indoor office environments, 9th floor.	Wall	10.6 dB (V-V), 11.7 dB (V-H)
	73	Indoor office environments, 9th floor.	Closet Door	32.3 dB (V-V), 16.3 dB (V-H)
	73	Indoor office environments, 9th floor.	Steel Door	52.2 dB (V-V), 48.3 dB (V-H)
	73	Indoor office environments, 9th floor.	Whiteboard Writing Walls	73.8 dB (V-V), 58.1 dB (V-H)
[130]	73	Indoor NYU wireless research center	Clear Glass	7.72 dB (6.43 dB/cm) (V-V)
	73	Indoor NYU wireless research center	Clear Glass	7.75 dB (6.46 dB/cm) (V-H)

wavelengths [16], [31]. Thus, diffuse reflections translate into less received transmission power than with specular reflections [16], [31], [130]–[132]. That is, while diffraction contributes to the received power for sub-6 GHz communication channels, its contribution is negligible in wireless communication channels operating in the mmWave frequency bands [16], [131]. Multiple measurement campaigns for mmWave communication were conducted to explore the propagation mechanisms at different mmWave frequencies [49], [55], [133]. Studies conducted by [49] for the spectrum in the 60 GHz band found that reflected multipath distribution is strongly correlated mainly with the propagation environment. In [133], omnidirectional models at 83.5 GHz were provided mainly for indoor environments, from 3000 measurements in LOS and NLOS conditions up to a range of 160 m. However, under NLOS in [133], no direct path was detected resulting from high penetration loss, while the diffracted paths detected resulted in $11 - 23$ dB weaker transmission power than the reflected paths.

Generally, parameters, like path loss, delay spread, shadowing (shadow-fading), and angular spread are employed mainly for radio propagation characterization. This can be achieved primarily through investigating the FSPL, rain-induced attenuation, atmospheric-induced attenuation, foliage-induced attenuation, material penetration loss, and radio-channel propagation mechanisms data collected by several channel measurement campaigns, in various environments. We describe these parameters in the following:

1) LARGE-SCALE PROPAGATION EFFECTS: PATH LOSS AND SHADOW FADING

Path loss, expressed in decibel (dB), describes a deterioration in power density of any transmitted electromagnetic wave as it propagates through space [134]. However, shadowing occurs mainly in NLOS scenarios resulting from obstacles and thus, permits significant attenuation of signal strength [135].

2) POWER DELAY PROFILE AND DELAY SPREAD

The power delay profile (PDP) provides the statistical power distribution of a received signal over a multipath channel as a function of propagation delays. While the delay spread gives the propagation time difference between the longest and shortest path with significant energy. Hence PDP and delay spread are also essential parameters that characterize mmWave radio propagation.

Table 6 summarizes for comparison typical path loss, shadowing and delay spread measurement campaign results for spectrum in the mmWave bands.

G. OTHER PROPAGATION FACTORS

The Doppler effect is likewise a significant factor that can affect mmWave communication, which is known to be $15 - 30$ times higher at $28 - 60$ GHz (being directly proportional to carrier frequency) compared to the sub-6GHz communication systems [338]. The mmWave cellular communication has two foremost characteristics compared to the sub-6 GHz wireless communication links. Firstly, the application of directive antennas —at least at one link end; and secondly, the much higher maximum Doppler shift. The authors in [339], nonetheless, present theoretically that directional antennas, envisioned for mmWave communications, serve as spatial filters. In [339], the investigation of the behavior of Doppler shift and Doppler spread and consequently the time-selectivity has been demonstrated to be significantly

TABLE 6. Comparison of typical path loss, shadowing and delay spread measurement campaign results reported for spectrum in the mmWave bands.

Ref.	Frequency (GHz)	Antenna Directionality	Tx Antenna	RX Antenna	Path Loss Exponent		Shadowing (dB)		Delay Spread (ns)
					LoS	NLoS	LoS	NLoS	
[86]	28	Omnidirectional	TX antenna height of 7 m; 17 m above ground level (AGL)	RX antenna at a height of 1.5 m AGL	2.1	3.4	3.6	9.7	–
[49]	38	Directional	Steerable 25-dBi TX	Steerable 13-dBi TX	2.13	2.54	8.14	7.74	10.1
	38	Directional	Steerable 25-dBi TX	Steerable 13-dBi TX	2.16	2.52	8.78	7.82	17.3
	38	Directional	Steerable 25-dBi TX	Steerable 13-dBi TX	2.03	2.40	5.31	5.27	4.8
	38	Directional	Steerable 25-dBi TX	Steerable 13-dBi TX	2.74	2.97	12.46	11.16	17.5
	38	Directional	Steerable 25-dBi TX	Steerable 25-dBi TX	2.25	3.29	6.51	11.63	13.5
	38	Directional	Steerable 25-dBi TX	Steerable 25-dBi TX	2.38	3.20	14.12	8.97	15.1
	38	Directional	Steerable 25-dBi TX	Steerable 25-dBi TX	2.01	2.70	6.56	5.54	5.3
[137]	73	–	TX antenna at 110 m AGL	RX antenna height between 1.6 m and 2 m AGL	2.16	2.75	1.7	6.7	–
[86]	73	Omnidirectional	TX antenna 7m; 17m AGL	RX antenna 4.06 m AGL	2.0	3.5	4.2	7.9	–
	73	Omnidirectional	TX antenna 7m; 17m AGL	RX antenna 2 m AGL	2.0	3.3	5.2	7.6	–
	73	Omnidirectional	TX antenna 7m; 17m AGL	RX antenna 2 m; 4.06m AGL	2.0	3.4	4.8	7.9	–
[138]	28	directional V-V	TX height was established at 2 m AGL	RX antenna was fixed at 1.5 m AGL	0.92	2.58	2.18	4.62	–
	28	directional V-H	TX height was established at 2 m AGL	RX antenna was fixed at 1.5 m AGL	0.90	2.33	3.25	4.76	
	28	omnidirectional V-Omni	TX height was established at 2 m AGL	RX antenna was fixed at 1.5 m AGL	1.07	3.85	4.35	4.85	
[138]	38	directional V-V	TX height was established at 2 m AGL	RX antenna was fixed at 1.5 m AGL	2.30	4.23	5.62	4.08	–
	38	directional V-H	TX height was established at 2 m AGL	RX antenna was fixed at 1.5 m AGL	2.24	4.53	6.64	3.69	
	38	omnidirectional V-Omni	TX height was established at 2 m AGL	RX antenna was fixed at 1.5 m AGL	2.40	4.55	3.78	2.58	
[54]	28	directional V-V	TX antenna height at 2.5 m AGL	RX antenna was fixed at 1.5 m AGL	1.7	4.4	2.5	11.6	17.3/17.7
	28	directional V-H	TX antenna height at 2.5 m AGL	RX antenna was fixed at 1.5 m AGL	4.1	5.1	8.0	10.9	17.2/18.0
[54]	73	directional V-V	TX antenna height at 2.5 m AGL	RX antenna was fixed at 1.5 m AGL	1.6	5.3	3.2	15.7	12.8/12.3
	73	directional V-H	TX antenna height at 2.5 m AGL	RX antenna was fixed at 1.5 m AGL	4.7	6.4	8.6	15.9	11.4/8.4
[139]	32	Directional	TX antenna height of 5 m (8 m) AGL	RX antenna at 1.7 m AGL	1.81 (1.94)	-	3.77 (3.38)	-	–
[139]	39	Directional	TX antenna height of 5 m (8 m) AGL	RX antenna at 1.7 m AGL	1.8 (1.91)	-	3.61 (3.16)	-	–

reduced by directional beamforming. Such analytical results can considerably expedite robust waveforms and air interface design toward Dopplar impairments.

H. SUMMARY

We summarize the current essential details from these channel measurement Campaigns in the mmWave band as follows: 1) The high penetration- and energy- losses ascribed to scattering for spectrum in the mmWave band results in more attenuation on NLOS paths and a remarkable difference in the path loss exponent (PLE) between NLoS and LOS mmWave band than the sub-6GHz band. This suggests that modeling mmWave NLOS paths require different considerations than the sub-6GHz band. 2) Reflection and scattering are more dominant NLOS conditions in the mmWave bands than diffraction due to the shorter wavelength. 3) Based on extensive experimentation in indoor [49]–[52], [139] and outdoor [48], [86] settings, results reveal that mmWave channels are sparse [2] in the angular (i.e., AoA/AoD) and delay domain based on their high propagation loss, directivity, and

sensitivity to blockage [140], [141]. That is, the channel is usually a LOS channel with few dominant path clusters. 4) In the mmWave band, the propagation loss and channel delay-spread typically decrease for increasing signal frequencies because of the shorter wavelengths of energy to be scattered or attenuated [4].

V. CHANNEL MODELS FOR mmWave COMMUNICATIONS

In this section, several typical antenna configurations for massive MIMO design is first introduced. Then, the classification of mmWave massive MIMO channel models is presented, which are in accordance with either theoretical analysis or practical evaluation. Next, we discus the narrowband and wideband mmWave channel models.

A. ANTENNA ARRAY CONFIGURATION

In conventional passive antenna array, the RF circuit is typically linked to its physical antennas via an RF cable [142]. To subdue the loss induced by the RF cable and save maintenance/installation costs, a remote radio unit (RRU) in combination with a baseband unit (BBU) has become preferred configurations [17], [142]. The generated digital baseband signals at the BBU, are transmitted to RRUs over optical fiber fronthauls. The physical massive MIMO antenna array is mainly integrated as close as practicable with RF circuit front ends. Moreover, active antenna systems, which integrate active radio transceiver with the passive antenna array into one circuit board to boost capacity and coverage, reduce RF cable requirements and cable loss. Hence, this configuration has become a preferred component of 5G.

Notably, the array geometries that have been studied in the literature for practical massive MIMO system designs include uniform linear arrays (ULAs), uniform rectangular arrays (URAs), uniform circular arrays (UCAs), uniform spherical arrays (USAs), uniform cylindrical arrays (UCyAs) and distributed antenna arrays [142], [143]. A Linear antenna array consists of similar antenna elements arranged in a straight line, which produces a beam that can be modified by adjusting some parameters like excitation amplitude, inter-element spacing, and excitation phase of each element [142], [143]. The broadside linear antenna array of isotropic elements produces a broad pattern, in a plane perpendicular to the array axis, and a narrow pattern in the plane of the antenna array. The ULA possesses superior directivity and can generate the narrowest main-lobe in any specific direction. However, ULAs can not function equally well in all azimuthal (horizontal) directions. Linear antenna array design has been studied primarily in the literature [144]–[146], by employing different optimization algorithms. These works [144]–[146] employ the particle swarm optimization, ant colony optimization, and biogeography-based optimization, respectively, for maximum sidelobe level reduction and null placement. Whereas the USAs, UCAs, UCyAs, and URAs are in the form of 2D antenna arrays, which can steer the beam in the 3D space, and more potentially employed in practical systems [142]. A potential drawback regarding the URA is the extra major lobe of equal intensity, which surfaces on the opposite side [142], [147]. An evident superiority emerges from the symmetry of the UCA structure. That is, as UCA antennas go without edge elements, directional patterns formed using UCAs, can be rotated[2] electronically in the array plane with no substantial change in either the beamwidth or the sidelobe level [148]. Compared with the URA geometry, the experiments conducted on the planar UCA geometry with similar areas, demonstrate that planer UCA realizes slightly higher directivity [147], [149]. Conversely, the circular array can be regarded typically as a high side-lobe (in the far-field radiation pattern) antenna configuration. If we reduce the sidelobes by reducing the inter-element distance, the mutual coupling effect becomes increasingly significant [147]. For lowering the circular array high side-lobe levels, the concentric multi-ring array (CMRA) with sufficient inter-element distance is often mainly employed [147]. Specifically, CMRA geometries can be arranged either as concentric circular arrays (CCAs) with concentric circular rings [150] or concentric hexagonal arrays (CHAs) [151], [152], to obtain low sidelobe radiation and highly directive pencil beam pattern. Experimental results of distributed antenna arrays were first reported and presented in [153], as an improved user separation capability under the indoor LOS scenario. The work in [153] finds that if the entire array is partitioned and distributed as subarrays parallel to the line connecting the users, the refined AoAs received from the distributed array increases the channel degrees of freedom and improve the user separation. Thus, array configurations determine the mutual coupling and correlation matrix, which defines systems performance [142]. For instance, reducing the inter-element spacing between the antenna terminals induces signal correlation and mutual coupling, which leads to a reduced capacity of massive MIMO channels [142].

B. CLASSIFICATION OF mmWave MASSIVE MIMO CHANNEL MODELS

Channel model represents the propagation characteristics of signals in radio environments and used for evaluating the performances of wireless communication systems [142]. To successfully support mmWave system design and deployment, accurate channel modeling is essential [1], [5], [20], [74], [78], [81]. The bases for modeling several types of wireless propagation channels have yielded an extensive number of different modeling techniques proposed in the literature [154]–[162]. Owing to the high-dimensional antenna arrays in massive MIMO channels, the multiple signal paths between the transmitter/receiver and the cluster may be smaller compared to the Rayleigh distance. Consequently, the system does not properly realize the far-field condition. In that case, the effect of the spherical wavefront is vital and should be considered rather than the conventional plane wavefront [81]. Furthermore, massive MIMO channels are

[2]Steering the beam through 360° in azimuth.

mainly characterized via their spatial non-stationarity [81]. That is, each antenna element on the array may observe different sets of clusters, which is not characterized in conventional MIMO channels [81], [142]. Since path parameters such as power and delay may drift across separate antennas, this needs to be accurately addressed, when modeling massive MIMO channels. Generally, channel modeling methods can be split mainly into two main categories, that is, analytical and physical channel models [163].

1) **Physical Channel Models**. Physical channel models (PCMs) depict an environment by characterizing the radio path linking the transmitter and receiver. PCMs particularly model wave propagation parameters such as DoD, DoA, complex amplitude and delay. Generally, physical channel modeling methods can be split basically into two classes namely, stochastic and deterministic models [1], [4], [87].
   - **Deterministic Modeling**. The deterministic modeling method is based on the theory of electromagnetic (EM) wave propagation. Hence, environmental-specific parameters are used to model the propagation channel [154]. This method can be split further into the following:
     - **Closed-Form approach**: Notably, the two-path signal model in [134], is a straightforward closed-form modeling approach which enables theoretical and analytical investigation for several communication designs. Yet, this method is likewise, conservative in describing the realistic channel model environment under consideration;
     - **Empirical approach**. In the empirical-based deterministic modeling approach, channel parameters are extracted from environmental-specific measurement campaign data collected under study. This approach renders more accurate channel propagation characteristics, but with increased data complexity. Several empirical models for the mmWave spectrum, mainly in the 60 GHz band for example, have been introduced in [155]–[159];
     - **Ray-tracing-based deterministic modeling**. The ray-based solvers use the uniform theory of diffraction (UTD) and finite-difference time-domain (FD-TD) to realize ray-tracing based deterministic models, use to predict the realistic behaviour of the electromagnetic wave along the ray path [164]–[166] and simulate power loss and shadowing effects. In [167], a 28 GHz channel model for urban outdoor environments in Ottawa and Chicago based on 3D ray-tracing simulations, is proposed, where parameters of the radio channel, like delay spread, angular spread, shadowing variance and path loss exponent are determined. Several other ray tracing models for the mmWave spectrum, mainly in the 60 GHz band for example, have been introduced in [168]–[171]. Some of the ray-tracing based mmWave channel simulators include: WinProp [172], which supports simulations for frequency up to 75 GHz, Ranplan Professional [173], which supports simulation in the frequency range 100 MHz to 70 GHz,
   - **Stochastic Modeling**. In the stochastic channel modeling approach, the propagation characteristics are obtained mainly via the channel statistics without having the specific location prior knowledge [154]. This approach can also be classified mainly as geometry-based stochastic models (GBSMs) and non-geometry based stochastic models (NGSMs), presented in the following:
     - **Geometry-based stochastic modeling (GBSM)**. GBSMs in [174] and [175] were introduced based on predefined stochastic distribution of effective scatterers by employing geometric information, namely, angles of departure and arrival, and delay. While the GBSM approach can be adapted straightforwardly to diverse scenarios by adjusting the scattering region shape, only single and double scattering effects require to be simulated, which reduces their complexity [176]. The GBSMs [31], [176]–[180] can be split mainly into regular-shaped GBSMs (RS-GBSM) (such as one-ring, two-ring, and ellipse models) or irregular shaped GBSMs (IS-GBSMs).
     - **Nongeometrical stochastic models (NGSMs)**. NGSMs statistically characterize the physical channel parameters, such as the number of scatterers, shadowing, path loss, AoD, DoA, and delay spread, without reference to any geometric assumptions [181]. The NGSMs can also be categorized mainly into two broad types. *a) The extended Saleh-Valenzuela model* [182], [183]: The existing Saleh-Valenzuela model, introduced in [184], utilizes clusters of multipath components (MPCs) (i.e., employing exponential decay profiles) and generally termed the extended Saleh-Valenzuela model [163], as it generalizes the temporal cluster Saleh-Valenzuela model developed in [184]. Specifically, the Saleh-Valenzuela model has mainly been extended to the spatial domain in [182], [183], and exploits angular domain information (i.e., AoA) in the channel model of [184] (adopting uniform, Laplacian, or Gaussian profiles). *b) Zwick Model*: The work in [185] demonstrates that for the indoor multipath channel, clustering and multipath fading are unlikely for sufficiently high sampling rates. Specifically, Zwick

models characterize the multipath propagation channel independently without both amplitude fading and clustering [163].

2) **Analytical Channel Models**. Generally, analytical channel modeling methods can be split broadly into two main categories, that is, correlation-based stochastic modeling (CBSM) and propagation models (PM).

- **Correlation-based stochastic modeling (CBSM)**. The CBSMs are employed primarily for evaluating the theoretical performance of massive MIMO channels [142]. CBSM has lower computational complexity than GBSM [142] but relatively simplistic, and therefore, inaccurate for modeling realistic massive MIMO channels that encounter a spherical wavefront. The CBSMs can be split mainly into three types, namely, non-dispersive independent identically distributed (i.i.d.) Rayleigh fading model, non-dispersive correlated channel models, and the dispersive multipath-channel (MPC) model.
  - **Non-dispersive i.i.d. Rayleigh fading model**. This model assumes that all the channel links are uncorrelated [87]. Therefore, the elements of the fast-fading channel matrix are i.i.d. Gaussian variables;
  - **Non-dispersive Correlated channel models**. While it has been widely applied mainly to characterize the Doppler-induced received signal correlation for massive MIMO channels due to its simplicity, unrealistic results regarding channel capacity have resulted in applying this basic model. Examples of this model include the Weichselberger model [84] and the Kronecker-based stochastic model [186]. The so-called Kronecker-based stochastic model was used in [187]–[190] for capacity analysis;
  - **Dispersive MPC model**. The dispersive MPC model of massive MIMO channel can support multiple distributions of the azimuth angles of arrival (AoA) (i.e., multiple independent paths) arriving from the different user equipment (UE) [17]. The characterization of each independent path is achieved mainly via a path attenuation times the steering vector of an AoA. Thus, UEs located at diverse angular positions can be separated mainly based on their AoAs, and therefore, the performances of the inter-user interference (IUI) or Intercell Interference (ICI) can be analyzed.
- **Propagation Models (PMs)**. PMs characterizes the MIMO channel matrix via propagation parameters, such as the virtual channel representation model [191], maximum entropy model [192], and finite scatterer model [193].

Generally, the analytical channel models can generate channel impulse responses (CIRs) from the scattering geometry. Nonetheless, obtaining values of probability distribution parameters and validating the models utilizing channel measurement campaigns, is still crucial.

C. EXISTING MASSIVE MIMO CHANNEL MODELS

Existing massive MIMO channel models are premised on the GBSMs and extended with additional attributes, namely, spherical wavefront and array non-stationarity. The works of [194], [195], [196] and [197] introduced massive MIMO channel models premised on a twin-cluster channel model, a multi-ring channel model, a twin-multi-ring channel model, and an ellipse channel model, respectively. Notably, on the array axis of the antenna elements, the birth-death process is adapted to characterize the cluster appearance and disappearance. While spherical wavefront is applied to determine the distances separating every transceiver element and clusters, the parameter drifts across the array were calculated as a function of the geometry. Recently, GBSM introduced in European WINNER I and II projects are based on the rules of 3GPP/3GPP2 spatial channel model (SCM) [198], which supports the extended-SCM (ESCM) [199] and COST 259 [200]. WINNER I and II models are represented mainly in deliverables D5.4 [201] and D1.1.2 [202], respectively. More recently, the WINNER II model has evolved in the WINNER+ project [203]. As a significant enhancement in [204], the 2D WINNER-type massive MIMO channel model, is introduced. Specifically, the cluster generation/recombination terms are realized mainly by adopting a two-state Markov process, while the spatial log-normal method was employed to implement smooth power variations. Moreover, in [204], a second-order approximation to the spherical wavefront (i.e., parabolic wavefront), is proposed resulting in linear drifts of the angles of MPCs and non-stationarity over the array, reducing theoretical and computational complexity compared to spherical wavefronts. The work in [205] extended the spherical wavefront (i.e., parabolic wavefront) in [204], into the 3D space and time domain to capture spatial-temporal non-stationary properties of the channel efficiently. Moreover, a 3D extension of the Riemann sum method in [206] for parameter computation has been introduced and validated through simulations. Recently, [207] also introduced a WINNER-type massive MIMO channel model different from [204].

The mmWave massive MIMO channel model is different from the conventional channel model in the following ways. Firstly, the non-stationary property is observed mainly in the antenna array of massive MIMO [197], which implies that different antenna elements can see different scatters, and the closer the two antennas are set, the more common scatterers they share [208], [209]. In that case, the conventional MIMO channel model cannot be extended straightforwardly to massive MIMO channel models, due to the non-stationary property of clusters on both the array and time axes. Hence, a model that can be consistent with the general conventional

MIMO standards, is required [208]. Secondly, the mmWave massive MIMO channel model can be realized more realistically in a three-dimension (3D) space [210]. Thirdly, massive MIMO arrays need to consider the effect of the spherical wavefront [81]. While [204] modeled the array non-stationarity by adopting a two-state Markov process, [207] modeled the array non-stationarity by segmenting the base station array into multiple sub-arrays for which clusters, are independently generated. Moreover, the size of the sub-array is delimited mainly by the stationarity distance, that is, correlation or coherence distance in terms of visible clusters. Besides, the Quasi Deterministic Radio Channel Generator (QuaDRiGa) model, which was initially introduced by [160], acts as the Winner-type GBSM reference model over which the extensions in [207], were derived. However, to ensure multi-user consistency, adjacent sub-arrays auras[3] can typically overlap to generate a gradual share of the clusters, which remains an open issue in [207]. In [211] and [212], massive MIMO channel models based on measurement campaigns for both outdoor and indoor environments, were proposed adopting the COST 2100 channel model developed in [213] as a general framework. Moreover, the included extensions in [211] and [212] of the COST 2100 [213] channel model, are 3D propagation polarization properties, cluster behavior model, and MPC gain functions. Notably, in [211] and [212], the array non-stationarity were modeled mainly by proposing two visibility regions: 1) mobile station visible region (MS-VR), which operates on the temporal domain, and 2) base station visible region (BS-VR), which operates on the array domain. Thus, both are employed to determine channel statistics and spherical wavefront. In [208], a two-cylinder GBSM model in a 3D space is proposed to characterize the non-stationarity of massive MIMO channels rather than using a 2D visibility region of the antenna array or a birth-death process. Specifically, in [208], a 3D two-cylinder regular-shaped GBSM, for non-isotropic scattering massive MIMO channels, is introduced. The 3D MIMO non-stationary GBSM was modeled mainly by allocating a 3D visible area for each antenna (to establish its own set of scatters), determined using a virtual sphere centered at each radiating antenna element. While GBSMs designs realistic massive MIMO channels, CBSMs is considered mainly for theoretical analysis of massive MIMO channel and used to analyze the proposed models of [214] and [215], theoretically. The authors in [216] designed a Kronecker-based stochastic model (KBSM) scheme for capacity analysis of massive MIMO channels by adapting the birth-death process on the array axis. The birth-death process is abstracted mainly via a survival probability matrix, whose rows are values from exponential functions. Thus, the birth-death process on the array axis decreases correlations between antennas, since antennas in a massive MIMO array may perceive diverse sets of scatterers. Instead of applying the i.i.d assumption which may over-simplify the channel model, a KBSM with LOS components were assumed in [217], for capacity analysis of massive MIMO channels. In [84], a joint correlation at both the transmitter and receiver was introduced primarily in the Weichselberger massive MIMO channel model. In [218], an empirical, measurement-based massive MIMO channel matrix model is introduced, by first characterizing the channel matrix as the sum of fixed and random matrices. And then, modeling the channel matrix by using the mutual coupling in the transmitting/receiving antenna arrays and correlation due to the non-richness of scatterings along the channels.

Apart from the stochastic channel modeling, a ray-tracing-based deterministic model is introduced in [219], to characterize massive MIMO channels for system performance evaluation. A time-reversal beamforming scheme was first introduced mainly to target the desired users dynamically. Then, convenient weights were applied to the emitted signals to improve the practical signal level for beamforming and time-focusing gains. To characterize the electromagnetic behavior of trees on ray-tracing based simulation platforms, the authors in [220] proposed 2D ray-tracing simulation model with appropriate tree models and compared the results with the measured results in an anechoic chamber. Specifically, this proposed 2D ray-tracing simulation model employs several point scatterers with specific radiation properties to characterize the effect propagation paths obstructed by trees. However, since the anechoic chamber describes a specific environment than the entire real world, the experimental measurements cannot correctly analyze the effect of trees on outdoor ray-tracing simulations. Moreover, to analyze the blockage effect of roadside trees, 2D ray-tracing simulation-based techniques are ill-suited for depicting the 3D structure of roadside trees correctly [221]. In [221], the influence of roadside tree trunks which are typical environment objects in an urban environment was modeled mainly by cylinders and propagation characteristics calculated based on UTD and added in 3D ray-tracing simulations. However, the results were analysed exclusively in limited perspectives, with no detailed channel analysis presented. Besides, in [221], roadside tree trunks were modeled mainly employing simple cylindrical shapes, making them inflexible in diverse real-world applications. To analyze the effects of including roadside tree trunks in simulating wireless channel behavior employing 3D ray tracing, the authors in [222], model roadside trees as objects transmitting, reflecting, and diffracting electromagnetic waves and included to 3D ray-tracing simulation. The model results of simulations are then compared mainly with experimental results measured employing a channel sounder in several areas, which improves prediction accuracy in modeling mmWave channels.

D. RECENT mmWave CHANNEL MODELING EFFORTS

To provide background knowledge, we present some of the recent channel modeling attempts for the mmWave system.

[3]The circle surrounding the user implies the user aura, where the stationarity interval determines its radius. Thus, the overlap between auras describes the common clusters share among users.

1) COST 2100 CHANNEL MODEL [213]

The COST 2100 channel model can be categorized primarily as GBSMs, which originates from the earlier COST 259 [244] and COST 273 [245] channel model frameworks. Specifically, the COST 259 channel model was the foremost GSCM for multiantenna base stations [213], while the COST 273 model subsequently addressed full MIMO systems. Therefore, the COST 2100 channel model extends the COST 273 model to support multi-user, multi-cellular, and cooperative technologies without requiring a paradigm shift in the COST 273 modeling basis [213]. Moreover, the COST 2100 channel model uses visibility regions and is cluster-based, which is not constrained by large-scale parameters (i.e., global delay and angular spreads), and the environment is characterized mainly independently of the UE location. Using visibility regions (i.e., of BSs from each UE) leads to a more practical evaluation of multi-cell transmission and heterogeneous transmission.

2) MmWave EVOLUTION FOR BACKHAUL AND ACCESS (MiWEBA) CHANNEL MODEL [246]

To further improve the development of mmWave communications for 5G cellular, the European Union's 5G public-private partnership (5G-PPP) initiative have introduced the MiWEBA project, based mainly on a measurement campaign conducted at 60 GHz frequency band. Hence, MiWEBA channel model, a quasi-deterministic channel model, can support the mmWave spectrum between 57 GHz and 66 GHz band and aim mainly for mmWave outdoor mobile access links [247]. Specifically, the MiWEBA quasi-deterministic channel model combines a geometry-based scheme for a limited number of MPCs and a stochastic method [247]. Thus, spatial consistency is inherently in the MiWEBA model as a limited number of MPCs is calculated deterministically compared to pure statistical models. The MiWEBA channel model supports mmWave massive MIMO communications and beamforming. However, the quasi-deterministic modeling technique requires an accurate description of the scenario; thus, only applicable to the specific scenario investigated and cannot be extended primarily to other scenarios [247].

3) QUASI-DETERMINISTIC RADIO CHANNEL GENERATOR (QuaDRiGa) [160]

The QuaDRiGa is a 3D geometry-based stochastic channel model developed mainly to enable the modeling of MIMO channels for specific network configurations [248], namely indoor, satellite or heterogeneous-based configurations. Here, 3D propagation implies antenna modeling, geometric polarization and scattering clusters. QuaDRiGa can support the mmWave spectrum between 0.45 GHz and 100 GHz band and inherently provide spatial consistency mainly by correlation of large-scale parameters and small-scale parameters. QuaDRiGa channel model stems from the 3GPP spatial channel model−extension (SCME) and WINNER channel models as well as new modeling methods which implement characteristics to support quasi-deterministic receiver-movement-multi-link tracking in changing environments [248]. Specifically, QuaDRiGa channel model assumes fixed BS and scattering clusters, moving UE, and deterministic radio channel time evolution. QuaDRiGa channel model is backed up by measurement campaign conducted at 10/28/43/60/82 GHz frequency band by the Fraunhofer Heinrich Hertz Institute (HHI) based on [249]. Typically, using the multi-bounce scattering model and spherical wave propagation, massive MIMO modeling is supported. The QuaDRiGa channel model is calibrated based on TR 36.873 [32] and TR 36.901 [249].

4) 5GCM-SIG CHANNEL MODEL [252]

Special interest group (SIG) which constitutes of diverse technical and academic institutes, introduced the 5G channel model (5GCM), namely 5GCM-SIG. Notably, 5GCM-SIG builds on extensive measurements and ray-tracing over frequency bands from 6 GHz to 100 GHz [252] incorporating new channel characteristics such as blockage, spatial consistency, support of large bandwidth and array, and new path loss models [254]. The 5GCM-SIG channel model has continuously developed from the narrowband channel representation of [174] to the state-of-the-art wideband mmWave channel models of [192], [228], [231], [232], [234] and [225]. 5GCM furnishes two LOS probability models characterize for mmWave. 1) 5GCM furnishes two LOS probability models characterize for mmWave. 1) the 5G 3GPP (TR 38.901)-like channel models for outdoor [162], namely, the d_1/d_2 model, except with somewhat diverse curve-fit parameters for d_1 and d_2. 2) NYU (squared) model developed by NYU [253], which enhances the efficiency of the d_1/d_2 model. The d_1/d_2 and NYU (squared) 5GCM LOS probability models, respectively in the urban microcell (UMi) environment [5] are presented in the following two equations.

$$P_{\mathrm{LOS}}(d_{2D}) = \min\left(\frac{d_1}{d_{2D}}, 1\right)\left(1-\exp\left(-\frac{d_{2D}}{d_2}\right)\right) + \exp\left(-\frac{d_{2D}}{d_2}\right), \quad d_1 = 20m,\ d_2 = 39m \tag{8}$$

$$P_{\mathrm{LOS}}(d_{2D}) = \left[\min\left(\frac{d_1}{d_{2D}}, 1\right)\left(1-\exp\left(-\frac{d_{2D}}{d_2}\right)\right) + \exp\left(-\frac{d_{2D}}{d_2}\right)\right]^2, \quad d_1 = 22m,\ d_2 = 100m \tag{9}$$

where d_{2D} is the 2D transmit-receiver Euclidean distance, with d_1 and d_2 as curve-fit parameters. While the 5GCM LOS probability model in an indoor hotspot environment gives

$$P_{\mathrm{LOS}} = \begin{cases} 1, & d_{2D} \le 1.2m \\ \exp\left(-\dfrac{(d_{2D}-1.2)}{4.7}\right) & \\ \qquad 1.2m < d_{2D} < 6.5m & \\ \exp\left(-\dfrac{(d_{2D}-6.5)}{32.6}\right) \times 0.32 & 6.5m \le d_{2D} \end{cases} \tag{10}$$

5) MmWave BASED MOBILE RADIO ACCESS NETWORK FOR 5G INTEGRATED COMMUNICATIONS (mmMAGIC) CHANNEL MODEL [250]

The mmMAGIC channel model stems from the 3GPP/ITU-R 3D channel modeling framework [249] and adopts the QuaDRiGa as a basis. Extensive radio channel measurement campaigns in the mmMAGIC project have been conducted mainly for different scenarios in multiple frequency bands, yielding a reliable basis for model extension and parameterization [250]. Notably, the mmMAGIC channel model is a statistical channel model for the link- and system-level simulations [1] and supports mmWave channel for the frequency range of 6-100 GHz and can robustly predict the time variance of the channel. The mmMAGIC channel model provides significant improvements concerning 1) the impact of ground reflection and blockage effects, 2) spatial consistency (i.e., assuming the radio environment conditions of close-by UE, are correlated), and 3) outdoor-to-indoor penetration loss modeling. The mmMAGIC LOS probability models in the UMi environment for indoor UEs and outdoor UEs, respectively are presented in the following equations.

$$P_{\mathrm{LOS}}(d_{2D}) = \min\left(\frac{d_1}{d_{2D}}, 1\right)\left(1 - \exp\left(-\frac{d_{2D}}{d_2}\right)\right) + \exp\left(-\frac{d_{2D}}{d_2}\right), \tag{11}$$

and

$$P_{\mathrm{LOS}}(d'_{2D}) = \left[\min\left(\frac{d_1}{d'_{2D}}, 1\right)\left(1 - \exp\left(-\frac{d'_{2D}}{d_2}\right)\right) + \exp\left(-\frac{d'_{2D}}{d_2}\right)\right]^2, \tag{12}$$

where $d_1 = 20\ m$ and $d_2 = 39\ m$ in both (11) and (12), and d'_{2D} denotes the distance between the indoor building surface and the BS, d_{2D} is the 2D transmit-receiver Euclidean distance, with d_1 and d_2 as curve-fit parameters. While the mmMAGIC LOS probability model in an indoor hotspot environment gives

$$P_{\mathrm{LOS}} = \begin{cases} 1, & d_{2D} \le 1.2m \\ \exp(-\dfrac{(d_{2D} - 1.2)}{4.7}) & 1.2m < d_{2D} < 6.5m \\ \exp(-\dfrac{(d_{2D} - 6.5)}{32.6}) \times 0.32 & 6.5m \le d_{2D} \end{cases} \tag{13}$$

6) METIS CHANNEL MODEL

5G channel model needs to consider the distribution of scatterers in the environment, to generate channels with reasonable spatial consistency. Hence, the Mobile and wireless communications Enablers for the Twenty-twenty Information Society (METIS) project [161] proposed a mmWave channel model for spectrum at 60 GHz band, by combining the geometric locations of the scatterers related to the first and last hops of each path in spatial channel models. Thus, this consequently enables an initial map-based ray-tracing model setting, where a simple geometry-based method is adopted to predict scatterer locations from the map of an environment [251]. The METIS channel model takes the form of a map-based (deterministic) model, stochastic model, or a hybrid model that is a combination of deterministic and stochastic modelling principles [1]. According to the well-defined propagation theories [161], [162], [164]–[166], the map-based model based on ray-tracing, can simulate well the deterministic, physics-based propagation mechanisms, given a simplified 3D geometric description of the propagation environment. These propagation mechanisms include penetration, diffraction, specular reflection, diffuse scattering and blocking. Hence, the METIS channel models realized with the implementation of the map-based ray-tracing models are inherently site-specific (or deterministic) to generate generic MIMO channel models for outdoor. Therefore, it is essential to develop measurement-based channel models that include the scatterers linked along paths estimated via MIMO channel sounding in real environments. The METIS stochastic channel model extends the GSCM, which has also been realized typically from WINNER/3GPP [161], to implement low complexity multi-dimensional shadowing maps, mmWave parameters, direct sampling of the angular power spectrum, and frequency-dependent path loss models [1], [161]. The METIS hybrid channel model attempts to balance between realism and complexity in the simulations via rendering scalable and flexible channel modeling structure. The METIS channel models can support the mmWave spectrum between sub-1 GHz and 86 GHz. The METIS LOS probability models in the UMi environment for indoor UEs and outdoor UEs are presented in the following equations, respectively as

$$P_{\mathrm{LOS}}(d_{2D}) = \min\left(\frac{d_1}{d_{2D}}, 1\right)\left(1 - \exp\left(-\frac{d_{2D}}{d_2}\right)\right) + \exp\left(-\frac{d_{2D}}{d_2}\right), \tag{14}$$

and

$$P_{\mathrm{LOS}}(d'_{2D}) = \left[\min\left(\frac{d_1}{d'_{2D}}, 1\right)\left(1 - \exp\left(-\frac{d'_{2D}}{d_2}\right)\right) + \exp\left(-\frac{d'_{2D}}{d_2}\right)\right]^2, \tag{15}$$

where $d_1 = 18\ m$, $d_2 = 36\ m$, and $10m \le d_{2\mathrm{D}}$ in both (14) and (15), and d'_{2D} denotes the distance between the indoor building surface and the BS, d_{2D} is the 2D transmit-receiver Euclidean distance, with d_1 and d_2 as curve-fit parameters.

7) 3GPP-mmWave CHANNEL MODEL TECHNICAL REPORT (TR) 38.901 [162]

MIMO approaches adapted to exploit the 3D spatial dimensions (azimuth and elevation) are often required to be an essential air-interface improvement technique critical in enhancing the spectral efficiency of the wireless link. Hence, the 3GPP has lately realized a 3D channel model to aid the implementation and evaluation of such MIMO approaches.

The fact is that the elevation channel characteristics are typically not captured by the existing 2D channel models, which makes them deficient for such investigations. The 3GPP TR 38.900 3D channel model extends the 3GPP channel model TR 36.873, to support frequency bands from 6 to 100 GHz, over different scenarios like urban macro, urban micro, device-to-device communication and indoor. Specifically, this model adds the generation of elevation angles utilizing a distance-dependent elevation spread. We note here that the 3GPP TR channel model designs are a nonstop ongoing work and suffice as the global industry standard that governs 5G cellular. Recently, 3GPP channel model TR 38.901 proposed in [162], extends the 3GPP channel model TR 38.900, to devise channel models designated for the frequency range from 0.5-100 GHz with bandwidth of up to 2 GHz. Notably, the 3GPP standards channel models of TR 38.900 and TR 38.901 characterize clustered delay line and tapped delay line as mmWave channel modeling methodologies for link-level simulation. The METIS channel models can support the mmWave spectrum between sub-1 GHz and 86 GHz. The 3GPP TR 38.901 LOS probability models in the UMi environment for indoor UEs and outdoor UEs, respectively are presented in the following equations, respectively as

$$P_{\mathrm{LOS}}(d_{2D}) = \min\left(\frac{d_1}{d_{2D}}, 1\right)\left(1 - \exp\left(-\frac{d_{2D}}{d_2}\right)\right) + \exp\left(-\frac{d_{2D}}{d_2}\right), \tag{16}$$

and

$$P_{\mathrm{LOS}}(d'_{2D}) = \left[\min\left(\frac{d_1}{d'_{2D}}, 1\right)\left(1 - \exp\left(-\frac{d'_{2D}}{d_2}\right)\right) + \exp\left(-\frac{d'_{2D}}{d_2}\right)\right]^2, \tag{17}$$

where $d_1 = 18\ m$ and $d_2 = 36\ m$ in both (16) and (17), and d'_{2D} denotes the distance between the indoor building surface and the BS, d_{2D} is the 2D transmit-receiver Euclidean distance, with d_1 and d_2 as curve-fit parameters.

8) IEEE 802.11ay CHANNEL MODEL [255]

The IEEE 802.11ay channel model is an extension of the existing IEEE 802.11ad channel model in the 60GHz band, with new scenarios (mostly outdoor) and use cases (i.e., usage models with SU-MIMO and MU-MIMO modes), that require new strategies to the mmWave channel model [255], [256]. Notably, the mmWave IEEE 802.11ay channel model is premised mainly on the quasi-deterministic methodology which exploits hybrid deterministic-stochastic characterization of the environment [255], [256]. Thus, achieved using the simple realization of scenario-specific geometric properties, ray blockage and mobility effects, reflection attenuation, in addition to the proper MIMO channel models for outdoor mmWave hotspots [246], [255], [256]. Contrary to existing point-to-point link-layer models, the IEEE 802.11ay channel model now supports full-scale system-level modeling, with mobility support.

9) INTERNATIONAL MOBILE TELECOMMUNICATIONS-2020 (IMT-2020) CHANNEL MODEL [257]

To fulfil the requirements of evaluating the candidate radio interface technologies for IMT-2020, the IMT-2020 channel model [257], is developed to support more realistic modeling of radio wave propagation in different radio propagation environments. Specifically, this involves supporting mmWave spectrum up to 100 GHz band with large bandwidth, supporting massive MIMO array, blockage modelling, 3D modelling, and spatial consistency [257]. While the 2D mmWave model only describes the azimuth angle channel propagation characteristics, the 3D channel model considers the elevation angle influence by describing the channel propagation characteristics more precisely both in azimuth and elevation dimensions. Moreover, spatial consistency of channel ensures that the channel evolves smoothly without discontinuities when the transmitter and/or receiver moves or turns [257], [258]. That is, closely located links have highly correlated channel characteristics, i.e., same base station observing two close-by UEs. Additionally, the sufficiently high resolution in both delay and AoA domains achieved by IMT-2020 channel model support the evaluation of large bandwidth and mmWave massive MIMO array.

E. NARROWBAND mmWave MASSIVE MIMO CHANNEL MODEL

In narrowband mmWave MIMO channel models, the path loss is characterized mainly as the amount of decay in the received power at a particular (carrier) frequency [223]. On account of insufficient measurements, such as obtaining relative propagation times from different angular directions, the seminal work of [174] developed a narrowband statistical mmWave channel model for the cluster power fractions and angular/spatial characteristics following the 3GPP/ITU MIMO model specification. However, the channel model in [174], which is based primarily on real experimental data collected at 28- and 73- GHz band is solely narrowband, in that the model neglects to account for frequency selectivity or multipath propagation time delays. Specifically, if there are n_{rx} receive antennas and n_{tx} transmit antennas, the narrowband time-varying channel gain between a transmit-receiver antenna pair depicts the mmWave channel matrix as [174]

$$\mathbf{H}(t) = \frac{1}{\sqrt{L}} \sum_{k=0}^{K} \sum_{l=0}^{L_k} g_{kl}(t) u_{rx}(\theta_{kl}^{rx}, \phi_{kl}^{rx}) u_{tx}^{H}(\theta_{kl}^{tx}, \phi_{kl}^{tx}) \tag{18}$$

where K and L_k denote the number of clusters and the number of rays within the kth cluster, respectively. $g_{kl}(t)$ denotes the instantaneous gain on the lth ray of the kth cluster, $u_{rx}(\theta_{kl}^{rx}, \phi_{kl}^{rx}) \in \mathbb{C}^{n_{rx}}$ and $u_{tx}^{H}(\theta_{kl}^{tx}, \phi_{kl}^{tx}) \in \mathbb{C}^{n_{tx}}$ represent the receive and transmit array response vectors, where $\theta_{kl}^{rx}(\theta_{kl}^{tx})$

and ϕ_{kl}^{rx} (ϕ_{kl}^{tx}) refers to azimuth and elevation angles of arrival and departure (AoAs and AoDs), respectively. By utilizing the values of mean and RMS angular spreads, the wrapped Gaussian distribution is employed mainly to model the AoA and the AoD [174], [224]. Since the multipath parameters, such as the spatial correlation of channel gains/rays in [174] is influenced primarily by the transmit and receive antenna array geometries (i.e., uniform linear arrays (ULA), uniform rectangular arrays (URA) and uniform circular arrays (UCA)), then the so-called narrowband clustered channel model in [174] with few dominant paths can thus be termed a geometry dependent model.

Recently, various propagation measurement campaigns have been conducted to investigate frequency selectivity or multipath propagation time delays (i.e., angular statistics on both the channel tap and cluster levels), to model wideband mmWave massive MIMO channels presented in the following.

F. WIDEBAND mmWave MASSIVE MIMO CHANNEL MODEL

In wideband mmWave massive MIMO channel models, the path loss is characterized mainly from the power of MPCs, which carries the joint effects of time dispersion and attenuation [223]. Based on extensive wideband mmWave channel measurements over 28-, 38-, 60- and 73-GHz bands, a 3GPP-type mmWave channel model termed statistical spatial channel model (SSCM) was developed in [225]–[232] utilizing the time cluster-spatial lobe (TCSL) technique for urban LOS and NLOS scenarios. This technique extends the existing UHF 3GPP model by the introduced model parameters of directional RMS lobe angular spreads for spatial lobes. Specifically, the SSCM can be described by a double-directional CIR, of the superposition MPCs premised on the 3GPP model. The omnidirectional CIR $h_{\text{omni}}(t, \overrightarrow{\Theta}, \overrightarrow{\Phi})$ is expressed as [225], [230]

$$h_{\text{omni}}(t, \overrightarrow{\Theta}, \overrightarrow{\Phi}) = \sum_{n=1}^{N}\sum_{m=1}^{M_n} a_{m,n} e^{j\varphi_{m,n}\cdot\delta(t-\tau_{m,n})} \cdot\delta(\overrightarrow{\Theta} - \overrightarrow{\Theta}_{m,n}) \cdot \delta(\overrightarrow{\Phi} - \overrightarrow{\Phi}_{m,n}) \quad (19)$$

where t is the absolute propagation time, $\overrightarrow{\Theta} = (\theta, \phi)_{\text{TX}}$ denotes the vector of azimuth and elevation AODs, $\overrightarrow{\Phi} = (\theta, \phi)_{\text{RX}}$ denotes the vector of azimuth and elevation AOAs; N and M_n denote the number of time cluster and cluster subpaths, respectively. $a_{m,n}$ is the complex amplitude of the mth subpath belonging to the nth time cluster, $\overrightarrow{\Theta}_{m,n}$ and $\overrightarrow{\Phi}_{m,n}$ denote the azimuth/elevation AODs and azimuth/elevation AOAs, respectively [225], [230], of each MPC. We notice that $h_{\text{omni}}(t, \overrightarrow{\Theta}, \overrightarrow{\Phi})$ can moreover be decomposed to form directional power delay profiles at a desired transmit-receive (TX-RX) antenna single best antenna pointing angle, and for arbitrary transmit-receive antenna design [225], [230], as follows

$$h_{\text{dir}}(t, \overrightarrow{\Theta}_{\text{des}}, \overrightarrow{\Phi}_{\text{des}}) = \sum_{n=1}^{N}\sum_{m=1}^{M_n} a_{m,n} e^{j\varphi_{m,n}\cdot\delta(t-\tau_{m,n})} \cdot g_{\text{TX}}(\overrightarrow{\Theta}_{\text{des}} - \overrightarrow{\Theta}_{m,n}) \cdot g_{\text{RX}}(\overrightarrow{\Phi}_{\text{des}} - \overrightarrow{\Phi}_{m,n}). \quad (20)$$

In (20), the desired transmit-receive antenna pointing angle are denoted as $(\overrightarrow{\Theta}_{\text{des}}, \overrightarrow{\Phi}_{\text{des}})$, while g_{TX} and g_{RX} are the global patterns of TX and RX antennas, respectively. We find that modern 3GPP and WINNER [198], [202] models assume that, a joint delay-angle probability density function characterizes clusters. Whereby, a cluster of traversing multipath link must be assigned a unique AOD-AOA angle combination centered about a mean propagation delay. Similarly, methods based on a 3D SSCM for mmWave, are introduced in [233]–[235], based on both mmWave wideband measurement results and ray-tracing and the corresponding channel models following the 3GPP methodology/WINNER models. Statistical characteristics of the channels, like delay and angular spreads, were obtained, and the RMS delay spread calculated via the power delay profiles from both the measurement data and the ray-tracing results. However, remarkable features of the mmWave channel model, such as the dynamic shadow fading model, and blocking model comprises human blockage, remain as future works that can be modeled mainly as an additional module.

Based on the clustering results, a number of statistical (e.g. stochastic) 60 GHz channel models parameters can be derived. One of the most widely used channel models based on clusters is the Saleh-Valenzuela model introduced in [236], which presents a simple statistical multipath model for indoor radio channels. The basic principle of the model arises from observations from indoor mmWave measurement campaigns that multipath components arrive in clusters, and that the cluster and MPCs within each cluster follow Poisson processes with different rates [237]. Specifically, the Saleh-Valenzuela model is premised mainly on the clustering of MPCs observed in the measurement data. The CIR based on S-V model, $h_{\text{sv}}(t)$, is expressed as follow

$$h_{\text{sv}}(t) = \sum_{k=0}^{K}\sum_{l=0}^{L_k} \beta_{kl}(t) e^{j\vartheta_{kl}} \delta(t - T_k - \tau_{kl}) \quad (21)$$

where k, l, K and L_k denote the cluster number, MPC number in the kth cluster, total number of clusters and total number of MPCs, respectively. $\delta(\cdot)$ denotes the Dirac delta function, g_{kl} denotes the multipath tap gain of the lth MPC in the kth cluster, τ_{kl} and T_k denote the arrival time of the lth MPC in the kth cluster and the arrival time of the kth cluster, respectively. These parameters of the Saleh-Valenzuela model can be addressed primarily as virtually time-invariant random variables. β_{kl} and ϑ_{kl} are the gain and uniformly distributed phase of the lth MPC in the kth cluster. Accordingly, the mean square value of β_{kl} reads [238]

$$\overline{\beta_{kl}^2} = \overline{\beta_{00}^2} e^{-T_k/\Omega} e^{-\tau_{kl}/\Lambda} \quad (22)$$

where $\overline{\beta_{00}^2}$ denotes the average power gain of the first MPC in the first cluster, and Ω and Λ are exponential power-decay constants for the clusters and MPCs, respectively. T_k and τ_{kl} in (21) and (22) are characterized via employing the probability function as [237], [238]

$$p(T_k \setminus T_{k-1}) = \Gamma e^{-\Gamma(T_k - T_{k-1})}, \quad k > 0 \tag{23}$$

and

$$p(\tau_{kl} \setminus \tau_{kl(l-1)}) = \lambda e^{-\lambda(\tau_{kl} - \tau_{kl(l-1)})} \quad l > 0 \tag{24}$$

where Γ and λ denote the cluster and MPC arrival rates, respectively. To characterize a propagation environment utilizing the Saleh-Valenzuela channel model requires the following propagation parameters, i.e., the cluster arrival rate, Γ ; cluster decay constant, Ω; MPC arrival rate, λ; and MPC decay constant, Λ. Consequently, the estimation of the parameter set $\boldsymbol{\Theta} = (\Gamma, \Omega, \lambda, \Lambda)$ is employed to calibrate the Saleh-Valenzuela model [237].

The IEEE 802.15.3c and 802.11ad, standard channel models [239] have been proposed for 60-GHz indoor wireless communications and are based on the extended Saleh-Valenzuela model [236], [240], [241]. Within the IEEE, two notable task groups are currently leading the way: IEEE 802.15.3c (IEEE Task Group 802.15.3c, i.e., TG3c) on 60 GHz WPAN and 802.11ad (IEEE Task Group 802.11ad, i.e., TGad) on 60 GHz WLAN. Notably, IEEE 802.15.3c (TG3c) is a single-input multiple-output (SIMO) channel model which only characterizes the AoA in azimuth domain [239]. At the same time, IEEE 802.11ad (TGad) is a MIMO channel model that characterizes the double-directional angle properties [243]. Specifically, the Saleh-Valenzuela Model was extended mainly to MIMO channels. Thus, the extended S-V model reads:

$$h(t, \theta^{\mathrm{rx}}, \theta^{\mathrm{tx}}) = \frac{1}{\sqrt{LK}} \sum_{k=0}^{K} \sum_{l=0}^{L_k} \beta_{kl}(t) e^{j\vartheta_{kl}} \delta(t - T_k - \tau_{kl}) \cdot \delta(\theta^{\mathrm{rx}} - \Phi_k^{\mathrm{rx}} - \varphi_{kl}^{\mathrm{rx}}) \delta(\theta^{\mathrm{tx}} - \Omega_k^{\mathrm{tx}} - \omega_{kl}^{\mathrm{tx}}) \tag{25}$$

where β_{kl} is the complex amplitude of the lth MPC in the kth cluster, T_k is the delay, Φ_k^{rx} and Ω_k^{tx} are the mean receive and transmit cluster arrival angles, respectively. Similarly, τ_{kl}, $\varphi_{kl}^{\mathrm{rx}}$ and $\omega_{kl}^{\mathrm{tx}}$ are the delay and the relative receive and transmit angles for the lth MPC in the kth cluster, respectively. The underlying assumption of the extended Saleh-Valenzuela model is that the delay and angular domains can be independently modeled. However, in mmWave MIMO systems, this assumption might not be valid for 60 GHz channels [243], due to the MPC decay and the large K-factor for the MPCs. Here, the K-factor is expressed primarily as $K(\mathrm{dB}) = 10\log_{10}(P_{\mathrm{LOS}}/P_{\mathrm{NLOS}})$ [134], where P_{LOS} is the MPC and P_{NLOS} is the power from multipath scatterers.

G. SUMMARY OF mmWave MASSIVE MIMO CHANNELS

The antenna configuration directly influences the characteristics of mmWave massive MIMO channels. We find

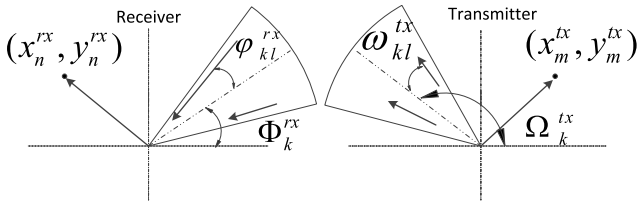

FIGURE 2. The extended Saleh-Valenzuela model parameters for a single cluster [242].

that linear antenna array induces both non-stationary channel characteristics in array domain and near-field effects. In contrast, the rectangular, spherical and cylindrical antenna array geometries more accurately steer the beam propagation in the 3D space. Hence, an array antenna design is a fundamental issue for mmWave massive MIMO systems. Two stochastic modelling techniques, namely, GBSMs and CBSMs, have been generally employed to simulate mmWave Massive MIMO channels. While GBSMs are generally used to model massive MIMO channel, they are mathematically tractable and relatively straightforward to fit measured data. Moreover, they are likewise independent of the arrangement (or design) of antenna arrays. Several antenna settings can be modeled employing GBSMs. Specifically, GBSMs model each cluster in the scattering environment according to its geometry relationships. Notably, CBSMs are analytical channel models employed primarily to analyze the theoretical performances of mmWave massive MIMO channels based on its simplicity.

Non-stationary property is known to be unique propagation characteristics which make massive MIMO channels different from conventional MIMO channels. Generally, the non-stationary property consists of two features: AOA shifts at the receiver side and dynamic characteristics of clusters on both the time and array axes for the massive MIMO channel model. Typically, employing spherical wave-front assumption, AOA shifts can be characterized entirely based on geometrical relationships linking the transmit antennas, receive antennas and clusters. Typically, dynamic characteristics of clusters on both the array and time axes imply that antennas at distinct physical location possess different cluster sets that vary over time. Most importantly, the non-stationary property on both the time and array axes is characterized mainly by birth-death process and cluster visibility region technique.

Furthermore, we present several research contributions that have proposed mmWave channel models for carrier frequencies up to 100 GHz. Channel model which can capture mmWave massive MIMO channel characteristics is essential to design and evaluate 5G systems. Some of the massive MIMO channels specific characteristics include spherical wavefront and cluster appearance and disappearance that can occur on both the array and time axes. However, traditional channel models like 3GPP SCM, the WINNER II, WINNER+, 3GPP 3D SCM, and COST 2100 channel models are unable to support these emerging 5G requirements appropriately. Since the impacts of cluster evolution and the

spherical wavefront assumption is vital compared to plane wavefront assumption adopted in conventional MIMO channel, the COST 2100 and METIS GBSM channel models following minor extensions can support spherical wavefronts. Moreover, cluster appearance and disappearance can occur on both the array and time axes in massive MIMO systems; that is, each antenna element may observe its own set of clusters. However, models like COST 2100, SCM-extension, IMT-2020 and METIS channel models have not considered this massive MIMO channel characteristic. Notably, FLS characterizes the LOS propagation of the mmWave communication link. Nonetheless, the propagating wave encounters higher attenuations resulting from path loss and shadowing influences. Hence, large-scale fading models typically encapsulates the overall effects due to path-loss and shadowing. Path loss modeling attempts at the initial stage of channel measurement campaigns considered the known reference path-loss model [46], [139]. Due to significantly better match to measurements, the modified three-parameter floating-intercept (alpha-beta (AB)) large-scale path loss model adopted by 3GPP [162] and WINNER [202] was proposed in [23], [46]. While the modified AB offers a standard model, it widely varying (floating) modeling parameters lacks solid physical meaning when implemented in a particular frequency band or scenario. Subsequently, the dual-slope model, an extension of the single-slope model with better accuracy was introduce for path loss modeling in [46], [234], at distances surpassing 200 m range. A comparison of some of the path loss models introduced in literature are presented in Table 7. Note that the negative slopes (marked with*) in Table 7 are not usable because of the low number of samples. We have used HLB and LLB in in Table 7 to denote high loss building and low loss building, respectively. Parabolic Path Loss Model Characterizing the path-loss of mmWave signals in the sub-100 GHz band in the outdoor-to-indoor (O2i) environment [4].

Notably, parameters linked to non-stationary properties of massive MIMO channels like non-stationarities on both the array and time axes are critical measurement parameters required for massive MIMO channels. Since the non-stationary properties of massive MIMO channels fluctuate from scenarios to scenarios and difficult to estimate, an immense number of measurement campaigns are needed to capture these parameters. Besides, cluster behaviors on both the array and time axes need further investigations. In mmWave massive MIMO measurements, despite observing AoA shifts and cluster appearance and disappearance on the array axis of antenna elements, multi-user system-level simulations that account for the values of AoA shifts, as well as the birth and death rates of scattering clusters, are still challenging problems to be resolved. Moreover [259], [260], very few works of literature studied the elevation characteristics of massive MIMO propagation channels. Besides, realizing the massive MIMO channel, require a dedicated radio frequency (RF) chain for each antenna element. One possible architecture to reduce the number of RF chains is hybrid beamforming, which involves the concatenation of a high dimensional analog RF beamformer realized using phase shifters (PSs) and a low-dimensional digital baseband beamformer, which we discuss in the following section.

VI. BEAMFORMING ARCHITECTURES AND APPROACHES FOR mmWave MIMO SYSTEMS

Spectral efficiency can be enhanced from MIMO systems in two methods. Firstly, a base station that enables multiple UEs to communicate on the same time-frequency resource block [13], [261]–[266], can provide a set of noticeable advantages like higher spectrum efficiency and system throughput. Secondly, by beamforming with multiple data streams (i.e., precoding), between the BS and each UE [2], can further improve mmWave spectral efficiency. MIMO systems develop from MU-MIMO to massive MIMO, where hundreds or thousands of antennas are required in the base station, to realize the required transmission energy through beamforming gain. Beamforming is an antenna technique, which steers, predominantly signals formed from an array of transmit antennas to a desired angular direction [7], [72]. In the beamforming settings, the same symbol −weighted by a complex scale factor −is communicated across each transmit antenna, to achieve a unit rank input covariance matrix [7], [72]. The receiver then combines all the received signals coherently employing a different scale factor for the maximization of the received signal-to-noise ratio (SNR). This gain in SNR in antenna array systems is the so-called beamforming gain.

Beamforming with multiple data streams, referred to as precoding [2], is employed to further enhance the spectral efficiency of mmWave communication systems. In the conventional MIMO systems, both beamforming and precoding are realized typically in the digital domain [2], where all the signal processing techniques are performed at baseband, as illustrated in Fig 3(a). Hence, the so-called full-digital precoding. One of the most significant challenges in designing the conventional MIMO system is that it requires a dedicated RF chain[4] for each antenna [2]. Therefore, as a result of the high cost and high-power consumption of RF chains, it is not suitable to be realized for massive MIMO systems. Since the mmWave system integrates massive MIMO systems [2], the conventional full digital precoding becomes unrealistic due to the costs and complexity of RF chains, which lets analog processing in the RF domain desirable [2].

As a promising technique for mmWave massive MIMO systems, hybrid precoding can significantly reduce the number of RF chain as illustrated in Fig 3(c). While digital baseband processing enables controlling both the phase and amplitude of the signal, analog RF processing realized via phase shifters can only control the phase of the signal (i.e., there is a constant modulus constraint), which leads to

[4]An RF chain includes analog-to-digital converters (ADCs), digital-toanalog converters (DACs), mixers, a local oscillator (LO), filter, low noise amplifier (LNA), intermediate frequency amplifier (IFA), as well as baseband processing, etc [302].

TABLE 7. A comparison of some of the path loss models introduced in literature.

Channel Model	Mathematical formulation	Path loss mathematical model description	Frequency measurements were recorded	LOS		NLOS			
				n_p	σ_s [dB]	n_p	σ_s [dB]	α_p	β_p
Reference Path loss	$PL = PL_0 + 10n_p \log_{10}(\frac{d}{d_0}) + S_{\sigma_s}[dB]$ (26) For estimating the transmitter-receiver path loss based measurements with a separation distance $\leq$ 200 m. Examples, of models that use the reference path loss model, include MiWEBA [249], TG3c [242], TGad [246] and NYU (squared) model [256].	We have written $d_0(m)$ as the free-space reference distance and S_{σ_s} as the shadowing modeled as zero-mean Gaussian random variable standard deviation σ_s in dB. $d(m)$ is the path loss distance between transmitting and receiving antenna	60 GHz Peer to Peer [271] 73 GHz cross polarization (Omni & directional, respectively) [234] 28 GHz Omni., V-V [234]	2.25 4.17 & 3.5 1.1	2 9.0 & 6.3 1.7	4.22 6.4 & 4.6 2.7	10.12 15.8 & 9.7 9.6	- - -	- - -
Modified (three-parameter floating-intercept (alpha-beta)) path loss model	$PL = \alpha_p + 10\beta_p \log_{10}(d) + S_{\sigma_s}[dB]$ (27) For estimating the transmitter-receiver path loss based measurements with a separation distance $\leq$ 200 m. Examples, of models that use the Modified floating-intercept (alpha-beta (AB)) path loss model, include 3GPP [164], WINNER II [205].	$d(m)$ is the path loss distance between transmitting and receiving antenna, S_{σ_s} denotes the log-normal shadowing with standard deviation σ_s in dB, α_p and β_p denote the floating intercept and the linear slope, respectively	28 GHz [176] 73 GHz [176]	- -	- -	- -	8.7 8	72 86.6	2.92 2.45
Dual Slop Path Loss Model (on the basis of the floating intercept (FI)	$PL'_{\text{Du}}(d) = \alpha_p + 10\beta_{p_1} \log_{10}(d) + S_{\sigma_s}[dB]$ (28) $PL''_{\text{Du}}(d) = PL'_{\text{Du}}(d_{th}) + 10\beta_{p_2} \log_{10}(d)[dB]$ (29) Extended to include path loss values at 400 m	dth is a predefined threshold with $d \leq dth$ and $d > dth$, respectively for (28) and (29). β_{p_1} and β_{p_2} denote the dual slopes. Further details on dual path-loss model can be found in [4].	UT 38 GHz [47], with $dth = 184$ AAU 28 GHz [272], with $dth = 229$	- -	- -	- -	8.4 6.3	32.0 109.6	$\beta_{p1} = 4.5$, $\beta_{p2} = -4.4$* $\beta_{p1} = 0.5$, $\beta_{p2} = 3.9$
Parabolic Path Loss Model	$PL = 10\log_{10}(A + B \times f_c^2) + S_{\sigma_s}[dB]$ (30)	$f_c <$ 100GHz, A is 10 (5) for HLB (LLB), respectively. B is 5 (0.03) for HHB (LLB), respectively.							

considerable performance loss [13], [261]–[263]. Conventional analog precoding architecture share only one RF chain and thus can only support single-stream transmission and is not viable for multi-stream or multi-user scenarios as illustrated in Fig 3(b). Hence, spatial multiplexing gain cannot be achieved with conventional analog precoding architecture to improve spectral efficiency [262], [263]. To enable multi-stream transmission, separate RF chain for each antenna element is assumed in the so-call full-digital baseband precoding, applying amplitude and phase weights by matrix-type operations at baseband to form the beams. Since the general design principle of hybrid analog-digital precoding is to approximate the full-digital precoder, many works in literature [2], [6], [24], [141], [270]–[272] have proposed hybrid precoding designs that can achieve the optimal full-digital precoding performance. Besides, the hybrid precoding design is known to significantly improve the energy efficiency (EE) of the system [6], [273]. We now overview some key candidate transceiver architectures for beam alignment for mmWave massive MIMO systems.

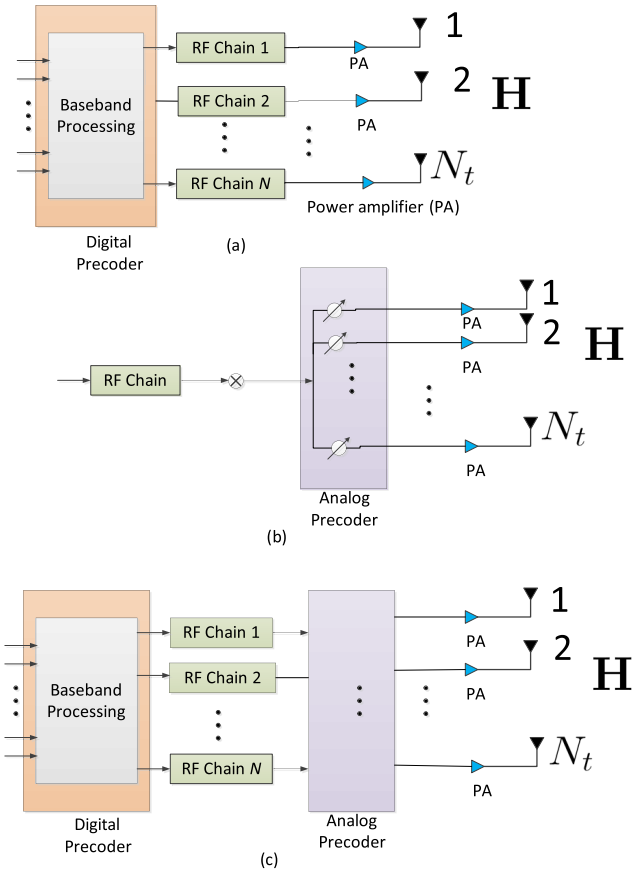

FIGURE 3. The mmWave massive MIMO systems precoding architectures: (a) Full-digital baseband precoding architecture, (b) Analog only precoding architecture, (c) Hybrid analog-digital precoding architecture. Here, N_t, N, and H denote the number of transmit antennas, number of RF chains, and the channel, respectively.

A. BEAM ALIGNMENT AND SELECTION ALGORITHM

The mmWave frequencies support packing a large number of antenna elements into small form factors [2], [274]. Nonetheless, beamforming is employed as a default method for mmWave massive MIMO systems, which typically requires continuous and accurate alignment. The highly directional beamforming gain realized needs to be aligned by an optimal hybrid precoding design since the analog circuit can only adjust the signal phase [2]. Therefore, directional mmWave beam alignment with the main channel path is essential for the high-dimensional analog RF precoding design, which determines the resulting beamforming gain and, consequently, the achievable rate [274]. Typically, there are two essential challenges in mmWave beamforming for mobile scenarios. Firstly, narrow beams in mmWave systems focus their transmitted power in the set direction, yet less robust to the movement as beam misalignment causes sharp connectivity loss. Secondly, the low-efficiency and time-consuming beam training scheme, since it appropriates network resources utilized for communication. The IEEE 802.11ad PHY layer transmits control (CPHY) sequence with both OFDM and single-carrier (SC) modulation schemes at operating frequencies of 2.64 GHz and 1.76 GHz [275], respectively. Each IEEE 802.11ad CPHY and SCPHY frame comprise of a beamforming training field, header, data, short training field (STF) and a channel estimation field (CEF) [275]. Thus, inside the IEEE 802.11ad CEF, holds two 512-point sequences, which embed Golay complementary pairs. These paired sequences have perfect aperiodic properties (i.e., whose aperiodic autocorrelation sidelobes are zero magnitudes), and used for communication CE, beam alignment and beam tracking. The authors in [275] introduced an IEEE 802.11ad MAC configuration to accommodate regular communications operations, which results in reduced overhead and misalignment in a high-mobility cellular environment. Based on the discrete Fourier transform (DFT) codebooks, the authors in [276] introduced an iterative antenna weight vectors (AWVs) training algorithm which employs one AWV feedback to realize the best transmit-receive AWVs pair. That is, rather than the initial multiple transmit-receive selections in the EEE 802.11ad design standard, only the best transmit AWV and receive AWV were selected for subsequent refinement. Moreover, the IEEE 802.11aj provides modifications to the IEEE 802.11ad PHY and MAC layers to support operation in the Chinese mmWave unlicensed frequency bands (45 GHz, $59-64$ GHz) [275]. The IEEE 802.11aj goal is to support backward compatibility with 802.11ad [275], and effective for communication CE, beam alignment and beam tracking.

B. HYBRID ANALOG-DIGITAL PRECODING AND COMBINING ARCHITECTURES

The mmWave massive MIMO will almost certainly apply HP with a reduced number of RF chain, to decompose the full-digital precoder via a high-dimensional analog precoder and a low-dimensional digital precoder [2], [6], [274], [277]. Benefits in hybrid analog-digital precoding are driven by the realization that the number of RF chains is constrained (at the transmitter) to be lower-bounded by the number of transmitted data streams [263]. In contrast, the beamforming gain and diversity order are determined by the number of antenna elements. Therefore, full-digital precoding which is realized at baseband presents increased flexibility with higher degrees of freedom (DoF) to realize efficient precoding algorithms. The full-digital baseband precoding can be realize entirely using analog precoding via a network of phase shifters, which controls only the signal phase before analog RF upconversion or after the upconversion stage [274]. However, analog precoding is subject to constant modulus constraint and suffers a low DoF, hence the need for hybrid analog-digital precoding.

The hybrid analog-digital precoding and combining architectures can be categorize into the fully-connected hybrid analog-digital precoding and combining and the partially-connected hybrid analog-digital precoding and combining architectures[5] [6], [272]. Besides, between

[5]In the fully-connected hybrid analog-digital precoding and combining architecture, each RF chain connects to all antennas, while in the partially-connected hybrid analog-digital precoding and combining architecture, each RF chain connects to a set of antenna elements.

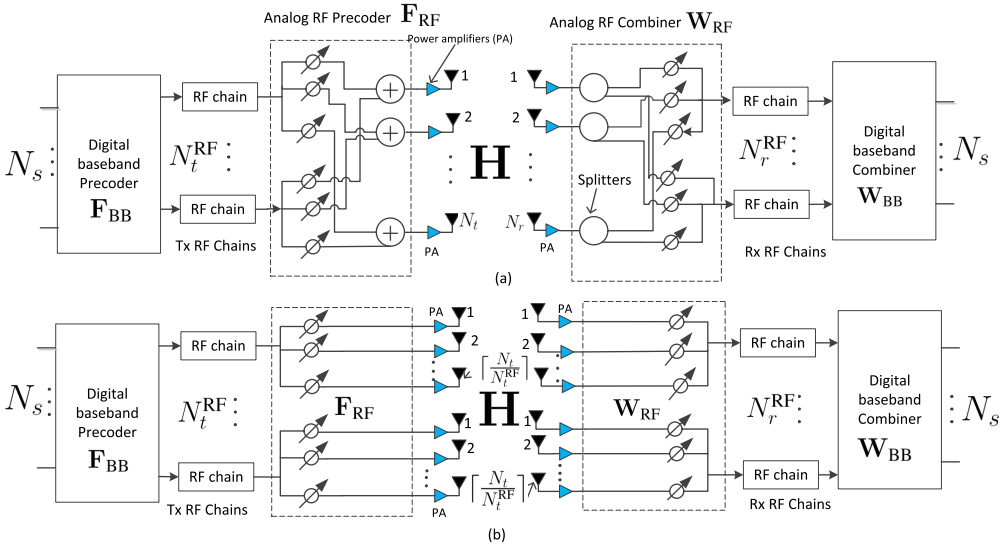

FIGURE 4. Hybrid analog-digital precoding and combining types [6] (a) Fully-connected hybrid analog-digital precoding and combining, (b) Partially-connected hybrid analog-digital precoding and combining, where each sub-array is connected to only a single RF chain.

the fully-connected and partially-connected hybrid analog-digital precoding and combining architectures, there exists a complexity-gain trade-off. For example, consider a fully-connected hybrid analog-digital precoding and combining architecture with N_t transmit antennas and N_t^{RF} transmit RF chains, the number of signal processing path is $N_t \times (N_t^{\mathrm{RF}})^2$, while $N_t \times N_t^{\mathrm{RF}}$ for the partially-connected hybrid analog-digital precoding and combining architecture [6]. Moreover, fully-connected hybrid analog-digital precoding and combining architecture has N_t^{RF} times more greater beamforming gain than partially-connected hybrid analog-digital precoding and combining architecture. It is worth noting that we have $N_t^{\mathrm{RF}} = N_r^{\mathrm{RF}} = N^{\mathrm{RF}}$ number of RF chains, where N_r^{RF} is the number of receive RF chains [6]. The hybrid analog-digital precoding and combining architectures aim to reduce hardware and signal processing complexity. The multiple RF chains availability in the fully-connected and partially-connected hybrid analog-digital precoding and combining architectures enable shaping the beam patterns close to those achieved by the full-digital architecture, i.e., with superior flatness over the covered sector, and far fewer overlaps with adjacent beams [272].

In the literature, there are only a few papers that show the hardware realizations of hybrid analog-digital precoding. In [278], the authors categorized the hybrid analog-digital precoding methods proposed for mmWave SU-MIMO into the application of codebooks, spatially sparse precoding, antenna selection, and beam selection. Furthermore, in [278] hardware structures of different complexities were differentiated while noting the specific design aspects for operation at mmWave frequencies. In [279], mmWave hybrid analog-digital precoding architectures, RF system realizations, signal processing algorithms methods, are presented.

A codebook based beamforming training method for mmWave massive MIMO systems can balance the trade-off between cost and performance [278]. Codebooks support different antenna array geometries and allow flexibility as regards the number, size, and spacing between antenna elements [278]. Generally, codebooks for joint hybrid analog precoder and combiner design are the Grassmannian-based codebook and RF beamsteering codebooks. Grassmannian manifold codebook [280] is designed to maximize the minimum distance between any pair of lines, spanned by the codebook vectors. Hence, a random search based Grassmannian manifold codebook design typically yields codebooks with the best minimum distance. The RF beamsteering codebook [281] is evaluated via the steering angle, and therefore, design to serve as a spatial filter-based on single-parameter quantization, generating small-sized codebook.

1) FULLY-CONNECTED AND PARTIALLY-CONNECTED HYBRID ANALOG-DIGITAL PRECODING ARCHITECTURES

The fully-connected hybrid analog-digital precoding architecture experiences full beamforming gain per transceiver [6]. It exploits all the AoD to realize the mapping (i.e., it maps every RF chain to all available antennas) via a network of phase shifters as illustrated in Fig. 4(a) [6]. Accordingly, all elements of the analog RF precoder $\mathbf{F}_{\mathrm{RF}}$ and analog RF combiner $\mathbf{W}_{\mathrm{RF}}$ results in constant modulus norm constraint, i.e., $|\mathbf{F}_{\mathrm{RF}}(i,j)| = |\mathbf{W}_{\mathrm{RF}}(i,j)| = 1, \forall\, i,j$ [2], [6], [272]. Therefore, the hybrid precoding-based mmWave massive MIMO realization with fully connected architecture requires analog processing networks of $N_t N_t^{\mathrm{RF}}$ and $N_r N_r^{\mathrm{RF}}$ phase shifters at the transmitter and receiver, respectively [2], [6], [272]. We have written $N_t(N_r)$ and $N_t^{\mathrm{RF}}(N_r^{\mathrm{RF}})$ to denote

the number of transmit (receive) antennas and the number of transmit (receive) RF chains, respectively.

Contrary to the fully-connected architecture, the partially-connected hybrid analog-digital precoding architecture connects each RF chain only to one sub-array with $\lceil N_t/N_t^{\mathrm{RF}} \rceil$ and $\lceil N_r/N_r^{\mathrm{RF}} \rceil$ antennas at the transmitter and receiver, respectively, as shown in Fig. 4(b). We have written $\lceil \cdot \rceil$ for the integer ceiling operator. Consequently, the analog RF precoding matrix $\mathbf{F}_{\mathrm{RF}} \in \mathbb{C}^{N_t \times N_t^{\mathrm{RF}}}$ in the partially-connected hybrid analog-digital precoding architecture consist of comprising of N_t^{RF} analog weighting vectors $\{f_i\}_{i=1}^{N_t^{\mathrm{RF}}}$ of the form [6]:

$$\mathbf{F}_{\mathrm{RF}} = \begin{bmatrix} f_1 & 0 & \cdots & 0 \\ 0 & f_2 & & 0 \\ 0 & 0 & \ddots & 0 \\ 0 & 0 & \cdots & f_{N_t^{\mathrm{RF}}} \end{bmatrix} \tag{31}$$

where each element of the vector f_i for $i \in [1, N_t^{\mathrm{RF}}]$ satisfies the constant modulus constraint.

Considering the channel sparsity of mmWave massive MIMO with hybrid analog-digital precoding and combining architecture, the limited number of RF chains relative to the number of antenna elements leads to a large dimensional analog RF precoding and combining matrices [6]. However, the analog RF precoding and combining matrices are sparse with a limited number of dominant components caused by the geometric characteristics of the mmWave massive MIMO channel. RF beam search algorithms iteratively finds the capacity maximizing RF beams over a subset of all available RF chains, where the size of the subset can be modified to suit different complexities.

a: DESIGN CHALLENGES AND PERFORMANCE OF FULLY-CONNECTED HYBRID ANALOG-DIGITAL PRECODING ARCHITECTURES

The work of [14] proposed an AltMin optimization hybrid analog-digital precoding and combining algorithm for mmWave massive MIMO systems for the fully-connected architecture. Results in [14] demonstrates that when $N_t^{\mathrm{RF}} \geq 2N_s$ and $N_r^{\mathrm{RF}} \geq 2N_s$, there exists a closed-form solution to the fully-connected hybrid analog-digital precoding design problem, which results in the same spectral efficiency performance furnished by the optimal full-digital baseband precoding. We have written N_s to denote the number of data streams. Therefore, in designing hybrid analog-digital precoders, the performance comparative analysis should focus on the $N_s \leq N_t^{\mathrm{RF}} < 2N_s$ regime [14]. The authors in [2] exploits the spatial structure of mmWave channels to formulate the hybrid analog-digital precoding and combining problem, as a sparse reconstruction problem. Here, the scattering structure of the mmWave channels is assumed to be N_t^{RF}-sparse [2]. Using an orthogonal matching pursuit algorithm, the analog RF precoder/combiner, and digital baseband precoder/combiner are designed. However, since OMP adds only one index per iteration, it requires a larger number of iterations to accurately approximate the optimal unconstrained precoders and combiners. Moreover, the OMP algorithm does not contain a pruning step [282]. Hence, wrongly selected indices of array response vectors will appear in the approximation, which degrades the spectral efficiency performance. The authors in [6] diverse the exploration of multiple candidates of array response vectors, to propose low-complexity hybrid precoder and combiner design via stage-determined matching pursuit (SdMP) [283], namely (LcHPC-SdMP). Based on the selection of multiple "correct" indices of array response vectors per iteration, the SdMP algorithm is finished with a much smaller number of iterations compared to the OMP. Since SdMP [283] contains a pruning step, wrongly selected indices of array response vectors in the proposed LcHPC-SdMP algorithm, will be eliminated in the subsequent iteration, which improves the spectral efficiency performance. Using a fully-connected hybrid-precoding architecture, the authors in [284] compare the rate performance and coverage of hybrid analog-digital precoding-based mmWave massive MU-MIMO system and single-user spatial multiplexing (SU-SM), with single-user analog beamforming (SU-BF). The authors in [284], find that with perfect channel state information at the transmitter and round-robin scheduling, the spectral efficiency performance of MU-MIMO outperforms that of SU-SM and SU-BF, and thus a better option for mmWave cellular networks. However, this observation neglects the channel acquisition overhead and computational complexity. In [28], practical hybrid analog-digital precoding-based mmWave massive MU-MIMO system is proposed, employing zero-forcing (ZF) precoding and beam selection for the digital and analog precoding, respectively. The authors in [28] find that hybrid analog-digital precoding with more RF chains outperforms the conventional full-digital baseband precoding.

b: DESIGN CHALLENGES AND PERFORMANCE OF PARTIALLY-CONNECTED HYBRID ANALOG-DIGITAL PRECODING ARCHITECTURES

It is demonstrated in [14] that there is a performance-complexity trade-off in selecting the partially-connected hybrid analog-digital precoding architectures. While the fully-connected architecture can achieve full beamforming gain via full phase control, the partially-connected architecture cannot achieve full beamforming gain in all scenarios due to the limited phase control [6], [14]. Conversely, the power consumption and hardware realization complexity of the partially-connected architecture are extremely lower over those of the fully-connected architecture [29]. As the partially-connected architecture typically consists of several sub-arrays of antenna elements, a dynamic sub-array structure that select the optimal sub-array in combination with the phase shifters, is proposed in [30] for hybrid precoding-based massive MIMO systems based on the long-term channel statistics. Hence, optimal sub-arrays selection for the partially-connected architecture is still an open issue.

It is shown in [29] that hybrid precoding performance in frequency-selective channels can asymptotically approach

the optimal fully-digital baseband precoding performance when the number of transmitting and receiving antenas is sufficiently large. This asymptotic design requires the mapping strategy of a fully-connected architecture and is not suited to the partially-connected architecture. The current challenge is how to implement the hybrid analog-digital precoding for the partially-connected architecture with the practical number of antennas to asymptotically approach the optimal fully-digital baseband precoding performance.

2) ANALOG-TO-DIGITAL CONVERTERS/DIGITAL-TO-ANALOG CONVERTERS (ADCs/DACs) RESOLUTIONS, PHASE SHIFTERS, AND ANTENNA ARRAY

Typically, hybrid analog-digital precoding and combining take the form of both an analog RF precoder realized via a network of phase shifters and a digital baseband precoder realize with a power-hungry and costly DAC at the transmitter side and ADC at the receiver side [6], [72]. It is common knowledge that the hardware cost and power consumption of ADCs/DACs exponentially increase with the number of quantization bits and linearly increases with the bandwidth [285]. Therefore, high-resolution ADCs/DACs will lead to high hardware cost and power consumption in practical massive MIMO systems. While the practical realization of hybrid analog-digital precoding requires high (or finite) resolution DAC/ADC and phase shifter, the high sampling rate and high bit-resolution requirements are at the expense of higher power consumption at mmWave frequencies. Compared to DAC [6], [72], finite or high-resolution ADC has shown to be more costly and power-hungry, hence turns to become a major research focus on the power and energy minimization of ADC or phase shifter, for mmWave massive MIMO communications. To resolve this challenging problem is to substitute the costly and power-hungry high-resolution ADCs/DACs (i.e., 8-12 bits), with low-resolution ADCs and DACs (i.e., 1-3 bits) which consumes low power. The authors in [286] introduce an iterative algorithm which sequentially designs the analog RF precoder/combiner with low-resolution phase shifters, for spectral- and energy-efficiency maximizing. Hybrid analog-digital precoding with few bits (or low-resolution) ADC has been investigated for spectral- and energy-efficiency trade-off in [285], [287]. The authors in [287] show that low-resolution ADCs can considerably improve energy efficiency with an acceptable performance loss in spectral efficiency. However, owing to the strong nonlinear characteristic of severe quantization, notable challenges in signal processing, channel estimation, multiuser detection, and phase/frequency synchronization unavoidably result. Therefore, a mixed-ADC/DAC architecture is introduced in [285], in which few antennas connect to low-resolution ADCs/DACs, while the rest connects to high-resolution ADCs/DACs, to improve the trade-off between spectral- and energy efficiency, while reducing the challenges in the signal processing and channel estimation task.

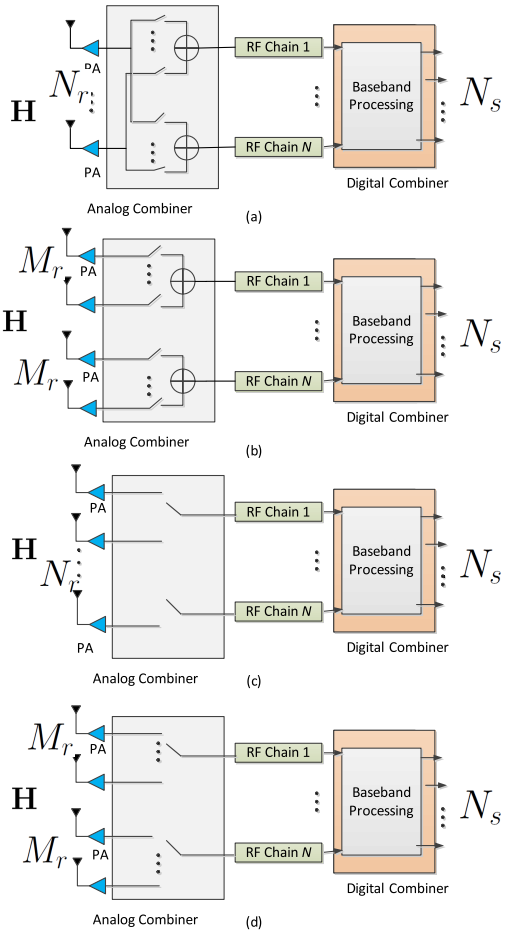

FIGURE 5. Analog architectures for the RF combiner. (a) Antenna selection with analog combining. (b) Antenna selection in subsets with analog combining. (c) Antenna selection. (d) Antenna selection in subsets. [99].

3) DYNAMIC SUB-ARRAY ARCHITECTURE, PERFORMANCE, AND CHALLENGES

A dynamic sub-array architecture [30] that selects subarray based on the long-term CSI, is presented in Fig. 5. In [30], moving the switching matrix towards the RF chains enables the optimal sub-array (i.e., antenna partitioning/grouping) in conjunction with phase shifters to be selected. Switches and networks of phase shifters, are employed to the channel (long-term channel statistics). Consequently, we turn to the design of proper antenna partitioning algorithms for an optimal sub-arrays selection.

4) SWITCH BASED ANALOG ARCHITECTURE

The authors in [99] find that hybrid combiner architecture based on switches realizes low-power and cost-effective solution for fixed array sizes and an equivalent number of RF chains, with performance approaching the traditional phased-array architectural approach. For example, the phased-based architecture is compared to the switched-based architecture in [99], demonstrating a large performance gap of approximately 2 b/s/Hz in favor of phased-based architecture, in the

realistic range of $1-7$ RF chains. However, for the equivalent number of RF chains, the switch-based architecture furnishes a $45-70\%$ reduction in power consumption. That is, for equivalent power consumption, a larger number of RF chains can be employed with switches, which leads to improved spectral efficiency. However, designing optimal combiners utilizing switch-based analog architecture introduces challenging problems since impairments such as noise figure or insertion losses, influence the actual SNR at the input of the digital combiner [99]. In the following, four hybrid analog-digital combining architectures are presented in Fig. 5, utilizing switch-based analog architecture as the essential constituent in the analog processing block.

a: SWITCHING NETWORK WITH ANALOG COMBINING (SNAC)

Each transceiver is connected to each antenna through a network of switches as illustrated in Fig. 5 (a). Each switching network selects a subset of N_{SNAC} antennas from N_r receiving antennas ($N_r \subset N_{\text{SNAC}}$), whose transmitter-receiver pairs are combined non-coherently, before subsequent RF chain connection [99], which may degrade performance in terms of sum-rate. Hence, devising optimal combiner introduces challenging problems. If the receiver uses its $N_s \leq N \leq N_r$ RF chains and its hybrid analog-digital combiner $\boldsymbol{W}_{\text{RF}}\boldsymbol{W}_{\text{BB}}$ (with an RF combiner $\boldsymbol{W}_{\text{RF}} \in \mathbb{C}^{N_r \times N}$ and a baseband combiner $\boldsymbol{W}_{\text{BB}} \in \mathbb{C}^{N \times N_s}$) to the received signal, the processed received signal is

$$\boldsymbol{y} = \sqrt{\rho}\boldsymbol{W}_{\text{BB}}^{H}\boldsymbol{W}_{\text{RF}}^{H}\boldsymbol{H}\boldsymbol{F}_{\text{RF}}\boldsymbol{F}_{\text{BB}}\boldsymbol{s} + \boldsymbol{W}_{\text{BB}}^{H}\boldsymbol{W}_{\text{RF}}^{H}\boldsymbol{n} \tag{32}$$

where $\boldsymbol{F}_{\text{RF}} \in \mathbb{C}^{N_t \times N}$ and $\boldsymbol{F}_{\text{BB}} \in \mathbb{C}^{N \times N_s}$ is the RF precoding matrix and baseband precoding matrix, respectively, such that $\|\boldsymbol{F}_{\text{RF}}\boldsymbol{F}_{\text{BB}}\|_F^2 = N_s$. We have written $\|\cdot\|_F$ to denote the Frobenius norm. N_s, N_t, N_r, N and $\boldsymbol{s} \in \mathbb{C}^{N_s \times 1}$ denote the number of data streams, transmit antenna, receive antenna, RF chains, and the symbol vector, respectively. In (32), the discrete-time transmitted signal is written as $\boldsymbol{x} = \boldsymbol{F}_{\text{RF}}\boldsymbol{F}_{\text{BB}}\boldsymbol{s}$. Therefore, the set of feasible RF combiners $\mathcal{W}_{\text{RF}}$ for SNAC is given by $\mathcal{W}_{\text{RF}}^{\text{SNAC}} = \{\boldsymbol{x} \in \mathcal{B}^{N_r \times 1}\}$, where $\mathcal{B}$ is the binary set $\{0, 1\}$ [99].

b: SWITCHING NETWORK IN SUBSETS WITH ANALOG COMBINING (SNSAC)

Each antenna is routed to a single switch, as illustrated in Fig. 5 (b) [99], which avoids the need for splitters, and low noise amplifiers, thus reducing power consumption. Each switching network selects a subset of M_r antennas from N_r receiving antennas (i.e., $N_r \subset M_r$) and combines only N_{SNSAC} of the M_r selected antennas, with $1 \leq N_{\text{SNSAC}} \leq M_r$. Therefore, the set of feasible RF combiners $\mathcal{W}_{\text{RF}}$ for SNSAC is given by [99]

$$\mathcal{W}_{\text{RF}}^{\text{SNSAC}} = \left\{ \begin{bmatrix} \hat{\boldsymbol{x}} \\ 0 \\ \vdots \\ 0 \end{bmatrix} \cup \begin{bmatrix} 0 \\ \hat{\boldsymbol{x}} \\ \vdots \\ 0 \end{bmatrix} \cup \cdots \begin{bmatrix} 0 \\ 0 \\ \vdots \\ \hat{\boldsymbol{x}} \end{bmatrix} \in \mathcal{B}^{N_r \times 1} \middle| \hat{\boldsymbol{x}} \in \mathcal{B}^{\frac{N_r}{N} \times 1} \right\}. \tag{33}$$

c: SWITCHING NETWORK (SN)

Antenna selection in a switching network according to channel conditions is known to maximize mmWave massive MIMO capacity [99]. In the switching network-based hybrid analog-digital combining architectures for mmWave massive MIMO systems, each transceiver links to any best one of N_r receive antennas (based on channel conditions) via a $N_r : 1$ antenna switch. Since the SN technique could result in large insertion losses, it is typically more tailored for small antenna arrays. Therefore, the set of feasible RF combiners $\mathcal{W}_{\text{RF}}$ for SN is given by $\mathcal{W}_{\text{RF}}^{\text{SN}} = \{\boldsymbol{x} \in \mathcal{B}^{N_r \times 1} | \|\boldsymbol{x}\|_0 = 1\}$, where $\mathcal{B}$ is the binary set $\{0, 1\}$ [99].

d: SWITCHING NETWORK IN SUBSETS (SNS)

Suitable for large antenna arrays since the combiner insertion loss can be by the selection of only one antenna per subset. Therefore, given a predefined subset of contiguous antennas, the set of feasible RF combiners $\mathcal{W}_{\text{RF}}$ for SNS is given by [99]

$$\mathcal{W}_{\text{RF}}^{\text{SNS}} = \left\{ \begin{bmatrix} \hat{\boldsymbol{x}} \\ 0 \\ \vdots \\ 0 \end{bmatrix} \cup \begin{bmatrix} 0 \\ \hat{\boldsymbol{x}} \\ \vdots \\ 0 \end{bmatrix} \cup \cdots \begin{bmatrix} 0 \\ 0 \\ \vdots \\ \hat{\boldsymbol{x}} \end{bmatrix} \in \mathcal{B}^{N_r \times 1} \middle| \begin{matrix} \hat{\boldsymbol{x}} \in \mathcal{B}^{\frac{N_r}{N} \times 1} \\ \|\hat{\boldsymbol{x}}_i\|_0 = 1 \end{matrix} \right\}. \tag{34}$$

Nonetheless, directly substituting variable phase shifters with switches can degrade performance in terms of sum-rate. Hence, an approach that effectively realizes analog phase shifters quantize phases is required, with a minimum reduced number of phase shifters [99], [288].

C. BEAMSPACE MIMO USING LENS ANTENNA ARRAYS

Beamspace using lens antenna arrays is the recent RF technology that has progressed from employing discrete antenna elements, to designing antenna arrays that operate as an optical system [288], [289]. A lens antenna array provides variable phase shifting for electromagnetic rays at various points on the lens aperture to realize AoA/AoD-dependent energy focusing property [288], [289]. Consequently, antenna selection can be implemented to significantly reduce the RF chain cost efficiently without compromising system performance, contrary to the case of implementing antenna selection with the conventional arrays. While conventional mmWave hybrid analog-digital precoding/combining with high-resolution phase shifters allow greater flexibility in the analog precoder/combiner design, lens-based topologies are inherently inflexible as the analog precoders have to be DFT matrices. Thus, making the channel estimation task problematic, especially for wideband systems where several antennas manage non-identical data symbols per sampling time [289]. The mmWave channels with sufficient AoAs/AoDs separations AoAs/AoDs, different beams in the spatial domain can be differentiated, with the aid of the lens antenna array. Consequently, the unfavorable multi-path effect in wide-band communications, i.e., the inter-symbol interference (ISI), can

be readily mitigated in the lens array MIMO systems [289], without complex ISI mitigation approaches like multi-carrier transmission, equalization, or spread spectrum. Accordingly, an efficient path grouping algorithm that can mitigate inter-path interference is required for mmWave channels with insufficient AoAs and/or AoDs separation; thus, a promising future research direction. Moreover, the power leakage problem in mmWave beamspace MIMO using lens antenna arrays has, in most current investigations, been neglected [289], which possibly results in SNR and system sum-rate, degradation [288]. Thus, the power consumption (single beam) model neglecting the power leakage problem, and selecting one beam per user via one RF chain, P_{SB}, is given as [288]

$$P_{\mathrm{SB}} = P_{\mathrm{T}} + P_{\mathrm{BB}} + P_{\mathrm{RF}}K + P_{\mathrm{SW}}K \tag{35}$$

where P_{T}, K, P_{BB}, P_{RF} and P_{SW} denote the total power budget, K single-antenna UEs, baseband power consumptions, one RF chain power consumptions, and one switch power consumptions, respectively. One solution to the power leakage problem is by appropriating several beams to obtain sufficient path power through multiple RF (MBMRF) structure [288]. Thus, we can model the power consumption [288]

$$P_{\mathrm{PMBMRF}} = P_{\mathrm{T}} + P_{\mathrm{BB}} + P_{\mathrm{RF}}B_T + P_{\mathrm{SW}}B_T. \tag{36}$$

We have used $B_T = \sum_k B_k$ and B_k to denote the total beam selected for all UEs and number of beam selected for the k-th UE, respectively. Employing a phase shifter network (PSN) to manage the power leakage problem introduced in [288], the power consumption can be model as

$$P_{\mathrm{PSN}} = P_{\mathrm{T}} + P_{\mathrm{BB}} + P_{\mathrm{RF}}K + P_{\mathrm{SW}}K + P_{\mathrm{PS}}B_T. \tag{37}$$

We have written P_{PS} to denote phase shifter power consumption.

D. MULTIPLE-ACCESS TECHNOLOGIES TOWARDS 5G WIRELESS NETWORKS

Several candidate multiple-access technologies have been considered primarily for 5G cellular networks in the sub-100GHz bands that can support multiple users in a single-bandwidth wireless link [6], [13], [290]. Some of the multiple access technologies or multiplexing techniques employed for practical mmWave massive MIMO systems include frequency division multiple access (FDMA), time division multiple access (TDMA), code division multiple access (CDMA), and orthogonal frequency division multiple access (OFDMA) [13]. The single-carrier FDMA (SC-FDMA) has been recently considered as a promising uplink transmission scheme for 5G cellular communications, because of its low peak-to-average power ratio (PAPR). However, issues like setting up large-scale BS transceivers, complicated channel Control, and realizing low-cost highly stabilized local oscillator, are often encountered [291]. The digital mobile radio system employing the TDMA technique is an essential primary solution to the problem associated with SC-FDMA [13]. Some advantages of the TDMA includes low-cost BS, low-frequency stability, decrease interferences, and channel control flexibility [13], [290]. In the CDMA multiplexing technique, multiple UEs access a channel simultaneously and asynchronously via using preassigned signature sequences, which allows the UEs to modulate and spread their information-bearing signals [292]. CDMA presents a more substantial capacity over conventional multiple access technologies like TDMA and FDMA, to combat the inherently hostile frequency-selectivity of the transmission channels [292]. With the human voice activity cycle known to be 35%, the current CDMA systems boast at least three times the capacity of TDMA, since all UEs share one radio channel [292]. Unlike TDMA and FDMA, which implements an equalizer at the receivers, the CDMA system does not need an equalizer, but a more straightforward device called a correlator to despread the spread spectrum signal. Unfortunately, as the number of UEs increases using CDMA, the overall quality of services decreases. Accordingly, OFDM makes resourceful utilization of the spectrum by overlapping, by managing to transform a frequency-selective fading channel into several flat fading subchannels with independent additive noise vectors [282], which significantly reduces the complexity of the receiver design. Similarly, OFDMA is a multi-user version of OFDM but with higher sensitivity to frequency selective fading as a significant disadvantage. MmWave frequencies can as well deploy the FDMA, TDMA and OFDMA multiple-access technologies, but in diverse aspects owning to the highly directional channel characteristics of mmWave transmission.

One key component of 5G communications system is the multiple access technology that it employs. It is worth noting that, multiple access technologies for mmWave systems need to turn to extreme interference management strategies, viz space division multiple access (SDMA) (which entirely tackle interference as noise), NOMA (which fully decode interference) and random access.

1) SPACE-DIVISION MULTIPLE ACCESS

Generally, there are two techniques used to suppress inter-user interference, i.e., SDMA and interference suppression precoding like zero-forcing precoding[6] [293]. Nevertheless, both have their benefits and drawbacks, and it is nontrivial to obtain a hybrid design that balances both. Taking advantage from multi-user gain induced by massive MIMO techniques [294], SDMA is capable of significantly improving spatial throughput in mmWave communications for 5G networks. Specifically, SDMA simultaneously serves multiple UEs in the same channel over identical spectrum resources by the superposition of the beam (i.e., it divide the space into a number of orthogonal spatial beams) [294]. In [295], a low complexity joint transmission scheme for mmWave massive MU-MIMO system is introduced, combining SDMA and interference suppression precoding to improve system

[6]In zero-forcing precoding, each UE's precoding vector increases the channel energy of its own and suppresses that of the others [293].

sum-rate capacity. In [293], a low complexity joint transmission scheme, which combines double-precoding-based SDMA and ZF-precoding interference suppression, is proposed to improve system performance.

2) NON-ORTHOGONAL MULTIPLE ACCESS

NOMA can be combined with massive MIMO systems (massive MIMO-NOMA) to enhance the spectrum efficiency further over massive MIMO systems with conventional orthogonal multiple access (massive MIMO-OMA) scheme [261], [296]. NOMA works on the principle of sharing time-frequency resources between UEs via separating them in another domain [263]. Specifically, this domain of separation occurs in two regimes −power-based and code-based, leading to power-domain NOMA (PD-NOMA) and code-domain NOMA (CD-NOMA) realizations, respectively [263]. Currently, attention has been place to combine NOMA and mmWave massive MIMO systems with hybrid analog-digital precoding, to achieve higher spectrum efficiency. By Implementing mmWave massive MIMO-NOMA systems with hybrid precoding, one beam can support two or more UEs with the help of intra-beam superposition coding and successive interference cancellation (SIC) [261], [296], which differs significantly from conventional mmWave massive MIMO where one beam supports only one UE at the same time-frequency resources. A low-complexity realization of hybrid precoding beamspace MIMO combined with NOMA was first proposed and investigated in the pioneering work of [261], where power allocation was optimized to maximize the achievable sum-rate. The authors in [261] introduced a new transmission scheme of HP-based beamspace MIMO-NOMA, where the number of UEs can be larger than the number of RF chains. Then, an iterative algorithm was introduced, premised on the equivalent-channel hybrid precoding to realize the optimal power allocation for the UEs. In [266], a capacity performance of a simplified mmWave massive MIMO-NOMA system is introduced by dividing the capacity analysis into the noise-dominated low-SNR regime and the interference-dominated high-SNR regime. The authors in [266] find that the number of UEs strongly contributes to capacity improvement, based on the non-orthogonal user multiplexing in the same time-frequency resource block enabled by NOMA. The authors in [264] introduced a general downlink mm-Wave NOMA system with the aid of random hybrid beamforming, splitting the non-convex problem into user scheduling and power allocation subproblems. Then, by leveraging the branch and bound technique, a global optimal power allocation solution is realized. In [265], hybrid analog-digital precoders and power allocation for the mmWave-NOMA system were separately designed to maximize the sum-rate. Based on an analog beamforming architecture with a phased array, joint power allocation and beamforming is proposed in [297], to maximize the sum rate of a 2-user mmWave-NOMA system. The authors in [298] investigates the design challenges of mmWave-NOMA beamforming, and results show higher achievable sum-rate performance and robustness for mmWave-NOMA multi-beamforming compare to conventional single-beam forming. In [262], joint hybrid precoding based mmWave MIMO combined with NOMA is proposed by optimizing user grouping, and power allocation to improve the achievable sum-rate and energy efficiency over conventional mmWave MIMO-OMA systems.

It is highly beneficial to combine NOMA with mmWave massive MIMO systems owing to the following advantages:

- Since the channel of different UEs in mmWave communication are highly correlated in the same direction, highly directional beams can be realized by the large-scale antenna array, which leads to higher beamforming gains, and thus, lesser inter-beam interference. Hence, mmWave massive MIMO-NOMA transmissions can be implemented on each beam to exploit the channel condition.
- NOMA combined with mmWave massive MIMO can enable each data stream to simultaneously support more than one UE at the same time-frequency resource block, and can transform different channel gain between UEs into multiplexed gain with the aid of intra-beam superposition coding and successive interference cancellation (SIC). Thus, mmWave massive MIMO-NOMA systems can improve system spectral efficiency.

3) RANDOM-ACCESS TECHNIQUE

The random access technique realized in mmWave cellular systems is employed mainly for initial access and handover [1], [299]. To fully exploit the beamforming gain, the beam direction, and channel path must be well aligned, by utilizing the beam quality estimation and information exchange (between BS and UE) on the best beam direction [299], as in IEEE 802.11ad protocol. However, there are conditions when mmWave-band communications employing the best beam pair may be impracticable. That is, for random access channel preamble transmission and reception, setting the beam directions at both the MS and BS, respectively, is challenging. For example, when a UE initially accesses the communication network employing a random access channel, the best beam pair cannot be known a priori and, thus, cannot fully exploit beamforming. As cellular networks employ random access channels for handover procedures, the random access channel design turns to a critical issue (even more challenging for mmWave communication) to be resolved initially. In [299], analysis of the critical problems of random access channel design, subject to initial access, handover, uplink-downlink configuration, and scheduling, were presented. The authors in [299] find that the performance gain from beamforming in multiple directions without prior knowledge of the best beam pair can yet be achieved. In [300], several different design options for mmWave initial access, i.e., the establishment of a link-layer connection between a UE and a BS, is evaluated. Even during initial access/cell search, beamforming is considered necessary for mmWave communication. While the analog beamforming is an energy-efficient technique for

initial access/cell search, it inherently experiences search delay during initial access. In [301], the authors find that the availability of context information (about mmWave BS) at the MS can reduce the inherent initial access/cell search delay of analog beamforming.

E. CHANNEL ESTIMATION METHODS FOR mmWave MASSIVE MIMO SYSTEMS WITH HYBRID PRECODING

Channel estimation (CE) for mmWave massive MIMO channel is demandingly challenging [27], [302], [303], as a result of the vast number of transmitting and receiving antennas and the small SNR before hybrid precoding. However, to fully benefit from the beamforming gains in mmWave massive MIMO systems, accurate CE is crucial to realize optimal hybrid analog-digital precoders and combiners. Specifically, the analog RF precoder and combiner, are designed to enhance the signal power, while the digital baseband precoder and combiner, are designed to suppress inter-user interferences. Towards this end, several CE techniques have been introduced [6], [13], [24], [26], [27], [262], [273], [302], [303] for mmWave massive MIMO systems. In the works of [6], [13], [24], [26], [262], [273], perfect CSI knowledge availability is assumed at the transmitters, in the design of hybrid analog-digital precoders and combiners in an attempt approach capacity. In works of [27], [302], partial knowledge of the CSI is assumed to be available at the transmitter, in the design of optimal hybrid analog-digital precoders and combiners for mmWave massive MIMO systems. The authors of [303], formulated the AoAs/AoDs estimation into a block-sparse signal recovery problem and introduced an adaptive angle estimation algorithm to solve the problem, i.e., to estimate the AoAs/AoDs. The researchers [302] and [304] have introduced CS-based and tensor-based CE algorithms for mmWave massive MIMO systems, respectively. However, they assume the conventional framework for training-based estimation, where the downlink and uplink CE problems are decoupled, and addressed separately at the receiver and transmitter, respectively.

As the dimension of the mmWave massive MIMO channel matrix increases, matrix operations required in the CE task will induce significantly higher computational complexity in the practical realization. For example, in frequency division duplexing (FDD) mode for 5G, CE is usually performed at the power-limited UE side [304], where the computational complexity becomes a major challenge as the number channel coefficients to be estimated is large. By exploiting the spatially common sparsity and temporal correlation of massive MIMO channels, the CE dimension challenge, can be effectively reduced. However, as a result of the additional hardware constraints of the analog RF phase shifters, in mmWave massive MIMO systems compared to those of conventional MIMO systems, it is challenging to design efficient CE algorithms. Hence, the joint design of CE and transmit precoding tailored to mmWave massive MIMO systems is well worth future efforts as the CE technique for such a hybrid analog-digital precoding and combining system is far from being well investigated.

F. SUMMARY OF BEAMFORMING ARCHITECTURES AND APPROACHES FOR mmWave MIMO SYSTEMS

High power consumption and expensive hardware are two drawbacks for massive MIMO systems realization. Some of the promising solutions are to employ hybrid analog-digital precoding and combining, and low-resolution ADCs/DACs. The paradigm shift towards higher bandwidth, as offered by mmWave frequency band, requires hybrid analog-digital precoding with limitted RF chains to significantly reduce the power consumption and hardware cost. We discussed the various hybrid analog-digital precoding and combining architectures, i.e., the fully-connected which achieves full beamforming gain per RF chain at the cost of hardware complexity, and the low complexity partially-connected architecture which renders low beamforming gain. Using low bit resolution ADC (in digital baseband precoding) and phase shifters (in analog RF precoder) perform a crucial role in maximizing energy efficiency but at the expense of lower spectral efficiency. In spite of the rate loss caused by the application of low-resolution ADCs/DACs, employing massive MIMO systems, however, permits a high achievable rate and considerable power saving. Besides, we envision as a future possibility that, RF signals will not only turn to a power source for energy-efficient cellular networks, but their information transmission and power realizations, simultaneously combined.

From a mmWave massive MIMO communications outdoor scenario, hybrid analog-digital precoding and combining solutions rely on specific essential design challenges presented in the following:

- *Hybrid analog-digital precoding and combining architectures for mmWave massive MIMO systems*: To achieve hybrid precoding performance close to full digital precoding, the determination of the optimal number of RF chains and analog RF phase shifters, on the availability of a considerable number of multiplexed data streams and antenna elements, establish an interesting design problem.
- *Analog RF precoder/combiner and digital baseband precoder/combiner designs:* Most existing works neglect the potential of parallel, multi-data stream processing to speed up the beam training phase, typically achieved by scanning multiple spatial directions, simultaneously. Instead, most works focus on the design of hybrid analog-digital precoders and combiners to maximize the achievable rate through the data transmission phase. Hence, the joint analog RF precoder/combiner and digital baseband precoder/combiner optimization problem is typically based on maximizing spectral efficiency achieved by Gaussian signaling over the mmWave channel, subject to constant modulus constraints on the elements of the RF precoder/combiner. From the physical realization standpoint, algorithms that

provide benefits to enable parallel hardware architecture for efficient signal processing is desirable.

- *Channel estimation:* In mmWave massive MIMO systems, optimal hybrid analog-digital precoding/combining gains can be achieved only in the case of perfect channel knowledge. Nevertheless, the far fewer numbers of RF chains relative to the number of antenna elements exhibit a burden for direct CE. Moreover, there is a challenge in CSI availability at the transmitter side, since the mapping linking transceivers and antennas makes CE in both the downlink and uplink more complicated. Methods for efficient channel estimation of mmWave massive MIMO channels, and thorough consideration of frequency selective mmWave massive MIMO channels, are still the topic of ongoing research.
- *Practical limitations due to RF hardware constraints:* The fundamental challenges in designing hybrid analog-digital precoders/combiners are the practical RF hardware constraints associated with the analog RF components. Specifically, it requires that the analog RF precoding/combining, be realized with constant modulus phase shifters and low-resolution quantized phase control. Therefore, hybrid analog-digital precoders/combiners design, essentially, requires the solution of several matrix factorization problems with constant modulus norm constraints. Moreover, since the analog RF and digital baseband precoders and combiners at the transmitter and receiver sides, respectively, are coupled, make the resulting joint optimization problem, non-convex.

VII. SIMULTANEOUS WIRELESS INFORMATION AND POWER TRANSFER

Removing the power line linking cellular devices to the grid for recharging is an envisioned solution for future cellular communication systems [7], [13], [262], [263]. Simultaneous wireless information and power transfer (SWIPT) has attracted significant attention in mmWave massive MIMO communications for simultaneous transmission of energy and information and regarded as a promising solution to realize this envision. SWIPT realization will lead to fundamental changes and new challenges in future 5G mobile communication design [7], [305]. Specifically, one method to achieve SWIPT is the use of a power-splitting receiver at each UE, to divide the received RF signal into two parts for simultaneous information decoding (ID) and energy harvesting (EH) [7], [13], [262], [263], [305]. Under the power-splitting architecture, it is beneficial to realize SWIPT by joint optimization of the transceivers for ID and power-splitting factors for EH. By exploiting the diversity and spatial multiplexing gain, a massive MIMO system can potentially enhance SWIPT transmission performance [13], [262]. Therefore, power splitting and transceiver design for the SWIPT-enabled mmWave massive MIMO system with hybrid precoding has recently received significant attention.

While RF energy is a form of electromagnetic energy that propagates both electrical and magnetic energy radiating through free space, components of the EH circuitry include antenna, matching network, and rectifier, generally known as a rectenna (or an RF/DC) [7]. Thus, RF EH is capable of harvesting and converting high-frequency energy in free space, to DC power, and requires the following well-balanced designs:

1) ANTENNA DESIGN

Proper antenna design for RF EH achieved by precise adjustment of impedance matching circuit and power control at different frequencies can effectively capture RF signals. However, it also brings new challenges and like path loss and shadowing as mitigating factors. The interested reader is referred to [305], where various antenna topologies for RF EH have been presented [7].

2) MATCHING NETWORK

Use to match the antenna impedance with the complex load impedance, which consists of capacitive and inductive elements, to realize the maximum power transfer from the antenna to the rectifier.

3) RECTIFIER CIRCUIT

Used to convert captured RF signals to the DC voltage levels [7]. One foremost challenge of the rectifier circuit design for RF EH applications is to generate a substantial voltage from the RF harvested energy [306]. The efficiency of the RF to DC voltage conversion is determined by the diode is in the rectification circuit, which serves as the principal component. Typically, employing a lower-voltage diode leads to a higher rectifying efficiency for RF EH [306].

A. RECEIVER ARCHITECTURE DESIGN

The SWIPT technology may not optimally support reliable information reception using the conventional information receiver architecture. The fact is that RF EH and information reception operate on dissimilar power sensitivity of -10 dBm and -60 dBm [79], respectively. That is, to enable SWIPT, EH and ID operations cannot be performed on the same received RF signal since the information content of the signal is destroyed by the EH operation. Therefore, several SWIPT-enabled receiver architectures can be implemented, such as time switching, separated receiver, antenna switching, and power splitting as illustrated in Fig. 6. Theoretically, power-splitting receiver design is known to achieve the best trade-off between the information rate and the amount of RF energy transferred. The power splitting receiver employs a certain power splitting ratio at the UE to divide the received RF signal into two, to enable simultaneous ID and EH at the receiver. Notably, the power splitting ratio can be optimized in each receiver and varied to balance the information rate and the harvested energy based on system requirements. Given that $\theta_j \in [0, 1]$ is the value of the power-splitting coefficient for the jth receiver, where θ_j is the fraction of RF signals

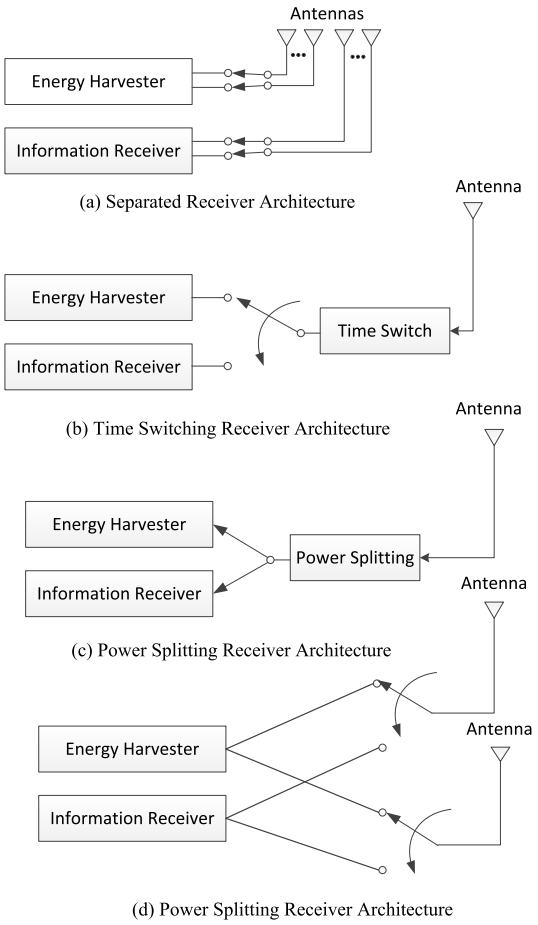

FIGURE 6. Integrated receiver architecture designs for SWIPT [79]: (a) Separated receiver architecture, (b) Time switching receiver architecture, (c) Power splitting receiver architecture, and (d) Antenna splitting receiver architectures.

employed for EH [7]. Then the power of harvested RF energy at a power-splitting receiver j from the ith source is of the form [7]

$$P_{j,i} = \eta P_i |h_{i,j}|^2 \theta_j, \tag{38}$$

In the meanwhile, the maximum ID rate at the jth power splitting receiver decoded from the ith source reads

$$R_{J,i} = W \log \left(1 + \frac{(1-\theta)P_i |h_{i,j}|^2}{\sigma^2 + \sigma_{sp}^2}\right) \tag{39}$$

where W, σ^2 and σ_{sp}^2 denote transmission bandwidth, transmission noise power, and signal processing noise power, respectively.

B. CIRCUITRY REALIZATIONS

Several RF EHs are implemented employing diverse technologies like complementary metal-oxide-semiconductor (CMOS), HSMS and SMS Schottky diode [7], [79]. Based on a recent survey in [79], several RF EH realizations utilize CMOS technology, which can yeild 1 V DC output, with −22 dBm to −14 dBm harvested RF power. While CMOS-based RF-EH realization supports a lower minimum RF input power, the peak RF-to-DC power conversion efficiency (PCE) is generally below that of the HSMS-based RF-EH realization. For instance, with over −10 dBm minimum RF input power, over 70% peak RF-to-DC PCE, can be achieved [79]. An SMS-based RF EH technology power rectifier achieved 85% PCE with 40-dBm input power with a dc output voltage of 30 V. THus SMS is suitable for RF-EH at high power, however suffers from low PCE with low harvested power [79].

C. SWIPT-ENABLED mmWave MASSIVE MIMO SYSTEMS AND ITS INTEGRATION WITH EXISTING TECHNOLOGIES

In [307], a SWIPT-enabled mmWave massive MIMO system with a lens-array antenna structure is introduced to maximize systems energy efficiency, by jointly optimizing the transmit power, beamforming, and power splitting ratio. In [308], a SWIPT-enabled mmWave massive MIMO system with limited RF chains is introduced, to maximize systems energy efficiency, by using one ID and several separate EH receivers.

SWIPT technology can be combined with mmWave MIMO-NOMA technology to improve the performance of both spectral efficiency and energy efficiency through joint transceiver and power splitting optimization. In [13], SWIPT-assisted mmWave massive MIMO-NOMA systems with hybrid precoding was investigated for the first time, where each UE uses a power splitter to extract both information and energy from the received RF signals. Subsequently, the optimization for power allocation and power splitting factors was determined to maximize the achievable sum rate. To implement SWIPT-enabled in HP-based mmWave massive MIMO-NOMA, the authors in [262] first introduced a K-means user grouping algorithm. Then the power allocation and HBF are jointly optimized to maximize the achievable sum-rate for all UEs.

D. SUMMARY OF SIMULTANEOUS WIRELESS INFORMATION AND POWER TRANSFER

Only limited surveys and overview articles directly relate to SWIPT and EH have been presented in the literature. Moreover, only a few studies have combined SWIPT with massive MIMO-NOMA systems to investigate the potential spectral and energy efficiency gains in mmWave communications. To achieve SWIPT, each UE employs a power-splitting receiver for simultaneous ID and EH which can lead to significant performance gains based on power consumption, spectral efficiency, transmission delay, and interference management. However, SWIPT introduces additional challenges for the joint transceiver and power splitting optimization for the mmWave MIMO-NOMA system with hybrid analog-digital precoding and combining architecture. Therefore, a proper scheme is required that examines both information and power that can render notable energy- and spectrum-efficient wireless communication and result in possible revolutionary applications and services. That is, optimal power allocation and UE scheduling are critical factors for

improving system performance and satisfying the so-called SWIPT-enabled hybrid precoding-based mmWave massive MIMO-NOMA system QoS constraints. Owing to practical constraints of the EH circuitry, realizing both EH and ID from the received signal is not feasible. Hence, optimized power allocation algorithms are required to improve the performance of SWIPT. Therefore, the joint optimization of the transceiver for ID and power splitting for EH, as well as UE grouping and scheduling, HP scheme and power allocation, is required.

VIII. 5G RESEARCH ACTIVITIES AND POTENTIAL RESEARCH TOPICS

Competition is intense on the 5G global platform, 5G activities are increasing, as vendors and service providers in technology-oriented countries, including South Korea, China, the United Kingdom, Germany, and the United States, work on early 5G network trials and test 5G in limited groups. An aggregate of thirteen 5G commercial networks in 2018 was launched, particularly regarding both mobile and fixed wireless deployments, with 42 new network launches envisioned in 2019. As 5G competition advances, other countries including, Switzerland, Russia, Japan, and Finland, are in the making in 5G development, owing to limited deployment. The accelerated schedule agreed to by the 3GPP in 2017 has witnessed some operators around the globe - including the US and China-present their 5G commercial launch plans. In late 2017, non-standalone 5G new radio (NSA 5G NR) specifications were officially approved, as part of the standardization activities of 5G. NR blueprints now available, chipmakers, hardware manufacturers can improve their tests, and develop components that realize the 5G new radio specifications, while expecting final standardization over NSA and standalone (SA) models. We present the current 5G commercial network including current 5G research, 5G field testing / 5G trials, and 5G development by country, in Table 8.

Diverse applications of massive MIMO in hot research directions in 5G, needs to be analyzed and investigated. Despite the fact there is no agreement on how specifically a 5G network ought to be, some inclinations are presently perceived. Some of the envisioned 5G architectural insights are being studied based on physical network structure, signalling protocols, and network management. In the following, we present a summary of the key architectural approaches envisioned for 5G based on potential gains and challenges.

A. INTERNET OF THINGS

With the Internet of Things (IoT) and cellular-based machine-to-machine (M2M) communication systems, 5G systems need to support the large numbers and deployable devices [309]. However, RACH congestion induced via massive access from M2M devices produces random access (RA) throughput degradation and link failures to the devices. These are low data rates sensor devices yet, their enormous number produces challenging problems, to network connectivity. Moreover, as a consequence of inefficient radio spectrum utilization, the cellular-based M2M traffic is expected to deteriorate the traditional cellular traffic performance. The challenges facing the IoT realization involve scalability, network management, security and privacy, interoperability and heterogeneity, network congestion and overload, and network mobility and coverage. The challenges facing the IoT realization involve scalability, network management, network congestion and overload, security and privacy, interoperability and heterogeneity, and network mobility and coverage. Considering network congestion, the massive number of connected devices produces enormous traffic, resulting in network congestion leading to a high packet loss rate. Interoperability and heterogeneity issues need to be addressed since heterogeneous IoT communication networks and devices will integrate into a unique standardization.

B. VEHICULAR COMMUNICATION NETWORKS

In accordance with the recent advances in the automotive industry regarding autonomous driving, vehicular communication are prone to become major applications of 5G networks. Hence, various vehicles can be implemented with mmWave massive MIMO systems to achieve effective vehicle-to-vehicle (V2V), vehicle-to-infrastructure (V2I), vehicle-to-pedestrian (V2P), and vehicle-to-network (V2N) communications, in an intelligent transportation system (ITS). Different use cases will possess different requirements sets, which the communications system requires to manage efficiently and cost-effectively, under the so-called V2X communications [309]. Therefore, a potential application for Device-to-Device (D2D) communication, which, unfortunately, faces multiple threats such as jamming, data modification, free-riding, and privacy violation [310]. Moreover, high mobility of vehicles yields challenges for the PHY layer, owing to the Doppler shift degradation and adaptive beamforming, and for the MAC layer, as to mobility management, routing, and dynamic resource allocation.

C. MULTI-HOP COMMUNICATIONS

Multi-hop communication is an efficient transmission technique that splits the communication link between the UE and the BS into several, possibly, even though the UE has no direct connection to a BS [310]. Multi-hop communications enable the UE to still communicate outside the BS coverage area, besides increasing the data rate and reduction of the transmit power. Hence, an essential solution to network coverage. However, challenges like the development of efficient routing algorithms with limited signalling overhead, while considering network mobility and the dynamic on/off switching of the relay node, need to be accurately addressed. Moreover, privacy and security issues ought to be addressed.

D. HIGH SPEED RAILWAY COMMUNICATIONS

5G systems are envisioned to realize data rates up to 150 Mbps UEs traveling at speeds up to 500 km/h in high-speed railway (HSR) scenarios. However, future

TABLE 8. Current 5G commercial network including current 5G research, 5G field testing / 5G trials, and 5G development by country [90], [91].

Country	5G research	5G trials / test	Partial Role in Developing 5G Network	5G commercial
South Korea	5G SK Telecom (SKT) 5G LG Uplus 5G Korea Telecom (KT)	1) 5G SKT/ Samsung (Nokia, Ericsson, Samsung, Intel and Rohde and Schwarz) completes 5G field trial. 2) 5G Korea Telecom / NEC is testing at Phoenix Park Ski World in Pyeong Chang.	5G SKT and 5G KT showcase 5G service at the 2018 Olympic Winter Games in PyeongChang	SKT, KT, and LG Uplus launched 5G mobile. The Samsung Galaxy S10 5G was launched using South Korea's 5G network.
China	5G China Mobile	5G China Mobile / ZTE completed testing the world's first pre-5G massive MIMO base station.	Chinese ZTE Gigabit Phone unveiled 2017, capable of utilizing 5G connectivity. ZTE GM 5G standalone architecture functionality test. ZTE plans to launch 5G phone in 2019. Huawei to launch 5G	China telecom operators rolled out 5G nationwide coverage (50 cities) in 2019.
United States (USA)	5G Verizon 5G AT&T 5G T-Mobile USA 5G Sprint 5G Google 5G Facebook	1) Qualcomm Technologies (San Diego)- first 5G mobile connection (1 Gbps)(Snapdragon X50 5G modem chipset) 2) 5G Verizon testing in "sandboxes" in New York; 3) 5G AT&T / Ericsson testing in Middletown; 5G AT&T / Nokia testing in Austin, 5G AT&T testing in Atlanta. 4) 5G T-Mobile USA testing; 5G Sprint/Nokia & Ericsson demos in Philadelphia, 2016; 5G Google (Skybender) testing in New Mexico; 5G Facebook (Terragraph / ARIES) testing in San Jose;	AT&T rolls out mobile 5G service in 12 US cities, 2018; Verizon - Disney using high-speed 5G technologies; Sprint /Nokia/Qualcomm completed the world's first over-the-air commercial 5G data transmission using 2.5 GHz, 2019; T-Mobile / Ericsson / Intel - completed the world's first 5G data call and video call on 600 MHz on a live commercial network, 2019;	Sprint (2.5GHz mid-band) 5G and Verizon 5G service provides commercial services; T-Mobile to launch a nationwide 5G network, AT&T to launch 5G in 2020.
Japan	5G NTT DoCoMo	1) 5G NTT DoCoMo /Huawei demonstrates mobile internet speeds of 3.6Gbps in China. 2) 5G NTT DoCoMo/Nokia trial of real-time transmission of 8K of 48Gbps video, 2016. 3) 5G NTT DoCoMo/Toyota tested controlling a humanoid robot on 5G, 2018.	5G NTT DoCoMo, planning to launch 5G service at the 2020 Tokyo Olympic and Paralympic Games.	-
Russia	5G MegaFon 5G Rostelecom 5G MTS 5G VimpelCom (Beeline)	1) 5G MegaFon/Huawei testing 5G cellular networks via TV channel "Russia 24" 2) 5G MTS/ Nokia & Ericsson tested in Russia, 2018. 3) 5G trial Rostelecom/Ericsson test (St. Petersberg) and 5G trial Rostelecom/ Nokia test (Skolkovo).	Russian mobile operators set to launch commercial 5G networks in 2020; MTS, Megafon, Beeline and Tele2 to create a single 5G operator.	-
UK	5G Centre for Communication Systems Research	5G CCSR (Huawei, Fujitsu, EE, Aircom, BT, Samsung, Telefonica, Vodafone, Aeroflex and Rohde and Schwarz) testing in Surrey University;	EE plans to offer OnePlus 5G smartphone and launch 5G in six cities. Vodafone UK plans to release 5G.	EE launched the 5G network in 6 cities, 2019); Vodafone launched 5G, 2019; O2 launched 5G, 2019;
Spain	5G lab testing - Telefonica/ZTE Corporation .	Vodafone Spain launched 5G trials, 2018. 5G network in Madrid, 2018.	Orange plans to launch 5G in Spain.	Vodafone/Huawei launched the 5G network in 15 Spanish cities, 2019.

high-mobility OFDM system communications such as express railroad trains for 5G wireless networks manage a fading operating environment of time-and frequency-selective-or doubly selective (DS)-fading [311]. The effect of DS fading is due to high Doppler frequency spread (DFS) (i.e., frequency dispersion -time selectivity) and multipath effects (i.e., time dispersion-frequency selectivity) in wireless links [311]. Hence, requiring far more pilots overhead for reliable channel estimation than with an entire frequency selective channel, making the channel estimation task over DS channel extremely challenging for coherent detection [311]. Therefore, channel state information feedback linked closely with the Doppler effect are significant challenges to be overcome in this scenario.

E. MOVING NETWORKS FOR 5G COMMUNICATION SYSTEMS

Combining multi-hop and vehicular communications technologies give the term moving networks. For instance, having a small cell on moving vehicles (i.e., moving relay node) such as trains, buses or cars, connected over a wireless backhaul to a fixed BS [309]. Hence, enabling higher data rates, lower

battery power consumption, and reducing the control overhead. However, the capacity, latency, reliability, and availability of implementing the high-rate wireless backhaul network from the moving cell to a fixed BS, is a significant challenge.

F. MULTIMEDIA COMMUNICATIONS

5G multimedia massive MIMO communication systems improve quality of service (QoS) and quality of experience (QoE) through voice over IP (VoIP) or real-time video streaming in the network. Consequently, enhancing massive MU-MIMO systems QoS/QoE of UEs constitutes an interesting research topic to investigate. Such as the consideration of scalable video coding and cross-layer optimization at the application layer and efficient beamforming and radio resource management at the PHY and MAC layers [309].

G. WIRELESS BACKHAUL

The 5G wireless backhaul network, which can be realized as a wired or wireless solution, serves as a link between the radio access and core networks ensuring connectivity to end-users. The backhaul network would confront the challenges of ultralow latency (i.e., 1 ms) requirements, and ultradense characteristics of the network [309]. The current 5G wireless backhauling depends on wireless technologies realized over P2P or P2MP configurations. Thus, optimal 5G wireless backhaul network deployment and management, besides protecting the backhaul from multiple security threats and attacks, essential for the emerging 5G networks, is an interesting and challenging issue.

H. CELL-FREE MASSIVE MIMO

While inter-cell interference is inherent to network-centric (cell centric) realization, it became a notable drawback with network densification. Cell-free massive MIMO systems enable coherent user-centric transmission realized by a distributed massive MIMO (DM-MIMO) system over a large geographical area to mitigate inter-cell interference constraints in cellular networks with increased macro-diversity [312]–[316]. Specifically, based on the time-division duplex (TDD) operation, geographically distributed antennas systems jointly support limited UEs via a fronthaul network and a CPU within the same time-frequency resource [312]–[314]. Thus, with no cellular or cell boundary conditions,[7] the cell-free massive MIMO is considered a promising technology for 5G indoor and hot-spot coverage scenarios, since it provides comparable QoS capabilities to all UEs with reduced signal processing complexity [312]. In cell-free massive MIMO systems, the access points can efficiently subdue interference among UEs as the unification of small- and large-scale fading causes the high-dimensional channel vectors pairwise nearly orthogonal. However, cell-free MIMO systems encounter increased spatial channel correlation [316], and therefore, proper user grouping and user scheduling algorithms are required to reduce UEs' spatial correlation. Moreover, joint distributed access point selection, and power allocation for cell-free massive MIMO systems is required to achieve reasonable performance in the cellular network [313], [316].

[7]From a channel capacity perspective, cellular networks are suboptimal as higher spectral efficiency (bit/s/Hz/UE) can be realized by employing multiple access points per signal co-processing [312], [313], [316].

I. BEAMSPACE MASSIVE MIMO

While deploying massive MIMO antenna arrays at the BS side can improve cellular system performance, it requires significant additional RF front-end complexity, hardware cost, and power consumption. Hence, the beamspace MIMO based approach is considered as a promising solution to addresses this issue [288], [289]. The fundamental purpose that beamspace MIMO can decrease the number of RF chains is the angular power sparsity found in mmWave massive MIMO channels. However, there is limited literature on the topic of limiting the RF complexity of beamspace massive MIMO systems beyond the beamspace transformation and beam selection. Beamspace massive MIMO is a general approach that underpins hybrid analog-digital precoding/combining. Hybrid analog-digital precoding is likewise anticipated to be the principal enabler for mmWave indoor and outdoor 5G cellular networks. The main challenge in this realization is to tackle link maintenance problems by accurate pointing and tracking over varying environmental conditions. Most existing works in the literature assume that the analog RF precoding and combining matrices are frequency flat and are realized employing a fully-connected architecture with digitally controlled phase (fixed phase) paired quantized phase shifters. However, analog RF precoding and combining matrices are frequency selective, therefore, it is essential to consider the spatial beam pattern distortion of the analog RF precoder and combiner in frequency selective mmWave channels. Recently, there has been a rising trend of employing lens arrays for beamspace massive MIMO.

J. TERAHERTZ BAND CHANNEL MODELING

While the course for higher carrier frequencies which support larger bandwidth is apparent, the entire consecutive available bandwidth for mmWave systems is yet beneath 10 GHz, which renders it challenging to realize Tbps data rates. Notwithstanding, Terahertz (THz) band is widely employed to sub-mmWave energy that occupies the wavelength range between 3 mm - 30 μm (100 GHz - 10 THz) [317]. In the past several decades, the unavailability of practically efficient THz antennas and transceivers caused the THz band among the least investigated frequency ranges in the electromagnetic (EM) spectrum. Nonetheless, significant advancement in the last twelve years is empowering practical realization of THz communication systems [317]–[321]. Following this course, data rates beyond 100 Giga-bit-per-second (100 Gbps) and even Terabit-per-second (Tbps), are foreseen to be realized in the coming three years [317]. In Table 9, we present a comparison between the mmWave band, THz band, infrared, and visible light communication

TABLE 9. Comparison between different wireless communication technologies [324].

Technology	mmWave	THz Band	Infrared	VLC	Ultra-Violet
Frequency Range	30 GHz - 300 GHz	100 GHz - 10 THz	10 THz - 430 THz	430 THz - 790 THz	790 THz - 30 PHz
Wave length	10mm - 1mm	3mm - 30μm	30μm - 698nm	698nm - 380 nm	380 nm - 10nm
Coverage Range	Short	Short/Medium	Relatively low	Relatively low	Relatively low
Network Topology	Point-to-Multipoint (P2MP) topology	P2MP topology	Point-to-point (P2P) topology	P2P topology	P2MP topology
Security	Medium	High	High	High	-
Weather Impairments (WIs)	Robust	Robust	Sensitive	-	Sensitive
Noise Source	Thermal noise	Thermal noise	Ambient noise	Ambient noise	Ambient noise

(VLC) technologies. Besides the previously outlined topics, there are yet several discussions over the specifications of future research directions for channel measurements and models. Future research directions will focus on covering extremely broad spectral bandwidth (i.e., sub-millimeter or Terahertz (THz) bands). The demand for mobile traffic has continuously increased with the development of systems that require data rates in the order of several Gbps up to tens of Gbps. To satisfy the growing demands of such high data rates, two techniques are feasible. Firstly, using devices operating in the 60 GHz band (i.e., the mmWave band, for instance), where spectrum up to 7 GHz, can be used for mobile communications. However, it is still challenging to satisfy systems with high spectral efficiencies beyond 10 bit/s/Hz. Secondly, using devices where extreme bandwidths beyond 20 GHz are available. Such contiguous frequency blocks can solely be found at the sub-millimeter/THz band, i.e., beyond 300 GHz [318]. Therefore, the technology enabling high gain, high directivity, steerable antennas in small form factor becomes the fundamental challenge at THz frequencies, with systems more susceptible to path loss. Concerning the integrated circuit field, increasing the number of transistors on an integrated circuit, which is empirically predicted by Moore's Law [322], permits the application of a large number of antenna elements in a relatively small form factor [1], [2], [318]. In the meanwhile, increasing the data rate in the telecommunication field is shifting towards meeting diverse increased service demands, which is envisioned based on Edholm's law of bandwidth [323]. Hence, the THz band communication has begun to realize considerable attention as a potential solution to 5G and beyond mobile communications. Microsecond latency, seamless high data rate wireless connectivity, huge bandwidth are channel characteristics for THz link wireless communications [318], [321], [324]. The seminal work of [325] utilized the THz term initially to express the spectral line frequency coverage of a Michelson interferometer. Until the early 2000s, the THz spectrum band was formerly referred to as the submillimeter-wave band, although without precise boundary separating the sub-mmWave band and far-infrared [318]. Based on directed NLOS transmissions, the notion of ultra-broadband THz communication was initially introduced in [326], as a potential solution, to support multi-Gbps data rates. The authors in [327] investigate harmonic spurs' effect in THz receiver on communication system performance, and the results validate the presence of harmonic spurs in the receiver with a spur suppression ratio (SSR) less than 20 dB, which significantly impacts the overall system performance. However, the practical results recommend over 30 dB SSR in the downconverted intermediate frequency (IF) signals for realizing below 1 dB interference. To this end, several THz interest group has been newly created, resulting in innovative designs, materials, and fabrication techniques that present endless potentialities for THz improvement. For example, the IEEE 802.15 Terahertz Interest Group (IGthz) [328], [329] has been founded in 2008 to investigate the feasibility of the Terahertz band for wireless communications.

Several measurement campaigns and demonstrations have since been conducted by the different interest groups with diverse technology, demonstrating that wireless communication links at 300 GHz and beyond [330]–[332], are realizable. In [326], basic link budget calculations show that signal attenuation at THz frequencies amounts to around 103.4 dB, with the challenge of too low received signal level, to successfully demodulate the information-bearing signal. Hence, the demand for highly directive (i.e., high-gain) antennas is required to compensate for the high signal attenuation. Hence, Table 10 compares the path loss, potential output powers, antenna type, contiguous bandwidths, and data rates between conventional microwave (at 2.4 GHz, 5 GHz), mmWave (at 60GHz), and THz (at 300 GHz) communications links. Using spatial filtering in beamforming leads to higher gain antennas, which, however, reduces the transmitted power. However, the drawback of very high gain (i.e., high directivity) antennas is the sensitivity to improper position displacement on account of wind conditions and a significant link attachment via ray shadowing. For the impact of antenna directivities on THz propagation channel characteristics, we refer the interested reader to [333] and the references therein. The following challenges have to be satisfied to realize THz communications:

- Channel models for the envisioned applications are remarkably required.
- RF front ends (i.e., circuitry linking a receiver antenna input up to the mixer stage) and antenna theories have to be improved.
- Proper baseband transmission schemes have to be established.
- Standards and regulatory issues require to develop and resolve, respectively.

TABLE 10. Comparison of the conventional microwave, mmWave, and THz communications links [90].

Technology	Data rates	Bandwidths	Antennas Type	Potential output powers	Path loss at 10 m
Macrowave band (at 2.4 GHz, 5 GHz)	600Mbps	40MHz	Omnidirectional ($\backsimeq$ 3 dBi)	22 dBm (Restrained by FCC regulations)	60 dB
mmWave band (at 60 GHz)	4Gbps	$\backsimeq$ 2 GHz	Medium directivities (15 . . . 25 dBi)	10 dBm (Restrained by FCC regulations/communication hardware)	88 dB
THz Band (at 300 GHz)	>100Gbps	10 . . . 100 GHz	High directivities (20 . . . 40 dBi)	$\ll$ 10 dBm (Restrained by communication hardware)	101 dB

1) THz STANDARDIZATION ACTIVITY

Standardization activities have been initiated since 2008 by the IEEE 802.15 organizations THz Interest Group, which aims at designing inter-operable specifications, and to formulate multiple standards specifically for frequency bands up to 3000 GHz. Other than the realization perspectives of THz Communications, there are significant regulatory viewpoints to be examined. For instance, the issues THz communication spectrum resource allocation for passive services, are the topic of the THz interest group. There has been a regular liaison between the IEEE 802.15 organizations THz interest group with both ITU and international radio amateur union (IARU) about the description of spectrum above 275 GHz [318], [321], [324]. Indeed, specific standardization activities for technologies above 275 GHz have been extremely limited until recently. Identifying potential application scenarios and design requirements are the basic tasks of this group, besides following the technological advancement of semiconductor technology to tackle radio channel models and to attend and influence the technical and spectrum regulatory discussions concerning the year 2012 World radio conference (WRC-12). Specifically, comprehensive discussions regarding the prevailing state of semiconductor technologies and photons based designs for production have been addressed in [334] and [335], respectively. In March 2012, review of the results of agenda item 1.6 at WRC-12 and the ITU-R regulations by the THz interest group (IG), to update spectrum use by the passive services within 275 GHz and 3 000 GHz, following Resolution 950 (Rev.WRC-07) [336]. The IG THZ reviewed the prerequisites expected to begin a research group, which involved the support of MAC expertise and bodies from the industry together with the modern PHY contributions. The THz IG upgraded to a study group, in July 2013, with the scope of exploring the validity of a standard on 100G (i.e., 100 Gbps over beam switchable wireless P2P 40/100 Gbps links). In March 2014, as a division of the IG THz, the task group 3d (TG3d) was founded, which operates on an amendment of 802.15.3 proposing 100 Gbitps for switched P2P wireless links [318], [324]. In WRC 2019 [267], agenda item 1.15 attempts to distinguish spectrum for land mobile service (LMS) and fixed service (FS) applications in the 275-450 GHz band, while securing the protection of the present Earth exploration-satellite service (EESS) (passive) including radio astronomy (RAS) applications specified in footnote 5.565 of the radio regulations.

2) THE mmWave BAND VERSUS THz BAND

The mmWave frequencies of 28 GHz, 60 GHz, 39 GHz, and 73 GHz, can coexist with existing wireless and emerging communication systems; and has been adopted by the FCC as the operational frequency of 5G technology. The availability of a larger bandwidth in the mmWave band, which ranges from $7 - 9$ GHz, enables higher data rates. This will consequently limit the channel overall throughput to an inadequate level because of the ever-increasing demand for wireless data traffic. Furthermore, to meet the envisaged data rate of 100 Gbps, communication technology undoubtedly require a challenging spectral efficiency of approximately up to 14 bps/Hz [318]. Furthermore, 5G backhaul (BH) and fronthaul (FH) links for mmWave systems typically require multi-Gbps capacity and latency on the order of a few microseconds. Consequently, venturing into the THz frequency range enables higher link directionality as against the mmWave band, due to the short wavelength of operation, thus leading to lower eavesdropping possibilities. That is, the illegitimate UEs necessarily need to be on the identical narrow beamwidth to intercept data.

IX. CONCLUSION

Bandwidth efficiency remains to be one of the most fundamental metrics in selecting candidate technologies for 5G. While mmWave spectrum is the preferred 5G platform due to its enormous bandwidth, insights in architectures and protocols are required to manage challenges regarding dynamics due to mobility, sensitivity to blockage, high propagation loss, and directivity. This paper provides a comprehensive overview of emerging 5G mmWave propagation characteristics, including the free-space path loss, material penetration loss, rain and foliage induced attenuation, atmospheric induced attenuation, and other propagation factors. Radio-frequency spectrum and regulatory issues, for the 5G channel modeling, have been provided. Existing channel measurement campaigns and modeling approaches for the most challenging 5G systems communication scenarios, such as mmWave communication, massive MIMO communication, multiple access, and performance analysis, have been

extensively reviewed and discussed. Non-stationary property is known to be unique propagation characteristics of massive MIMO channels and consists of AOA shifts at the receiver side and dynamic characteristics of clusters on both the time and array axes, have been discussed. Most importantly, the non-stationary property on both the time and array axes is characterized mainly by birth-death process and cluster visibility region technique. Furthermore, several research contributions that have proposed mmWave channel models for carrier frequencies up to 100 GHz, have also been discussed. Studies on mmWave massive MIMO systems have shown that beamforming with spatial multiplexing approaches can significantly improve system spectral efficiency, network capacity, and overcome interference. To reduce the cost for hardware design, hybrid analog-digital precoding and combining can be jointly realized in both analog and digital domains, to limit the number of required RF chains via constant modulus phase shifters. Hence, we track the development in hybrid analog-digital precoding and combining techniques for mmWave massive MIMO systems, in terms of fully connected and partially connected hybrid transceivers' architectures with the potential antenna configuration scenarios. However, beam search techniques for hybrid analog-digital precoding/combining-based mmWave massive MIMO systems pose a unique set of challenges requiring antenna selection approaches and Low complexity RF beam search algorithms. In the meanwhile, low-complexity iterative algorithms for RF beam search algorithms need to be further investigated. To further improve energy efficiency, switch-based analog combiners are low power and low complexity solutions, realizing a significant reduction in the power consumption per RF chain. That is, for equivalent power consumption, a larger number of RF chains can be employed with switches, which leads to improved spectral efficiency. However, designing optimal combiners utilizing switch-based analog architecture introduces challenging problems since impairments such as noise figure or insertion losses, influence the actual SNR at the input of the digital combiner. We have analyzed the critical issues in the design of multiple-access technologies for mmWave MIMO systems such as NOMA, and random access channel with respect to initial access. By using NOMA, one beam can support two or more UEs with the help of intra-beam superposition coding and SIC, which differs significantly from conventional mmWave massive MIMO systems, where one beam supports only one UE at the same time-frequency resources. The research on random access in hybrid analog-digital precoding and combining based mmWave cellular network is still at its infancy. We foresee that more investigation on random access will be considered, for successful improvement of the mmWave cellular communication, for next-generation 5G mobile broadband. Several research directions for future work have likewise been identified. Lastly, we overview state-of-art techniques of RF-EH and SWIPT-enabled technology for mmWave massive MIMO systems. Subsequently, we review existing SWIPT related literature and then present a detailed description of SWIPT and its antenna design architectures.

REFERENCES

[1] X. Ge, R. Zi, X. Xiong, Q. Li, and L. Wang, "Millimeter wave communications with OAM-SM scheme for future mobile networks," *IEEE J. Sel. Areas Commun.*, vol. 35, no. 9, pp. 2163–2177, Sep. 2017.
[2] O. El Ayach, S. Rajagopal, S. Abu-Surra, Z. Pi, and R. W. Heath, Jr., "Spatially sparse precoding in millimeter wave MIMO systems," *IEEE Trans. wireless Commun.*, vol. 13, no. 3, pp. 1499–1513 Jan. 2014.
[3] Q. C. Li, H. Niu, A. T. Papathanassiou, and G. Wu, "5G network capacity: Key elements and technologies," *IEEE Veh. Technol. Mag.*, vol. 9, no. 1, pp. 71–78, Mar. 2014.
[4] I. A. Hemadeh, K. Satyanarayana, M. El-Hajjar, and L. Hanzo, "Millimeter-wave communications: Physical channel models, design considerations, antenna constructions, and link-budget," *IEEE Commun. Surveys Tuts.*, vol. 20, no. 2, pp. 870–913, 2nd Quart., 2018.
[5] T. S. Rappaport, Y. Xing, G. R. MacCartney, A. F. Molisch, E. Mellios, and J. Zhang, "Overview of millimeter wave communications for fifth-generation (5G) wireless networks—With a focus on propagation models," *IEEE Trans. Antennas Propag.*, vol. 65, no. 12, pp. 6213–6230, Dec. 2017.
[6] A. N. Uwaechia, N. M. Mahyuddin, M. F. Ain, N. M. A. Latiff, and N. F. Za'bah, "On the spectral-efficiency of low-complexity and resolution hybrid precoding and combining transceivers for mmWave MIMO systems," *IEEE Access*, vol. 7, pp. 109259–109277, Aug. 2019.
[7] T. D. Ponnimbaduge Perera, D. N. K. Jayakody, S. K. Sharma, S. Chatzinotas, and J. Li, "Simultaneous wireless information and power transfer (SWIPT): Recent advances and future challenges," *IEEE Commun. Surveys Tuts.*, vol. 20, no. 1, pp. 264–302, 1st Quart., 2018.
[8] B. Bangerter, S. Talwar, R. Arefi, and K. Stewart, "Networks and devices for the 5G era," *IEEE Commun. Mag.*, vol. 52, no. 2, pp. 90–96, Feb. 2014.
[9] K. C. Huang and Z. Wang, *Millimeter Wave Communication Systems*, vol. 29. Hoboken, NJ, USA: Wiley, 2011.
[10] R. Prasad, Ed. *5G Outlook-Innovations and Applications*. Delft, The Netherlands: River Publishers, 2016.
[11] M. A. Abu-Rgheff, *5G Physical Layer Technologies*. Hoboken, NJ, USA: Wiley, 2019.
[12] F. Hu and S. Lucyszyn, "Advances in Front-end Enabling Technologies for Thermal Infrared 'THz torch' Wireless Communications," *J. Infr., Millim., THz Waves*, vol. 37, no. 9, pp. 881–893, Sep. 2016.
[13] L. Dai, B. Wang, M. Peng, and S. Chen, "Hybrid precoding-based millimeter-wave massive MIMO-NOMA with simultaneous wireless information and power transfer," *IEEE J. Sel. Areas Commun.*, vol. 37, no. 1, pp. 131–141, Jan. 2019.
[14] X. Yu, J.-C. Shen, J. Zhang, and K. B. Letaief, "Alternating minimization algorithms for hybrid precoding in millimeter wave MIMO systems," *IEEE J. Sel. Topics Signal Process.*, vol. 10, no. 3, pp. 485–500, Apr. 2016.
[15] X. Wang, L. Kong, F. Kong, F. Qiu, M. Xia, S. Arnon, and G. Chen, "Millimeter wave communication: A comprehensive survey," *IEEE Commun. Surveys Tuts.*, vol. 20, no. 3, pp. 1616–1653, 3rd Quart., 2018.
[16] M. Marcus and B. Pattan, "Millimeter wave propagation: Spectrum management implications," *IEEE Microw. Mag.*, vol. 6, no. 2, pp. 54–62, Jun. 2005.
[17] K. Zheng, L. Zhao, J. Mei, B. Shao, W. Xiang, and L. Hanzo, "Survey of large-scale MIMO systems," *IEEE Commun. Surveys Tuts.*, vol. 17, no. 3, pp. 1738–1760, 3rd Quart., 2015.
[18] W. Roh, J.-Y. Seol, J. Park, B. Lee, J. Lee, Y. Kim, J. Cho, K. Cheun, and F. Aryanfar, "Millimeter-wave beamforming as an enabling technology for 5G cellular communications: Theoretical feasibility and prototype results," *IEEE Commun. Mag.*, vol. 52, no. 2, pp. 106–113, Feb. 2014.
[19] Z. Pi and F. Khan, "A millimeter-wave massive MIMO system for next generation mobile broadband," in *Proc. Conf. Rec. Forty 6th Asilomar Conf. Signals, Syst. Comput. (ASILOMAR)*, Nov. 2012, pp. 693–698.
[20] S. K. Yong and C.-C. Chong, "An overview of multigigabit wireless through millimeter wave technology: Potentials and technical challenges," *EURASIP J. Wireless Commun. Netw.*, vol. 2007, no. 1, p. 50, Dec. 2006.
[21] F. E. Mahmouli and S. D. Walker, "4-Gbps uncompressed video transmission over a 60-GHz orbital angular momentum wireless channel," *IEEE Wireless Commun. Lett.*, vol. 2, no. 2, pp. 223–226, Apr. 2013.

[22] E. Torkildson, B. Ananthasubramaniam, U. Madhow, and M. Rodwell, "Millimeter-wave MIMO: Wireless links at optical speeds," in *Proc. 44th Allerton Conf. Commun., Control Comput.*, 2006, pp. 1–9.

[23] A. I. Sulyman, A. Alwarafy, G. R. MacCartney, T. S. Rappaport, and A. Alsanie, "Directional radio propagation path loss models for millimeter-wave wireless networks in the 28-, 60-, and 73-GHz bands," *IEEE Trans. Wireless Commun.*, vol. 15, no. 10, pp. 6939–6947, Oct. 2016.

[24] A. Alkhateeb, J. Mo, N. Gonzalez-Prelcic, and R. W. Heath, Jr., "MIMO precoding and combining solutions for millimeter-wave systems," *IEEE Commun. Mag.*, vol. 52, no. 12, pp. 122–131, Dec. 2014.

[25] R. W. Heath, Jr., N. Gonzalez-Prelcic, S. Rangan, W. Roh, and A. M. Sayeed, "An overview of signal processing techniques for millimeter wave MIMO systems," *IEEE J. Sel. Topics Signal Process.*, vol. 10, no. 3, pp. 436–453, Apr. 2016.

[26] O. Andrisano, V. Tralli, and R. Verdone, "Millimeter waves for short-range multimedia communication systems," *Proc. IEEE*, vol. 86, no. 7, pp. 1383–1401, Jul. 1998.

[27] A. Alkhateeb, O. El Ayach, G. Leus, and R. W. Heath, Jr., "Hybrid precoding for millimeter wave cellular systems with partial channel knowledge," in *Proc. Inf. Theory Appl. Workshop (ITA)*, San Diego, CA, USA, Feb. 2013, pp. 1–5.

[28] Y. Ren, Y. Wang, C. Qi, and Y. Liu, "Multiple-beam selection with limited feedback for hybrid beamforming in massive MIMO systems," *IEEE Access*, vol. 5, pp. 13327–13335, 2017.

[29] F. Sohrabi and W. Yu, "Hybrid analog and digital beamforming for mmWave OFDM large-scale antenna arrays," *IEEE J. Sel. Areas Commun.*, vol. 35, no. 7, pp. 1432–1443, Jul. 2017.

[30] S. Park, A. Alkhateeb, and R. W. Heath, Jr., "Dynamic subarrays for hybrid precoding in wideband mmWave MIMO systems," *IEEE Trans. Wireless Commun.*, vol. 16, no. 5, pp. 2907–2920, May 2017.

[31] *Technical Feasibility of IMT in Bands Above 6 GHz*, document ITU-R M.2376-0, ITU-R, International Telecommunication Union, 2015. [Online]. Available: https://www.itu.int/dms_pub/itu-r/opb/rep/R-REP-M.2376-2015-PDF-E.pdf

[32] *Study on 3D Channel Model for LTE*, document TR 36.873, 3GPP, 2015.

[33] Federal Communications Commission. (Jul. 2016). *Spectrum Frontiers Report and Order and Further Notice of Proposed Rulemaking: FCC16-89*. [Online]. Available: https://docs.fcc.gov/public/attachments/FCC-16-89A1.pdf

[34] *IEEE 802.15 WPAN Millimeter Wave Alternative PHY Task Group 3c (TG3c)*. [Online]. Available: http://www.ieee802.org/15/pub/TG3c.html

[35] P. Kumari, N. Gonzalez-Prelcic, and R. W. Heath, Jr., "IEEE 802.11ad-based radar: An approach to joint vehicular communication-radar system," in *Proc. IEEE 82nd Veh. Technol. Conf. (VTC-Fall)*, Feb. 2015, pp. 1–5.

[36] T. Siriburanon, S. Kondo, M. Katsuragi, H. Liu, K. Kimura, W. Deng, K. Okada, and A. Matsuzawa, "A low-power low-noise mm-wave sub-sampling PLL using dual-step-mixing ILFD and tail-coupling quadrature injection-locked oscillator for IEEE 802.11ad," *IEEE J. Solid-State Circuits*, vol. 51, no. 5, pp. 1246–1260, May 2016.

[37] H. Ajorloo and M. T. Manzuri-Shalmani, "Modeling beacon period length of the UWB and 60-GHz mmWave WPANs based on ECMA-368 and ECMA-387 standards," *IEEE Trans. Mobile Comput.*, vol. 12, no. 6, pp. 1201–1213, Jun. 2013.

[38] F. Barale, P. Sen, S. Sarkar, S. Pinel, and J. Laskar, "A 60 GHz-standard compatible programmable 50 GHz phase-locked loop in 90 nm CMOS," *IEEE Microw. Wireless Compon. Lett.*, vol. 20, no. 7, pp. 411–413, Jul. 2010.

[39] K. Button, *Infrared and Millimeter Waves V4: Millimeter Systems* (Infrared and Millimeter Waves). Amsterdam, The Netherlands: Elsevier, 2014. [Online]. Available: https://books.google.co.uk/books?id=_D9HvmdlTS4C

[40] A. Natarajan, A. Komijani, X. Guan, A. Babakhani, and A. Hajimiri, "A 77-GHz phased-array transceiver with on-chip antennas in silicon: Transmitter and local LO-path phase shifting," *IEEE J. Solid-State Circuits*, vol. 41, no. 12, pp. 2807–2819, Dec. 2006.

[41] J. W. Dees, R. J. Wangler, and J. C. Wiltse, "System considerations for millimeter wave satellite communications," *IEEE Trans. Aerosp. Electron. Syst.*, vols. AES–2, no. 6, pp. 195–213, Nov. 1966.

[42] E. Damosso, L. Stola, and G. Brussaard, "Characterisation of the 50-70 Ghz band for space communications," *ESA J.*, vol. 7, no. 1, pp. 25–43, 1983.

[43] L. A. Hoffman and K. H. Hurlbut, "A 94-GHz RADAR for space object identification," in *Proc. G-MTT Int. Microw. Symp.*, Dallas, TX, USA, May 1969, pp. 475–484.

[44] W. O. Copeland, J. R. Ashwell, G. P. Kefalas, and J. C. Wiltse, "Millimeter-wave systems applications," in *Proc. G-MTT Int. Microw. Symp.*, Dallas, TX, USA, May 1969, pp. 485–488.

[45] H. H. Meinel, "System design, applications and development trends in the millimeter-wave range," in *Proc. 18th Eur. Microw. Conf.*, Stockholm, Sweden, Oct. 1988, pp. 1203–1217.

[46] T. S. Rappaport, G. R. MacCartney, M. K. Samimi, and S. Sun, "Wideband millimeter-wave propagation measurements and channel models for future wireless communication system design," *IEEE Trans. Commun.*, vol. 63, no. 9, pp. 3029–3056, Sep. 2015.

[47] W. Hong, K.-H. Baek, Y. Lee, Y. Kim, and S.-T. Ko, "Study and prototyping of practically large-scale mmWave antenna systems for 5G cellular devices," *IEEE Commun. Mag.*, vol. 52, no. 9, pp. 63–69, Sep. 2014.

[48] T. S. Rappaport, F. Gutierrez, E. Ben-Dor, J. N. Murdock, Y. Qiao, and J. I. Tamir, "Broadband millimeter-wave propagation measurements and models using adaptive-beam antennas for outdoor urban cellular communications," *IEEE Trans. Antennas Propag.*, vol. 61, no. 4, pp. 1850–1859, Apr. 2013.

[49] H. Xu, V. Kukshya, and T. S. Rappaport, "Spatial and temporal characteristics of 60-GHz indoor channels," *IEEE J. Sel. Areas Commun.*, vol. 20, no. 3, pp. 620–630, Apr. 2002.

[50] S. Nie, M. K. Samimi, T. Wu, S. Deng, G. R. MacCartney, Jr., and T. S. Rappaport, "73 GHz millimeter-wave indoor and foliage propagation channel measurements and results," NYU Wireless, Brooklyn, NY, USA, Tech. Rep. TR-2014-003, 2014.

[51] G. Zhang, K. Saito, W. Fan, X. Cai, P. Hanpinitsak, J.-I. Takada, and G. F. Pedersen, "Experimental characterization of millimeter-wave indoor propagation channels at 28 GHz," *IEEE Access*, vol. 6, pp. 76516–76526, 2018.

[52] M. Alloulah and H. Huang, "Future millimeter-wave indoor systems: A blueprint for joint communication and sensing," *Computer*, vol. 52, no. 7, pp. 16–24, Jul. 2019.

[53] G. R. Maccartney, T. S. Rappaport, S. Sun, and S. Deng, "Indoor office wideband millimeter-wave propagation measurements and channel models at 28 and 73 GHz for ultra-dense 5G wireless networks," *IEEE Access*, vol. 3, pp. 2388–2424, 2015.

[54] X. Wu, C.-X. Wang, J. Sun, J. Huang, R. Feng, Y. Yang, and X. Ge, "60-GHz millimeter-wave channel measurements and modeling for indoor office environments," *IEEE Trans. Antennas Propag.*, vol. 65, no. 4, pp. 1912–1924, Apr. 2017.

[55] H. Zhao, R. Mayzus, S. Sun, M. Samimi, J. K. Schulz, Y. Azar, K. Wang, G. N. Wong, F. Gutierrez, and T. S. Rappaport, "28 GHz millimeter wave cellular communication measurements for reflection and penetration loss in and around buildings in New York city," in *Proc. IEEE Int. Conf. Commun. (ICC)*, Jun. 2013, pp. 5163–5167.

[56] H.-S. Lee, M. Park, and B.-W. Min, "A 26-GHz transmitter front-end using double quadrature architecture," *PLoS ONE*, vol. 14, no. 5, 2019, Art. no. e0216474.

[57] X. Yang, M. Matthaiou, J. Yang, C.-K. Wen, F. Gao, and S. Jin, "Hardware-constrained millimeter-wave systems for 5G: Challenges, opportunities, and solutions," *IEEE Commun. Mag.*, vol. 57, no. 1, pp. 44–50, Jan. 2019.

[58] S. Dutta, M. Mezzavilla, R. Ford, M. Zhang, S. Rangan, and M. Zorzi, "Frame structure design and analysis for millimeter wave cellular systems," *IEEE Trans. Wireless Commun.*, vol. 16, no. 3, pp. 1508–1522, Mar. 2017.

[59] S. Dutta, M. Mezzavilla, R. Ford, M. Zhang, S. Rangan, and M. Zorzi, "MAC layer frame design for millimeter wave cellular system," in *Proc. Eur. Conf. Netw. Commun. (EuCNC)*, Jun. 2016, pp. 117–121.

[60] R. Ford, M. Zhang, M. Mezzavilla, S. Dutta, S. Rangan, and M. Zorzi, "Achieving ultra-low latency in 5G millimeter wave cellular networks," *IEEE Commun. Mag.*, vol. 55, no. 3, pp. 196–203, Mar. 2017.

[61] H. Shokri-Ghadikolaei, C. Fischione, P. Popovski, and M. Zorzi, "Design aspects of short-range millimeter-wave networks: A MAC layer perspective," *IEEE Netw.*, vol. 30, no. 3, pp. 88–96, May 2016.

[62] G. Hong, T. Nitsche, and J. C. Widmer, "Addressing MAC layer inefficiency and deafness of IEEE802.11ad millimeter wave networks using a multi-band approach," in *Proc. IEEE 27th Annu. Int. Symp. Pers., Indoor, Mobile Radio Commun. (PIMRC)*, Sep. 2016, pp. 1–6.

[63] M. Park, C. Cordeiro, E. Perahia, and L. L. Yang, "Millimeter-wave multi-gigabit WLAN: Challenges and feasibility," in *Proc. IEEE 19th Int. Symp. Pers., Indoor Mobile Radio Commun.*, Sep. 2008, pp. 1–5.
[64] Y. Nagai, M. Ochiai, A. Taira, T. Yamauchi, N. Shimizu, and A. Shibuya, "On the design of a point-to-multipoint gigabit WLAN system on 60 GHz millimeter wave," in *Proc. 6th IEEE Consum. Commun. Netw. Conf.*, Jan. 2009, pp. 1–5.
[65] R. Baldemair, T. Irnich, K. Balachandran, E. Dahlman, G. Mildh, Y. Selén, S. Parkvall, M. Meyer, and A. Osseiran, "Ultra-dense networks in millimeter-wave frequencies," *IEEE Commun. Mag.*, vol. 53, no. 1, pp. 202–208, Jan. 2015.
[66] M. Alkhawatra and N. Qasem, "Improving and extending indoor connectivity using relay nodes for 60 GHz applications," *Int. J. Adv. Comput. Sci. Appl.*, vol. 7, no. 4, pp. 427–434, 2016.
[67] M. Soleimani, M. H. MacGregor, R. Kerslake, P. Mousavi, and M. M. Bhuiyan, "RF channel modelling and multi-hop routing for wireless sensor networks located on oil rigs," *IET Wireless Sensor Syst.*, vol. 6, no. 5, pp. 173–179, Oct. 2016.
[68] F. S. Shaikh and R. Wismuller, "Routing in multi-hop cellular device-to-device (D2D) networks: A survey," *IEEE Commun. Surveys Tuts.*, vol. 20, no. 4, pp. 2622–2657, 4th Quart., 2018.
[69] Y. Liu, X. Chen, Y. Niu, B. Ai, Y. Li, and D. Jin, "Mobility-aware transmission scheduling scheme for millimeter-wave cells," *IEEE Trans. Wireless Commun.*, vol. 17, no. 9, pp. 5991–6004, Sep. 2018.
[70] H. Jung and I.-H. Lee, "Performance analysis of millimeter-wave multi-hop Machine-to-Machine networks based on hop distance statistics," *Sensors*, vol. 18, no. 2, p. 204, 2018.
[71] Z. Wei, X. Zhu, S. Sun, Y. Huang, A. Al-Tahmeesschi, and Y. Jiang, "Energy-efficiency of millimeter-wave full-duplex relaying systems: Challenges and solutions," *IEEE Access*, vol. 4, pp. 4848–4860, 2016.
[72] I. Ahmed, H. Khammari, A. Shahid, A. Musa, K. S. Kim, E. De Poorter, and I. Moerman, "A survey on hybrid beamforming techniques in 5G: Architecture and system model perspectives," *IEEE Commun. Surveys Tuts.*, vol. 20, no. 4, pp. 3060–3097, 4th Quart., 2018.
[73] S. A. Busari, K. M. S. Huq, S. Mumtaz, L. Dai, and J. Rodriguez, "Millimeter-wave massive MIMO communication for future wireless systems: A survey," *IEEE Commun. Surveys Tuts.*, vol. 20, no. 2, pp. 836–869, 2nd Quart., 2018.
[74] T. S. Rappaport, S. Sun, R. Mayzus, H. Zhao, Y. Azar, K. Wang, G. N. Wong, J. K. Schulz, M. Samimi, and F. Gutierrez, "Millimeter wave mobile communications for 5G cellular: It will work!," *IEEE Access*, vol. 1, pp. 335–349, 2013.
[75] S. Rangan, T. S. Rappaport, and E. Erkip, "Millimeter-wave cellular wireless networks: Potentials and challenges," *Proc. IEEE*, vol. 102, no. 3, pp. 366–385, Mar. 2014.
[76] A. Ghosh, T. A. Thomas, M. C. Cudak, R. Ratasuk, P. Moorut, F. W. Vook, T. S. Rappaport, G. R. MacCartney, S. Sun, and S. Nie, "Millimeter-wave enhanced local area systems: A High-Data-Rate approach for future wireless networks," *IEEE J. Sel. Areas Commun.*, vol. 32, no. 6, pp. 1152–1163, Jun. 2014.
[77] C. Dehos, J. L. González, A. D. Domenico, D. Kténas, and L. Dussopt, "Millimeter-wave access and backhauling: The solution to the exponential data traffic increase in 5G mobile communications systems?" *IEEE Commun. Mag.*, vol. 52, no. 9, pp. 88–95, Sep. 2014.
[78] J. G. Andrews, T. Bai, M. N. Kulkarni, A. Alkhateeb, A. K. Gupta, and R. W. Heath, Jr., "Modeling and analyzing millimeter wave cellular systems," *IEEE Trans. Commun.*, vol. 65, no. 1, pp. 403–430, Jan. 2016.
[79] X. Lu, P. Wang, D. Niyato, D. I. Kim, and Z. Han, "Wireless networks with RF energy harvesting: A contemporary survey," *IEEE Commun. Surveys Tuts.*, vol. 17, no. 2, pp. 757–789, 2nd Quart., 2015.
[80] I. Krikidis, S. Timotheou, S. Nikolaou, G. Zheng, D. W. K. Ng, and R. Schober, "Simultaneous wireless information and power transfer in modern communication systems," *IEEE Commun. Mag.*, vol. 52, no. 11, pp. 104–110, Nov. 2014.
[81] C.-X. Wang, J. Bian, J. Sun, W. Zhang, and M. Zhang, "A survey of 5G channel measurements and models," *IEEE Commun. Surveys Tuts.*, vol. 20, no. 4, pp. 3142–3168, 4th Quart., 2018.
[82] D. C. Araújo, T. Maksymyuk, A. L. F. de Almeida, T. Maciel, J. C. M. Mota, and M. Jo, "Massive MIMO: Survey and future research topics," *IET Commun.*, vol. 10, no. 15, pp. 1938–1946, Oct. 2016.
[83] J. Ryan, G. R. MacCartney, and T. S. Rappaport, "Indoor office wideband penetration loss measurements at 73 GHz," in *Proc. IEEE Int. Conf. Commun. Workshops (ICC Workshops)*, May 2017, pp. 1–6.
[84] W. Weichselberger, M. Herdin, H. Ozcelik, and E. Bonek, "A stochastic MIMO channel model with joint correlation of both link ends," *IEEE Trans. Wireless Commun.*, vol. 5, no. 1, pp. 90–100, Jan. 2006.
[85] G. R. MacCartney, M. K. Samimi, and T. S. Rappaport, "Omnidirectional path loss models in New York City at 28 GHz and 73 GHz," in *Proc. IEEE 25th Annu. Int. Symp. Pers., Indoor, Mobile Radio Commun. (PIMRC)*, Sep. 2014, pp. 227–231.
[86] H. Singh, R. Prasad, and B. Bonev, "The studies of millimeter waves at 60 GHz in outdoor environments for IMT applications: A state of art," *Wireless Pers. Commun.*, vol. 100, no. 2, pp. 463–474, May 2018.
[87] S. K. Yong, P. Xia, and A. Valdes-Garcia, *60 GHz Technology for Gbps WLAN and WPAN: From Theory to Practice*. Hoboken, NJ, USA: Wiley, 2011.
[88] W. Haiming, H. Wei, C. Jixin, S. Bo, and P. Xiaoming, "IEEE 802.11aj (45 GHz): A new very high throughput millimeter-wave WLAN system," *China Commun.*, vol. 11, no. 6, pp. 51–62, 2014.
[89] J. Ryan, G. R. MacCartney, and T. S. Rappaport, "Indoor office wideband penetration loss measurements at 73 GHz," in *Proc. IEEE Int. Conf. Commun. Workshops (ICC Workshops)*, May 2017, pp. 228–233.
[90] T. Kürner and S. Priebe, "Towards THz communications-status in research, standardization and regulation," *J. Infr., Millim., THz Waves*, vol. 35, no. 1, pp. 53–62, Jan. 2014.
[91] (Dec. 12, 2019). *Current 5G Commercial Network Including Current 5G Research, 5G Field Testing/5G Trials, and 5G Development by Country*. [Online]. Available: https://www.worldtimezone.com/5g.html
[92] M. J. Marcus, "Spectrum policy issues for millimeter wave mobile communications," *IEEE Wireless Commun.*, vol. 21, no. 6, pp. 8–9, Dec. 2014.
[93] W. Nawrocki, *Measurement Systems and Sensors*. Norwood, MA, USA: Artech House, 2016.
[94] M. Hasan, J. M. Thakur, and P. Podder, "Design and implementation of FHSS and DSSS for secure data transmission," *Int. J. Signal Process. Syst.*, vol. 4, no. 2, pp. 144–149, 2015.
[95] J. Qiao, X. Shen, J. W. Mark, and Y. He, "MAC-layer concurrent beamforming protocol for indoor millimeter-wave networks," *IEEE Trans. Veh. Technol.*, vol. 64, no. 1, pp. 327–338, Jan. 2015.
[96] O. Jo, S. Chang, C. Kweon, J. Oh, and K. Cheun, "60 GHz wireless communication for future Wi-Fi," *ICT Express*, vol. 1, no. 1, pp. 30–33, 2015.
[97] K. Sakaguchi, E. M. Mohamed, H. Kusano, M. Mizukami, S. Miyamoto, R. E. Rezagah, K. Takinami, K. Takahashi, N. Shirakata, H. Peng, T. Yamamoto, and S. Nanba, "Millimeter-wave wireless LAN and its extension toward 5G heterogeneous networks," *IEICE Trans. Commun.*, vol. E98.B, no. 10, pp. 1932–1948, 2015.
[98] A. M. Al-Samman, M. H. Azmi, and T. A. Rahman, "A survey of millimeter wave (mm-Wave) communications for 5G: Channel measurement below and above 6 GHz," in *Proc. Int. Conf. Reliable Inf. Commun. Technol.* Cham, Switzerland: Springer, 2019. pp. 451–463.
[99] R. Mendez-Rial, C. Rusu, N. Gonzalez-Prelcic, A. Alkhateeb, and R. W. Heath, Jr., "Hybrid MIMO architectures for millimeter wave communications: Phase shifters or switches?" *IEEE Access*, vol. 4, pp. 247–267, 2016.
[100] S. Ghosh and D. Sen, "An inclusive survey on array antenna design for millimeter-wave communications," *IEEE Access*, vol. 7, pp. 83137–83161, 2019.
[101] Q. Li, W.-J. Lu, S.-G. Wang, and L. Zhu, "Planar quasi-isotropic magnetic dipole antenna using fractional-order circular sector cavity resonant mode," *IEEE Access*, vol. 5, pp. 8515–8525, 2017.
[102] Z. Nossire, N. Gupta, L. Almazaydeh, and X. Xiong, "New empirical path loss model for 28 GHz and 38 GHz millimeter wave in indoor urban under various conditions," *Appl. Sci.*, vol. 8, no. 11, p. 2122, 2018.
[103] T. Manning, *Microwave Radio Transmission Design Guide*. Norwood, MA, USA: Artech House, 2009.
[104] K. Pahlavan and P. Krishnamurthy, *Principles of Wireless Access and Localization*. Hoboken, NJ, USA: Wiley, 2013.
[105] A. Mauludiyanto, G. Hendrantoro, M. H. Purnomo, T. Ramadhany, and A. Matsushima, "ARIMA modeling of tropical rain attenuation on a short 28-GHz terrestrial link," *IEEE Antennas Wireless Propag. Lett.*, vol. 9, pp. 223–227, Feb. 2010.
[106] D. Nandi and A. Maitra, "The effects of rain on millimeter wave communication for tropical region," in *Proc. URSI Asia–Pacific Radio Sci. Conf. (AP-RASC)*, Mar. 2019, pp. 1–3.

[107] S. Shrestha and D.-Y. Choi, "Rain attenuation study over an 18 GHz terrestrial microwave link in South Korea," *Int. J. Antennas Propag.*, vol. 2019, pp. 1–16, Mar. 2019.

[108] I. Shayea, T. A. Rahman, M. H. Azmi, and M. R. Islam, "Real measurement study for rain rate and rain attenuation conducted over 26 GHz microwave 5G link system in malaysia," *IEEE Access*, vol. 6, pp. 19044–19064, 2018.

[109] M. S. J. Singh, S. I. S. Hassan, M. F. Ain, F. Ghani, K. Igarashi, K. Tanaka, and M. Iida, "Rain attenuation model for south east asia countries," *Electron. Lett.*, vol. 43, no. 2, pp. 75–77, 2007.

[110] K. C. Allen, H. J. Liebe, and C. M. Rush, "Estimates of millimeter wave attenuation for 18 United States cities," NASA STI/Recon, Tech. Rep. N 84, 1983. [Online]. Available: https://www.its.bldrdoc.gov/publications/download/83-119_ocr.pdf

[111] H. M. Rahim, C. Y. Leow, and T. A. Rahman, "Millimeter wave propagation through foliage: Comparison of models," in *Proc. IEEE 12th Malaysia Int. Conf. Commun. (MICC)*, Nov. 2015, pp. 236–240.

[112] A. Ghasemi, A. Abedi, and F. Ghasemi, *Propagation Engineering in Wireless Communications*. Berlin, Germany: Springer, 2012, p. 64.

[113] U. A. Korai, L. Luini, R. Nebuloni, and I. Glesk, "Statistics of attenuation due to rain affecting hybrid FSO/RF link: Application for 5G networks," in *Proc. 11th Eur. Conf. Antennas Propag. (EUCAP)*, Mar. 2017, pp. 1789–1792.

[114] S. Shrestha and D.-Y. Choi, "Rain attenuation over terrestrial microwave links in South Korea," *IET Microw., Antennas Propag.*, vol. 11, no. 7, pp. 1031–1039, Jun. 2017.

[115] F. C. M. Filho, R. S. Cole, and A. D. Sarma, "Millimetre-wave rain induced attenuation: Theory and experiment," *IEE Proc. H Microw., Antennas Propag.*, vol. 133, no. 4, pp. 308–314, 1986.

[116] S. Joshi, S. Sancheti, and A. Goyal, "Rain attenuation measurements for short-range millimetre-wave radio link," *Electron. Lett.*, vol. 42, no. 2, pp. 72–74, 2006.

[117] J. Sander, "Rain attenuation of millimeter waves at $\lambda = 77$, 3.3, 2 mm," *IEEE Trans. Antennas Propag.*, vol. 23, no. 2, pp. 213–220, Aug. 1975.

[118] A. K. M. Isa, A. Nix, and G. Hilton, "Impact of diffraction and attenuation for material characterisation in millimetre wave bands," in *Proc. Loughborough Antennas Propag. Conf. (LAPC)*, Nov. 2015, pp. 1–4.

[119] K. Sato, T. Manabe, T. Ihara, H. Saito, S. Ito, T. Tanaka, K. Sugai, N. Ohmi, Y. Murakami, M. Shibayama, Y. Konishi, and T. Kimura, "Measurements of reflection and transmission characteristics of interior structures of office building in the 60-GHz band," *IEEE Trans. Antennas Propag.*, vol. 45, no. 12, pp. 1783–1792, Dec. 1997.

[120] Q. Wang, X. Zhao, S. Li, M. Wang, S. Sun, and W. Hong, "Attenuation by a human body and trees as well as material penetration loss in 26 and 39 GHz millimeter wave bands," *Int. J. Antennas Propag.*, vol. 2017, pp. 1–8, 2017.

[121] T. S. Rappaport and S. Deng, "73 GHz wideband millimeter-wave foliage and ground reflection measurements and models," in *Proc. IEEE Int. Conf. Commun. Workshop (ICCW)*, Jun. 2015, pp. 1238–1243.

[122] P. Papazian and Y. Lo, "Seasonal variability of a local multi-point distribution service radio channel," in *Proc. IEEE Radio Wireless Conf. (RAWCON)*, Aug. 1999, pp. 211–214.

[123] W. J. Vogel and J. Goldhirsh, "Earth-satellite tree attenuation at 20 GHz: Foliage effects," *Electron. Lett.*, vol. 29, no. 18, pp. 1640–1641, 1993.

[124] F. K. Schwering, E. J. Violette, and R. H. Espeland, "Millimeter-wave propagation in vegetation: Experiments and theory," *IEEE Trans. Geosci. Remote Sens.*, vol. 26, no. 3, pp. 355–367, May 1988.

[125] H. Xu, T. S. Rappaport, R. J. Boyle, and J. H. Schaffner, "Measurements and models for 38-GHz point-to-multipoint radiowave propagation," *IEEE J. Sel. Areas Commun.*, vol. 18, no. 3, pp. 310–321, Mar. 2000.

[126] I. J. Dilworth, "Propagation effects due to foliage and building scatter at millimetre wavelengths," in *Proc. 9th Int. Conf. Antennas Propag. (ICAP)*, 1995, pp. 2–51.

[127] Y. Zhang, D. J. Love, N. Michelusi, J. V. Krogmeier, S. Jyoti, A. Sprintson, and C. R. Anderson, "Improving millimeter-wave channel models for suburban environments with site-specific geometric features," in *Proc. Int. Appl. Comput. Electromagn. Soc. Symp. (ACES)*, Mar. 2018, pp. 1–2.

[128] E. J. Violette, R. H. Espeland, R. O. DeBolt, and F. K. Schwering, "Millimeter-wave propagation at street level in an urban environment," *IEEE Trans. Geosci. Remote Sens.*, vol. 26, no. 3, pp. 368–380, May 1988.

[129] Y. Xing, O. Kanhere, S. Ju, T. S. Rappaport, and G. R. MacCartney, "Verification and calibration of antenna cross-polarization discrimination and penetration loss for millimeter wave communications," in *Proc. IEEE 88th Veh. Technol. Conf. (VTC-Fall)*, Aug. 2018, pp. 1–6.

[130] A. S. Abdulrasool, J. S. Aziz, and S. J. Abou-Loukh, "Calculation algorithm for diffraction losses of multiple obstacles based on Epstein–Peterson approach," *Int. J. Antennas Propag.*, vol. 2017, pp. 1–9, 2017.

[131] A. S. Glassner, Ed., *An Introduction to Ray Tracing*. Amsterdam, The Netherlands: Elsevier, 1989.

[132] D. Chikhale and S. Deosarkar, "Recent trends in millimeter wave communication," in *Proc. Int. Conf. Commun. Signal Process. (ICCASP)*, 2017, pp. 586–591.

[133] J. Senic, C. Gentile, P. B. Papazian, K. A. Remley, and J.-K. Choi, "Analysis of E-Band path loss and propagation mechanisms in the indoor environment," *IEEE Trans. Antennas Propag.*, vol. 65, no. 12, pp. 6562–6573, Dec. 2017.

[134] T. S. Rappaport, *Wireless Communications: Principles and Practice*, vol. 2. Upper Saddle River, NJ, USA: Prentice-Hall, 1996.

[135] H. N. Mahjoub, A. Tahmasbi-Sarvestani, S. M. O. Gani, and Y. P. Fallah, "Composite $\alpha - \mu$ based DSRC channel model using large data set of RSSI measurements," *IEEE Trans. Intell. Transp. Syst.*, vol. 20, no. 1, pp. 205–217, Jan. 2019.

[136] G. R. MacCartney and T. S. Rappaport, "Rural macrocell path loss models for millimeter wave wireless communications," *IEEE J. Sel. Areas Commun.*, vol. 35, no. 7, pp. 1663–1677, Jul. 2017.

[137] M. B. Majed, T. A. Rahman, O. A. Aziz, M. N. Hindia, and E. Hanafi, "Channel characterization and path loss modeling in indoor environment at 4.5, 28, and 38 GHz for 5G cellular networks," *Int. J. Antennas Propag.*, vol. 2018, Sep. 2018, Art. no. 9142367.

[138] M. Khalily, M. Ghoraishi, S. Taheri, S. Payami, and R. Tafazolli, "Millimeter-wave directional path loss models in the 26 GHz, 32 GHz, and 39 GHz bands for small cell 5G cellular system," in *Proc. EuCAP*, Apr. 2018, pp. 17–25.

[139] S. Deng, M. K. Samimi, and T. S. Rappaport, "28 GHz and 73 GHz millimeter-wave indoor propagation measurements and path loss models," in *Proc. IEEE Int. Conf. Commun. Workshop (ICCW)*, Jun. 2015, pp. 1244–1250.

[140] Y. C. Eldar, P. Kuppinger, and H. Bolcskei, "Block-sparse signals: Uncertainty relations and efficient recovery," *IEEE Trans. Signal Process.*, vol. 58, no. 6, pp. 3042–3054, Jun. 2010.

[141] J. Brady, N. Behdad, and A. M. Sayeed, "Beamspace MIMO for millimeter-wave communications: System architecture, modeling, analysis, and measurements," *IEEE Trans. Antennas Propag.*, vol. 61, no. 7, pp. 3814–3827, Jul. 2013.

[142] K. Zheng, S. Ou, and X. Yin, "Massive MIMO channel models: A survey," *Int. J. Antennas Propag.*, vol. 2014, pp. 1–10, Jun. 2014.

[143] Y. Bouchoucha, K. Kheireddine, and S. Hasnaoui, "Beamforming using linear antenna arrays for photonic applications," in *Proc. Int. Conf. Internet Things, Embedded Syst. Commun. (IINTEC)*, Dec. 2018, pp. 59–63.

[144] A. Recioui, "Sidelobe level reduction in linear array pattern synthesis using particle swarm optimization," *J. Optim. Theory Appl.*, vol. 153, no. 2, pp. 497–512, May 2012.

[145] E. Rajo-Iglesias and O. Quevedo-Teruel, "Linear array synthesis using an ant-colony-optimization-based algorithm," *IEEE Antennas Propag. Mag.*, vol. 49, no. 2, pp. 70–79, Apr. 2007.

[146] U. Singh, H. Kumar, and T. S. Kamal, "Linear array synthesis using biogeography based optimization," *Prog. Electromagn. Res.*, vol. 11, pp. 25–36, 2010.

[147] H. Singh, H. L. Sneha, and R. M. Jha, "Mutual coupling in phased arrays: A review," *Int. J. Antennas Propag.*, vol. 2013, pp. 1–23, 2013.

[148] P. Ioannides and C. A. Balanis, "Uniform circular arrays for smart antennas," *IEEE Antennas Propag. Mag.*, vol. 47, no. 4, pp. 192–206, 2005.

[149] P. Ioannides and C. A. Balanis, "Uniform circular and rectangular arrays for adaptive beamforming applications," *IEEE Antennas Wireless Propag. Lett.*, vol. 4, pp. 351–354, 2005.

[150] M. I. Dessouky, H. A. Sharshar, and Y. A. Albagory, "Efficient sidelobe reduction technique for small-sized concentric circular arrays," *Prog. Electromagn. Res.*, vol. 65, pp. 187–200, Jan. 2006.

[151] F. Gozasht, G. R. Dadashzadeh, and S. Nikmhr, "A comprehensive performance study of circular and hexagonal array geometreis in the LMS algorithem for smart antenna applications," *Prog. Electromagn. Res.*, vol. 68, pp. 281–296, 2007.

[152] K. R. Mahmoud, M. El-Adawy, S. M. M. Ibrahem, R. Bansal, and S. H. Zainud-Deen, "A comparison between circular and hexagonal array geometries for smart antenna systems using particle swarm optimization algorithm," *Prog. Electromagn. Res.*, vol. 72, pp. 75–90, 2007.
[153] C.-M. Chen, V. Volskiy, A. Chiumento, L. Van der Perre, G. A. E. Vandenbosch, and S. Pollin, "Exploration of user separation capabilities by distributed large antenna arrays," in *Proc. IEEE Globecom Workshops (GC Wkshps)*, Dec. 2016, pp. 1–6.
[154] A. A. Khuwaja, Y. Chen, N. Zhao, M.-S. Alouini, and P. Dobbins, "A survey of channel modeling for UAV communications," *IEEE Commun. Surveys Tuts.*, vol. 20, no. 4, pp. 2804–2821, 4th Quart., 2018.
[155] R. Janaswamy, "An indoor pathloss model at 60 GHz based on transport theory," *IEEE Antennas Wireless Propag. Lett.*, vol. 5, pp. 58–60, 2006.
[156] Y. Lostanlen, Y. Corre, Y. Louet, Y. Le Helloco, S. Collonge, and G. El-Zein, "Comparison of measurements and simulations in indoor environments for wireless local networks at 60 GHz," in *Proc. IEEE 55th Veh. Technol. Conf. (VTC Spring)*, May 2002, pp. 389–393.
[157] J. Hansen, "A novel stochastic millimeter-wave indoor radio channel model," *IEEE J. Sel. Areas Commun.*, vol. 20, no. 6, pp. 1240–1246, Aug. 2002.
[158] P. F. M. Smulders and L. M. Correia, "Characterisation of propagation in 60 GHz radio channels," *Electron. Commun. Eng. J.*, vol. 9, no. 2, pp. 73–80, Apr. 1997.
[159] N. Moraitis and P. Constantinou, "Indoor channel modeling at 60 GHz for wireless LAN applications," in *Proc. 13th IEEE Int. Symp. Pers., Indoor Mobile Radio Commun.*, vol. 3, Sep. 2014, pp. 1203–1207.
[160] S. Jaeckel, L. Raschkowski, K. Borner, and L. Thiele, "QuaDRiGa: A 3-D multi-cell channel model with time evolution for enabling virtual field trials," *IEEE Trans. Antennas Propag.*, vol. 62, no. 6, pp. 3242–3256, Jun. 2014.
[161] T. Jamsa, Deliverable D1.4 METIS Channel Models, document ICT-317669-METIS/D1.4, METIS, New York, NY, USA, Feb. 2015. [Online]. Available: https://www.metis2020.com/wpcontent/uploads/METIS_D1.4_v3.pdf
[162] *Study on Channel Model for Frequencies From 0.5 to 100 GHz*, document TR 38.901 V14.1.1 Release, 3GPP, Aug. 2017, vol. 14. [Online]. Available: http://www.3gpp.org/DynaReport/38901.htm
[163] P. Almers, E. Bonek, A. Burr, N. Czink, M. Debbah, V. Degli-Esposti, H. Hofstetter, P. Kyösti, D. Laurenson, G. Matz, A. F. Molisch, C. Oestges, and H. Özcelik, "Survey of channel and radio propagation models for wireless MIMO systems," *EURASIP J. Wireless Commun. Netw.*, vol. 2007, no. 1, Dec. 2007, Art. no. 019070.
[164] R. G. Kouyoumjian and P. H. Pathak, "A uniform geometrical theory of diffraction for an edge in a perfectly conducting surface," *Proc. IEEE*, vol. 62, no. 11, pp. 1448–1461, Nov. 1974.
[165] P. Pathak, N. Wang, W. Burnside, and R. Kouyoumjian, "A uniform GTD solution for the radiation from sources on a convex surface," *IEEE Trans. Antennas Propag.*, vol. AP-29, no. 4, pp. 609–622, Jul. 1981.
[166] P. Pathak, W. Burnside, and R. Marhefka, "A uniform GTD analysis of the diffraction of electromagnetic waves by a smooth convex surface," *IEEE Trans. Antennas Propag.*, vol. 28, no. 5, pp. 631–642, Sep. 1980.
[167] S. Hur, S. Baek, B. Kim, J. Park, A. F. Molisch, K. Haneda, and M. Peter, "28 GHz channel modeling using 3D ray-tracing in urban environments," in *Proc. 9th Eur. Conf. Antennas Propag. (EuCAP)*, Apr. 2015, pp. 1–5.
[168] Ł. Januszkiewicz, "Model for ray-based UTD simulations of the human body shadowing effect in 5G wireless systems," *Int. J. Antennas Propag.*, vol. 2018, pp. 1–11, Jul. 2018.
[169] A. Khafaji, R. Saadane, J. El Abbadi, and M. Belkasmi, "Ray tracing technique based 60 GHz band propagation modelling and influence of people shadowing," *Int. J. Electr., Comput., Syst. Eng.*, vol. 2, no. 2, pp. 102–108, 2008.
[170] W. K. M. Peter, W. Keusgen, and R. Felbecker, "Measurement and ray-tracing simulation of the 60 GHz indoor broadband channel: Model accuracy and parameterization," in *Proc. 2nd Eur. Conf. Antennas Propag. (EuCAP)*, 2007, p. 432.
[171] C.-P. Lim, M. Lee, R. J. Burkholder, J. L. Volakis, and R. J. Marhefka, "60 GHz indoor propagation studies for wireless communications based on a ray-tracing method," *EURASIP J. Wireless Commun. Netw.*, vol. 2007, no. 1, p. 49, Dec. 2007.
[172] (2018). *Altair WinProp*. [Online]. Available: https://altairhyperworks.com/product/FEKO/WinProp-Propagation-Modeling
[173] (2018). *Ranplan Professional*. [Online]. Available: https://ranplanwireless.com/
[174] M. R. Akdeniz, Y. Liu, M. K. Samimi, S. Sun, S. Rangan, T. S. Rappaport, and E. Erkip, "Millimeter wave channel modeling and cellular capacity evaluation," *IEEE J. Sel. Areas Commun.*, vol. 32, no. 6, pp. 1164–1179, Jun. 2014.
[175] *Initial Channel Models Based on Measurements*, Standard METIS ICT-317669-METIS/D1.2, 2015. [Online]. Available: https://www.metis2020.com/
[176] X. Cheng, C.-X. Wang, D. Laurenson, S. Salous, and A. Vasilakos, "An adaptive geometry-based stochastic model for non-isotropic MIMO mobile-to-mobile channels," *IEEE Trans. Wireless Commun.*, vol. 8, no. 9, pp. 4824–4835, Sep. 2009.
[177] X. Cheng, Q. Yao, M. Wen, C.-X. Wang, L.-Y. Song, and B.-L. Jiao, "Wideband channel modeling and intercarrier interference cancellation for Vehicle-to-Vehicle communication systems," *IEEE J. Sel. Areas Commun.*, vol. 31, no. 9, pp. 434–448, Sep. 2013.
[178] A. Ghazal, C.-X. Wang, B. Ai, D. Yuan, and H. Haas, "A nonstationary wideband MIMO channel model for high-mobility intelligent transportation systems," *IEEE Trans. Intell. Transp. Syst.*, vol. 16, no. 2, pp. 885–897, Sep. 2014.
[179] X. Yin, X. Cai, X. Cheng, J. Chen, and M. Tian, "Empirical geometry-based random-cluster model for high-speed-train channels in UMTS networks," *IEEE Trans. Intell. Transp. Syst.*, vol. 16, no. 5, pp. 2850–2861, Oct. 2015.
[180] J. Karedal, F. Tufvesson, N. Czink, A. Paier, C. Dumard, T. Zemen, C. F. Mecklenbrauker, and A. F. Molisch, "A geometry-based stochastic MIMO model for vehicle-to-vehicle communications," *IEEE Trans. Wireless Commun.*, vol. 8, no. 7, pp. 3646–3657, Jul. 2009.
[181] S. Geng, J. Kivinen, X. Zhao, and P. Vainikainen, "Millimeter-wave propagation channel characterization for short-range wireless communications," *IEEE Trans. Veh. Technol.*, vol. 58, no. 1, pp. 3–13, Jan. 2009.
[182] C.-C. Chong, C.-M. Tan, D. I. Laurenson, S. McLaughlin, M. A. Beach, and A. R. Nix, "A new statistical wideband spatio-temporal channel model for 5-GHz band WLAN systems," *IEEE J. Sel. Areas Commun.*, vol. 21, no. 2, pp. 139–150, Feb. 2003.
[183] J. W. Wallace and M. A. Jensen, "Modeling the indoor MIMO wireless channel," *IEEE Trans. Antennas Propag.*, vol. 50, no. 5, pp. 591–599, May 2002.
[184] A. A. M. Saleh and R. Valenzuela, "A statistical model for indoor multipath propagation," *IEEE J. Sel. Areas Commun.*, vol. 5, no. 2, pp. 128–137, Feb. 1987.
[185] T. Zwick, C. Fischer, and W. Wiesbeck, "A stochastic multipath channel model including path directions for indoor environments," *IEEE J. Sel. Areas Commun.*, vol. 20, no. 6, pp. 1178–1192, Aug. 2002.
[186] J. P. Kermoal, L. Schumacher, K. I. Pedersen, P. E. Mogensen, and F. Frederiksen, "A stochastic MIMO radio channel model with experimental validation," *IEEE J. Sel. Areas Commun.*, vol. 20, no. 6, pp. 1211–1226, Aug. 2002.
[187] D.-S. Shiu, G. J. Foschini, M. J. Gans, and J. M. Kahn, "Fading correlation and its effect on the capacity of multielement antenna systems," *IEEE Trans. Commun.*, vol. 48, no. 3, pp. 502–513, Mar. 2000.
[188] D. P. McNamara, "Temporal variation of multiple-input multiple-output (MIMO) channels in indoor environments," in *Proc. 11th Int. Conf. Antennas Propag. (ICAP)*, Leuven, Belgium, Oct. 2000, pp. 139–143.
[189] C.-N. Chuah, J. M. Kahn, and D. Tse, "Capacity of multi-antenna array systems in indoor wireless environment," in *Proc. IEEE GLOBECOM*, New York, NY, USA, Nov. 1998, pp. 1894–1899.
[190] D. Chizhik, F. Rashid-Farrokhi, J. Ling, and A. Lozano, "Effect of antenna separation on the capacity of BLAST in correlated channels," *IEEE Commun. Lett.*, vol. 4, no. 11, pp. 337–339, Nov. 2000.
[191] A. M. Sayeed, "Deconstructing multiantenna fading channels," *IEEE Trans. Signal Process.*, vol. 50, no. 10, pp. 2563–2579, Oct. 2002.
[192] M. Debbah and R. R. Muller, "MIMO channel modeling and the principle of maximum entropy," *IEEE Trans. Inf. Theory*, vol. 51, no. 5, pp. 1667–1690, May 2005.
[193] A. G. Burr, "Capacity bounds and estimates for the finite scatterers MIMO wireless channel," *IEEE J. Sel. Areas Commun.*, vol. 21, no. 5, pp. 812–818, Jun. 2003.
[194] S. Wu, C.-X. Wang, H. Haas, E.-H.-M. Aggoune, M. M. Alwakeel, and B. Ai, "A non-stationary wideband channel model for massive MIMO communication systems," *IEEE Trans. Wireless Commun.*, vol. 14, no. 3, pp. 1434–1446, Mar. 2015.
[195] Y. Chen, Y. Li, S. Sun, X. Cheng, and X. Chen, "A twin-multi-ring channel model for massive MIMO system," in *Proc. 16th Int. Symp. Commun. Inf. Technol. (ISCIT)*, Qingdao, China, Sep. 2016, pp. 606–610.

[196] H. Wu, S. Jin, and X. Gao, "Non-stationary multi-ring channel model for massive MIMO systems," in *Proc. Int. Conf. Wireless Commun. Signal Process. (WCSP)*, Oct. 2015, pp. 1–6.

[197] S. Wu, C.-X. Wang, E.-H.-M. Aggoune, M. M. Alwakeel, and Y. He, "A non-stationary 3-D wideband twin-cluster model for 5G massive MIMO channels," *IEEE J. Sel. Areas Commun.*, vol. 32, no. 6, pp. 1207–1218, Jun. 2014.

[198] *Spatial Channel Model for Multiple Input Multiple Output (MIMO) Simulations*, document TR (2003-09), Release 6, 3GPP, 2017.

[199] D. S. Baum, J. Hansen, J. Salo, G. D. Galdo, M. Milojevic, and P. Kyösti, "An interim channel model for beyond-3G systems: Extending the 3GPP spatial channel model (SCM)," in *Proc. IEEE 61st Veh. Technol. Conf.*, vol. 5, May 2005, pp. 3132–3136.

[200] L. M. Correia, "Wireless flexible personalised communications: COST 259," in *Proc. Eur. Co-Operation Mobile Radio Res.* New York, NY, USA: Wiley, 2001, pp. 77–222.

[201] D. S. Baum, H. El-Sallabi, T. Jamsa, J. Meinila, P. Kyösti, and X. Zhao, "Final report on link level and system level channel models," Winner Deliverable D5, 2005.

[202] J. Meinilä, P. Kyösti, T. Jämsä, and L. Hentilä, "WINNER II channel models," in *Radio Technologies and Concepts for IMT-Advanced*. Hoboken, NJ, USA: Wiley, 2010, pp. 39–92.

[203] T. Jamsa and J. Iinatti, "Approximation of geometry based stochastic channel models," in *Proc. 1st Int. Conf. Wireless Commun., Veh. Technol., Inf. Theory Aerosp. Electron. Syst. Technol.*, May 2009, pp. 693–697.

[204] C. F. Lopez, C.-X. Wang, and R. Feng, "A novel 2D non-stationary wideband massive MIMO channel model," in *Proc. IEEE 21st Int. Workshop Comput. Aided Model. Design Commun. Links Netw. (CAMAD)*, Oct. 2016, pp. 207–212.

[205] C. F. Lopez and C.-X. Wang, "Novel 3-D non-stationary wideband models for massive MIMO channels," *IEEE Trans. Wireless Commun.*, vol. 17, no. 5, pp. 2893–2905, May 2018.

[206] C. A. Gutierrez and M. Patzold, "The Riemann sum method for the design of sum-of-cisoids simulators for Rayleigh fading channels in non-isotropic scattering environments," in *Proc. Int. Conf. Ultra Modern Telecommun. Workshops*, Oct. 2009, pp. 1–5.

[207] A. O. Martinez, P. Eggers, and E. De Carvalho, "Geometry-based stochastic channel models for 5G: Extending key features for massive MIMO," in *Proc. IEEE 27th Annu. Int. Symp. Pers., Indoor, Mobile Radio Commun. (PIMRC)*, Sep. 2016, pp. 1–6.

[208] Y. Xie, B. Li, X. Zuo, M. Yang, and Z. Yan, "A 3D geometry-based stochastic model for 5G massive MIMO channels," in *Proc. 11th EAI Int. Conf. Heterogeneous Netw. Qual., Rel., Secur. Robustness*, 2015, pp. 216–222.

[209] J. Chen, X. Yin, X. Cai, and S. Wang, "Measurement-based massive MIMO channel modeling for outdoor LoS and NLoS environments," *IEEE Access*, vol. 5, pp. 2126–2140, 2017.

[210] A. Kammoun, H. Khanfir, Z. Altman, M. Debbah, and M. Kamoun, "Preliminary results on 3D channel modeling: From theory to standardization," 2013, *arXiv:1312.0288*. [Online]. Available: https://arxiv.org/abs/1312.0288

[211] X. Gao, F. Tufvesson, and O. Edfors, "Massive MIMO channels—Measurements and models," in *Proc. Asilomar Conf. Signals, Syst. Comput.*, Nov. 2013, pp. 280–284.

[212] X. Gao, J. Flordelis, G. Dahman, F. Tufvesson, O. Edfors, and O. ctober. 2., "Massive MIMO channel modeling—Extension of the COST 2100 model," in *Proc. Joint NEWCOM/COST Workshop Wireless Commun. (JNCW)*, vol. 1, pp. 4558–4563.

[213] L. Liu, C. Oestges, J. Poutanen, K. Haneda, P. Vainikainen, F. Quitin, F. Tufvesson, and P. Doncker, "The COST 2100 MIMO channel model," *IEEE Wireless Commun.*, vol. 19, no. 6, pp. 92–99, Dec. 2012.

[214] J. Joung, E. Kurniawan, and S. Sun, "Channel correlation modeling and its application to massive MIMO channel feedback reduction," *IEEE Trans. Veh. Technol.*, vol. 66, no. 5, pp. 3787–3797, May 2017.

[215] S. Dahiya, "A statistical block fading channel model for multiuser massive MIMO system," in *Proc. SPCOM*, Bengaluru, India, Jun. 2016, pp. 1–5.

[216] S. Wu, C.-X. Wang, E.-H.-M. Aggoune, and M. M. Alwakeel, "A novel Kronecker-based stochastic model for massive MIMO channels," in *Proc. IEEE/CIC Int. Conf. Commun. China (ICCC)*, Nov. 2015, pp. 1–6.

[217] G. Taricco, "Asymptotic mutual information statistics of separately correlated Rician fading MIMO channels," *IEEE Trans. Inf. Theory*, vol. 54, no. 8, pp. 3490–3504, Aug. 2008.

[218] Y. Yu, P.-F. Cui, J. She, Y. Liu, X. Yang, W.-J. Lu, S. Jin, and H.-B. Zhu, "Measurement and empirical modeling of massive MIMO channel matrix in real indoor environment," in *Proc. 8th Int. Conf. Wireless Commun. Signal Process. (WCSP)*, Oct. 2016, pp. 1–5.

[219] M. Mbeutcha, W. Fan, J. Hejsclbaek, and G. F. Pedersen, "Evaluation of massive MIMO systems using time-reversal beamforming technique," in *Proc. IEEE 27th Annu. Int. Symp. Pers., Indoor, Mobile Radio Commun. (PIMRC)*, Sep. 2016, pp. 1–6.

[220] N. R. Leonor, R. F. S. Caldeirinha, T. R. Fernandes, D. Ferreira, and M. García Sánchez, "A 2D ray-tracing based model for Micro- and millimeter-wave propagation through vegetation," *IEEE Trans. Antennas Propag.*, vol. 62, no. 12, pp. 6443–6453, Dec. 2014.

[221] B. Goktepe, M. Peter, R. J. Weiler, and W. Keusgen, "The influence of street furniture and tree trunks in urban scenarios on ray tracing simulations in the millimeter wave band," in *Proc. Eur. Microw. Conf. (EuMC)*, Sep. 2015, pp. 195–198.

[222] J.-Y. Lee, J.-H. Lee, and S.-C. Kim, "Improving the accuracy of millimeter-wave ray-tracing simulations by modeling roadside trees," *IEEE Antennas Wireless Propag. Lett.*, vol. 18, no. 1, pp. 162–166, Jan. 2019.

[223] A. M. Al-samman, T. Abd Rahman, and M. H. Azmi, "Indoor corridor wideband radio propagation measurements and channel models for 5G millimeter wave wireless communications at 19 GHz, 28 GHz, and 38 GHz bands," *Wireless Commun. Mobile Comput.*, 2018, pp. 1–12, 2018.

[224] Z. D. Zhong, B. Ai, G. Zhu, H. Wu, L. Xiong, F. G. Wang, L. Lei, J. W. Ding, K. Guan, and R. S. He, *Dedicated Mobile Communications for High-Speed Railway*. Berlin, Germany: Springer, 2018.

[225] M. K. Samimi and T. S. Rappaport, "3-D millimeter-wave statistical channel model for 5G wireless system design," *IEEE Trans. Microw. Theory Techn.*, vol. 64, no. 7, pp. 2207–2225, Jul. 2016.

[226] M. K. Samimi, S. Sun, and T. S. Rappaport, "MIMO channel modeling and capacity analysis for 5G millimeter-wave wireless systems," in *Proc. 10th Eur. Conf. Antennas Propag. (EuCAP)*, Apr. 2016, pp. 1–5.

[227] M. K. Samimi and T. S. Rappaport, "Ultra-wideband statistical channel model for non line of sight millimeter-wave urban channels," in *Proc. IEEE Global Commun. Conf.*, Dec. 2014, pp. 3483–3489.

[228] M. K. Samimi, G. R. MacCartney, S. Sun, and T.S. Rappaport, "28 GHz millimeter-wave ultrawideband small-scale fading models in wireless channels," in *Proc. IEEE 83rd Veh. Technol. Conf. (VTC Spring)*, May 2016, pp. 1–6.

[229] M. Samimi, K. Wang, Y. Azar, G. N. Wong, R. Mayzus, H. Zhao, J. K. Schulz, S. Sun, F. Gutierrez, and T. S. Rappaport, "28 GHz angle of arrival and angle of departure analysis for outdoor cellular communications using steerable beam antennas in New York City," in *Proc. IEEE 77th Veh. Technol. Conf. (VTC Spring)*, Jun. 2013, pp. 1–6.

[230] M. K. Samimi and T. S. Rappaport, "3-D statistical channel model for millimeter-wave outdoor mobile broadband communications," in *Proc. IEEE Int. Conf. Commun. (ICC)*, London, U.K., Jun. 2015, pp. 2430–2436.

[231] M. K. Samimi and T. S. Rappaport, "Statistical channel model with multi-frequency and arbitrary antenna beamwidth for millimeter-wave outdoor communications," in *Proc. IEEE Globecom Workshops (GC Wkshps)*, Dec. 2015, pp. 1–7.

[232] M. K. Samimi and T. S. Rappaport, "Local multipath model parameters for generating 5G millimeter-wave 3GPP-like channel impulse response," in *Proc. 10th Eur. Conf. Antennas Propag. (EuCAP)*, Apr. 2016, pp. 1–5.

[233] J. Meredith, *Study on Channel Model for Frequency Spectrum Above 6 GHz*, document 3GPP TR 38.900, 2016.

[234] S. Hur, S. Baek, B. Kim, Y. Chang, A. F. Molisch, T. S. Rappaport, K. Haneda, and J. Park, "Proposal on millimeter-wave channel modeling for 5G cellular system," *IEEE J. Sel. Topics Signal Process.*, vol. 10, no. 3, pp. 454–469, Apr. 2016.

[235] X. Zhao, S. Li, Q. Wang, M. Wang, S. Sun, and W. Hong, "Channel measurements, modeling, simulation and validation at 32 GHz in outdoor microcells for 5G radio systems," *IEEE Access*, vol. 5, pp. 1062–1072, 2017.

[236] A. A. M. Saleh and R. Valenzuela, "A statistical model for indoor multipath propagation," *IEEE J. Sel. Areas Commun.*, vol. 5, no. 2, pp. 128–137, Feb. 1987.

[237] R. Adeogun, "Calibration of stochastic radio propagation models using machine learning," *IEEE Antennas Wireless Propag. Lett.*, vol. 18, no. 12, pp. 2538–2542, Dec. 2019.

[238] Y. Shoji, H. Sawada, C.-S. Choi, and H. Ogawa, "A modified SV-model suitable for Line-of-Sight desktop usage of millimeter-wave WPAN systems," *IEEE Trans. Antennas Propag.*, vol. 57, no. 10, pp. 2940–2948, Oct. 2009.

[239] S. K. Yong, "TG3c channel modeling subcommitee final report," IEEE P802 Work. Group Wireless Pers. Area Netw. (WPANs), Tech. Rep. 15-07-0584-01-003c, 2007. [Online]. Available: https://mentor.ieee.org/802.15/dcn/07/15-07-0584-01-003ctg3c-channel-modeling-sub-committee-final-report.doc

[240] Q. H. Spencer, B. D. Jeffs, M. A. Jensen, and A. L. Swindlehurst, "Modeling the statistical time and angle of arrival characteristics of an indoor multipath channel," *IEEE J. Sel. Areas Commun.*, vol. 18, no. 3, pp. 347–360, Mar. 2000.

[241] C. Liu, E. Skafidas, T. S. Pollock, and R. J. Evans, "Angle of arrival extended S-V model for the 60 ghz wireless desktop channel," in *Proc. IEEE 17th Int. Symp. Pers., Indoor Mobile Radio Commun.*, Sep. 2006, pp. 1–6.

[242] K. Yu and B. Ottersten, "Models for MIMO propagation channels: A review," *Wireless Commun. Mobile Comput.*, vol. 2, no. 7, pp. 653–666, Nov. 2002.

[243] C. Gustafson, K. Haneda, S. Wyne, and F. Tufvesson, "On mm-Wave multipath clustering and channel modeling," *IEEE Trans. Antennas Propag.*, vol. 62, no. 3, pp. 1445–1455, Mar. 2014.

[244] A. F. Molisch, H. Asplund, R. Heddergott, M. Steinbauer, and T. Zwick, "The COST259 directional channel model-part I: Overview and methodology," *IEEE Trans. Wireless Commun.*, vol. 5, no. 12, pp. 3421–3433, Dec. 2006.

[245] N. Czink and C. Oestges, "The COST 273 MIMO channel model: Three kinds of clusters," in *Proc. IEEE 10th Int. Symp. Spread Spectr. Techn. Appl.*, Aug. 2008, pp. 282–286.

[246] *Channel Modeling and Characterization, Deliverable 5.1*, document FP7-ICT-608637, MiWEBA, Jun. 2014.

[247] R. J. Weiler, M. Peter, W. Keusgen, A. Maltsev, I. Karls, A. Pudeyev, I. Bolotin, I. Siaud, and A.-M. Ulmer-Moll, "Quasi-deterministic millimeter-wave channel models in MiWEBA," *EURASIP J. Wireless Commun. Netw.*, vol. 2016, no. 1, p. 84, Dec. 2016.

[248] S. Jaeckel, K. Borner, L. Thiele, and V. Jungnickel, "A geometric polarization rotation model for the 3-D spatial channel model," *IEEE Trans. Antennas Propag.*, vol. 60, no. 12, pp. 5966–5977, Dec. 2012.

[249] *Technical Specification Group Radio Access Network, Study on 3D Channel Model for LTE (Release 12), V12.0.0*, document TR 36.873, 3GPP, Sophia Antipolis, France, 3rd Generation Partnership Project, Jun. 2015.

[250] mmMAGIC Deliverable D2.1. (Mar. 2016). *Measurement Campaigns and Initial Channel Models for Preferred Suitable Frequency Ranges*. [Online]. Available: https://5g-mmmagic.eu/results/#deliverables

[251] X. Yin, N. Zhang, W. Stephen, and X. Cheng, "Measurement-based spatial-consistent channel modeling involving clusters of scatterers," *ZTE Commun.*, vol. 15, no. 1, p. 1, 2017.

[252] 5GCM. (Oct. 2016). *5G Channel Model for Bands up to 100 GHz*. [Online]. Available: http://www.5gworkshops.com/5GCM.html

[253] M. K. Samimi, T. S. Rappaport, and G. R. MacCartney, "Probabilistic omnidirectional path loss models for millimeter-wave outdoor communications," *IEEE Wireless Commun. Lett.*, vol. 4, no. 4, pp. 357–360, Aug. 2015.

[254] S. Wu, C.-X. Wang, E.-H.-M. Aggoune, M. M. Alwakeel, and X. You, "A general 3-D non-stationary 5G wireless channel model," *IEEE Trans. Commun.*, vol. 66, no. 7, pp. 3065–3078, Jul. 2018.

[255] A. Maltsev, A. Pudeyev, A. Lomayev, and I. Bolotin, *Channel Models for IEEE 802.11ay*, document 802.11-15/1150r9, New York, NY, USA, 2016.

[256] Maltsev, Alexander, Andrey Pudeyev, Artem Lomayev, and Ilya Bolotin, "Channel modeling in the next generation mmWave Wi-Fi: IEEE 802.11 ay standard," in *Proc. Eur. Wireless 22th Eur. Wireless Conf.*, 2016, pp. 1–8.

[257] *Guidelines for Evaluation of Radio Interface Technologies for IMT-2020*, document ITU-R M.2412-0, IMT-2020, 2017. [Online]. Available: https://www.itu.int/dms_pub/itu-r/opb/rep/R-REP-M.2412-2017-PDF-E.pdf

[258] A. Osseiran, J. F. Monserrat, and P. Marsch, Eds., *5G Mobile and Wireless Communications Technology*. Cambridge, U.K.: Cambridge Univ. Press, 2016.

[259] V. Kristem, S. Sangodoyin, C. U. Bas, M. Kaske, J. Lee, C. Schneider, G. Sommerkorn, C. J. Zhang, R. S. Thoma, and A. F. Molisch, "3D MIMO Outdoor-to-Indoor propagation channel measurement," *IEEE Trans. Wireless Commun.*, vol. 16, no. 7, pp. 4600–4613, Jul. 2017.

[260] C.-X. Wang, S. Wu, L. Bai, X. You, J. Wang, and C.-L. I, "Recent advances and future challenges for massive MIMO channel measurements and models," *Sci. China Inf. Sci.*, vol. 59, no. 2, pp. 1–16, Feb. 2016.

[261] B. Wang, L. Dai, Z. Wang, N. Ge, and S. Zhou, "Spectrum and energy-efficient beamspace MIMO-NOMA for millimeter-wave communications using lens antenna array," *IEEE J. Sel. Areas Commun.*, vol. 35, no. 10, pp. 2370–2382, Oct. 2017.

[262] L. Zhu, J. Zhang, Z. Xiao, X. Cao, D. O. Wu, and X.-G. Xia, "Millimeter-wave NOMA with user grouping, power allocation and hybrid beamforming," *IEEE Trans. Wireless Commun.*, vol. 18, no. 11, pp. 5065–5079, Nov. 2019.

[263] N. M. Balasubramanya, A. Gupta, and M. Sellathurai, "Combining code-domain and power-domain NOMA for supporting higher number of users," in *Proc. IEEE Global Commun. Conf. (GLOBECOM)*, Dec. 2018, pp. 1–6.

[264] J. Cui, Y. Liu, Z. Ding, P. Fan, and A. Nallanathan, "Optimal user scheduling and power allocation for millimeter wave NOMA systems," *IEEE Trans. Wireless Commun.*, vol. 17, no. 3, pp. 1502–1517, Mar. 2018.

[265] M. A. Almasi and H. Mehrpouyan, "Non-orthogonal multiple access based on hybrid beamforming for mmWave systems," in *Proc. IEEE 88th Veh. Technol. Conf. (VTC-Fall)*, Aug. 2018, pp. 1–7.

[266] D. Zhang, Z. Zhou, C. Xu, Y. Zhang, J. Rodriguez, and T. Sato, "Capacity analysis of NOMA with mmWave massive MIMO systems," *IEEE J. Sel. Areas Commun.*, vol. 35, no. 7, pp. 1606–1618, Jul. 2017.

[267] S. Rey, *Progress in Regulation Above 275 GHz*, IEEE Standard 802.15-14-439-00-0thz, Jul. 2016. [Online]. Available: https://mentor.ieee.org/802.15/dcn/16/15-16-0492-00-0thz-progressin-regulation-above-275-ghz.pdf

[268] T. S. Rappaport, E. Ben-Dor, J. N. Murdock, and Y. Qiao, "38 GHz and 60 GHz angle-dependent propagation for cellular & peer-to-peer wireless communications," in *Proc. IEEE Int. Conf. Commun. (ICC)*, Jun. 2012, pp. 4568–4573.

[269] S. Sun, T. A. Thomas, T. S. Rappaport, H. Nguyen, I. Z. Kovacs, and I. Rodriguez, "Path loss, shadow fading, and Line-of-Sight probability models for 5G urban macro-cellular scenarios," in *Proc. IEEE Globecom Workshops (GC Wkshps)*, Dec. 2015, pp. 1–7.

[270] S. Han, C.-L. I, Z. Xu, and C. Rowell, "Large-scale antenna systems with hybrid analog and digital beamforming for millimeter wave 5G," *IEEE Commun. Mag.*, vol. 53, no. 1, pp. 186–194, Jan. 2015.

[271] J. Mo and R. W. Heath, Jr., "Capacity analysis of one-bit quantized MIMO systems with transmitter channel state information," *IEEE Trans. Signal Process.*, vol. 63, no. 20, pp. 5498–5512, Oct. 2015.

[272] R. Mendez-Rial, C. Rusu, N. Gonzalez-Prelcic, A. Alkhateeb, and R. W. Heath, Jr., "Hybrid MIMO architectures for millimeter wave communications: Phase shifters or switches?" *IEEE Access*, vol. 4, pp. 247–267, Jan. 2016.

[273] X. Gao, L. Dai, S. Han, C.-L. I, and R. W. Heath, Jr., "Energy-efficient hybrid analog and digital precoding for mmWave MIMO systems with large antenna arrays," *IEEE J. Sel. Areas Commun.*, vol. 34, no. 4, pp. 998–1009, Apr. 2016.

[274] X. Sun and C. Qi, "Multiuser beam allocation for millimeter wave massive MIMO systems," in *Proc. IEEE Int. Conf. Commun. (ICC)*, May 2019, pp. 1–7.

[275] G. R. Muns, K. V. Mishra, C. B. Guerra, Y. C. Eldar, and K. R. Chowdhury, "Beam alignment and tracking for autonomous vehicular communication using IEEE 802.11ad-based radar," in *Proc. IEEE Conf. Comput. Commun. Workshops (INFOCOM WKSHPS)*, Apr. 2019, pp. 535–540.

[276] L. Zhou and Y. Ohashi, "Efficient codebook-based MIMO beamforming for millimeter-wave WLANs," in *Proc. IEEE 23rd Int. Symp. Pers., Indoor Mobile Radio Commun. (PIMRC)*, Sep. 2012, pp. 1885–1889.

[277] L. Zhao, D. W. K. Ng, and J. Yuan, "Multi-user precoding and channel estimation for hybrid millimeter wave systems," *IEEE J. Sel. Areas Commun.*, vol. 35, no. 7, pp. 1576–1590, Jul. 2017.

[278] A. F. Molisch, V. V. Ratnam, S. Han, Z. Li, S. L. H. Nguyen, L. Li, and K. Haneda, "Hybrid beamforming for massive MIMO: A survey," *IEEE Commun. Mag.*, vol. 55, no. 9, pp. 134–141, 2017.

[279] S. Kutty and D. Sen, "Beamforming for millimeter wave communications: An inclusive survey," *IEEE Commun. Surveys Tuts.*, vol. 18, no. 2, pp. 949–973, 2nd Quart., 2016.

[280] D. J. Love, R. W. Heath, Jr., and T. Strohmer, "Grassmannian beamforming for multiple-input multiple-output wireless systems," *IEEE Trans. Inf. Theory*, vol. 49, no. 10, pp. 2735–2747, Oct. 2003.

[281] J. Wang, Z. Lan, C.-w. Pyo, T. Baykas, C.-s. Sum, M. A. Rahman, J. Gao, R. Funada, F. Kojima, H. Harada, and S. Kato, "Beam codebook based beamforming protocol for multi-Gbps millimeter-wave WPAN systems," *IEEE J. Sel. Areas Commun.*, vol. 27, no. 8, pp. 1390–1399, Oct. 2009.

[282] A. N. Uwaechia and N. M. Mahyuddin, "Collaborative framework of algorithms for sparse channel estimation in OFDM systems," *J. Commun. Netw.*, vol. 20, no. 1, pp. 9–19, Feb. 2018.

[283] A. N. Uwaechia and N. M. Mahyuddin, "Stage-determined matching pursuit for sparse channel estimation in OFDM systems," *IEEE Syst. J.*, vol. 13, no. 3, pp. 2240–2251, Sep. 2019.

[284] M. N. Kulkarni, A. Ghosh, and J. G. Andrews, "A comparison of MIMO techniques in downlink millimeter wave cellular networks with hybrid beamforming," *IEEE Trans. Commun.*, vol. 64, no. 5, pp. 1952–1967, May 2016.

[285] J. Zhang, L. Dai, Z. He, B. Ai, and O. A. Dobre, "Mixed-ADC/DAC multipair massive MIMO relaying systems: Performance analysis and power optimization," *IEEE Trans. Commun.*, vol. 67, no. 1, pp. 140–153, Jan. 2019.

[286] Z. Wang, M. Li, Q. Liu, and A. L. Swindlehurst, "Hybrid precoder and combiner design with low-resolution phase shifters in mmWave MIMO systems," *IEEE J. Sel. Topics Signal Process.*, vol. 12, no. 2, pp. 256–269, May 2018.

[287] J. Liu, Z. Luo, and X. Xiong, "Low-resolution ADCs for wireless communication: A comprehensive survey," *IEEE Access*, vol. 7, pp. 91291–91324, 2019.

[288] T. Xie, L. Dai, D. W. K. Ng, and C.-B. Chae, "On the power leakage problem in millimeter-wave massive MIMO with lens antenna arrays," *IEEE Trans. Signal Process.*, vol. 67, no. 18, pp. 4730–4744, Sep. 2019.

[289] Y. Zeng and R. Zhang, "Millimeter wave MIMO with lens antenna array: A new path division multiplexing paradigm," *IEEE Trans. Commun.*, vol. 64, no. 4, pp. 1557–1571, Feb. 2016.

[290] L. Frenzel, "Fundamentals of Communications Access Technologies: FDMA, TDMA, CDMA, OFDMA, AND SDMA," Electronic Design, 2013.

[291] K. Kinoshita, M. Hata, and K. Hirade, "Digital mobile telephone system using TD/FDMA scheme," *IEEE Trans. Veh. Technol.*, vol. VT-31, no. 4, pp. 153–157, Nov. 1982.

[292] S. Hara and R. Prasad, "Overview of multicarrier CDMA," *IEEE Commun. Mag.*, vol. 35, no. 12, pp. 126–133, Dec. 1997.

[293] Y. Han, H. Zhang, S. Jin, X. Li, R. Yu, and Y. Zhang, "Investigation of transmission schemes for millimeter-wave massive MU-MIMO systems," *IEEE Syst. J.*, vol. 11, no. 1, pp. 72–83, Mar. 2017.

[294] J. Liu, M. Sheng, and J. Li, "Limitation of SDMA in ultra-dense small cell networks," *IEEE Wireless Commun. Lett.*, vol. 7, no. 4, pp. 506–509, Aug. 2018.

[295] Y. Han, S. Jin, X. Li, and Y. Huang, "A joint SDMA and interference suppression multiuser transmission scheme for millimeter-wave massive MIMO systems," in *Proc. 6th Int. Conf. Wireless Commun. Signal Process. (WCSP)*, Oct. 2014, pp. 1–5.

[296] W. Hao, M. Zeng, Z. Chu, and S. Yang, "Energy-efficient power allocation in millimeter wave massive MIMO with non-orthogonal multiple access," *IEEE Wireless Commun. Lett.*, vol. 6, no. 6, pp. 782–785, Dec. 2017.

[297] Z. Xiao, L. Zhu, J. Choi, P. Xia, and X.-G. Xia, "Joint power allocation and beamforming for non-orthogonal multiple access (NOMA) in 5G millimeter wave communications," *IEEE Trans. Wireless Commun.*, vol. 17, no. 5, pp. 2961–2974, May 2018.

[298] L. Zhu, Z. Xiao, X.-G. Xia, and D. Oliver Wu, "Millimeter-wave communications with non-orthogonal multiple access for B5G/6G," *IEEE Access*, vol. 7, pp. 116123–116132, 2019.

[299] C. Jeong, J. Park, and H. Yu, "Random access in millimeter-wave beamforming cellular networks: Issues and approaches," *IEEE Commun. Mag.*, vol. 53, no. 1, pp. 180–185, Jan. 2015.

[300] C. N. Barati, S. A. Hosseini, M. Mezzavilla, P. Amiri-Eliasi, S. Rangan, T. Korakis, S. S. Panwar, and M. Zorzi, "Directional initial access for millimeter wave cellular systems," in *Proc. 49th Asilomar Conf. Signals, Syst. Comput.*, Nov. 2015, pp. 307–311.

[301] W. B. Abbas and M. Zorzi, "Context information based initial cell search for millimeter wave 5G cellular networks," in *Proc. Eur. Conf. Netw. Commun. (EuCNC)*, Jun. 2016, pp. 111–116.

[302] A. N. Uwaechia, N. M. Mahyuddin, M. F. Ain, N. M. A. Latiff, and N. F. Za'bah, "Compressed channel estimation for massive MIMO-OFDM systems over doubly selective channels," *Phys. Commun.*, vol. 36, Oct. 2019, Art. no. 100771.

[303] Q. Qin, L. Gui, P. Cheng, and B. Gong, "Time-varying channel estimation for millimeter wave multiuser MIMO systems," *IEEE Trans. Veh. Technol.*, vol. 67, no. 10, pp. 9435–9448, Oct. 2018.

[304] P. R. B. Gomes, A. L. F. de Almeida, J. P. C. L. da Costa, and R. T. de Sousa, "Joint DL and UL channel estimation for millimeter wave MIMO systems using tensor modeling," *Wireless Commun. Mobile Comput.*, vol. 2019, pp. 1–13, Sep. 2019.

[305] J. P. Thomas, M. A. Qidwai, and J. C. Kellogg, "Energy scavenging for small-scale unmanned systems," *J. Power Source*, vol. 159, no. 2, pp. 1494–1509, Sep. 2006.

[306] J. A. G. Akkermans, M. C. van Beurden, G. J. N. Doodeman, and H. J. Visser, "Analytical models for low-power rectenna design," *IEEE Antennas Wireless Propag. Lett.*, vol. 4, pp. 187–190, 2005.

[307] W. Hao, G. Sun, Z. Chu, P. Xiao, Z. Zhu, S. Yang, and R. Tafazolli, "Beamforming design in SWIPT-based joint multicast-unicast mmWave massive MIMO with lens-antenna array," *IEEE Wireless Commun. Lett.*, vol. 8, no. 4, pp. 1124–1128, Aug. 2019.

[308] A. Li and C. Masouros, "Energy-efficient SWIPT: From fully digital to hybrid analog–digital beamforming," *IEEE Trans. Veh. Technol.*, vol. 67, no. 4, pp. 3390–3405, Apr. 2018.

[309] E. Yaacoub, M. Husseini, and H. Ghaziri, "An overview of research topics and challenges for 5G massive MIMO antennas," in *Proc. IEEE Middle East Conf. Antennas Propag. (MECAP)*, Sep. 2016, pp. 1–4.

[310] A. Zhang and X. Lin, "Security-aware and privacy-preserving D2D communications in 5G," *IEEE Netw.*, vol. 31, no. 4, pp. 70–77, Jul. 2017.

[311] A. N. Uwaechia and N. M. Mahyuddin, "Spectrum-efficient distributed compressed sensing based channel estimation for OFDM systems over doubly selective channels," *IEEE Access*, vol. 7, pp. 35072–35088, 2019.

[312] J. Zhang, E. Björnson, M. Matthaiou, D. W. K. Ng, H. Yang, and D. J. Love, "Prospective multiple antenna technologies for beyond 5G," 2019, *arXiv:1910.00092*. [Online]. Available: http://arxiv.org/abs/1910.00092

[313] J. Zhang, S. Chen, Y. Lin, J. Zheng, B. Ai, and L. Hanzo, "Cell-free massive MIMO: A new next-generation paradigm," *IEEE Access*, vol. 7, pp. 99878–99888, 2019.

[314] Y. Jin, J. Zhang, S. Jin, and B. Ai, "Channel estimation for cell-free mmWave massive MIMO through deep learning," *IEEE Trans. Veh. Technol.*, vol. 68, no. 10, pp. 10325–10329, Oct. 2019.

[315] Y. Jin, J. Zhang, B. Ai, and X. Zhang, "Channel estimation for mmWave massive MIMO with convolutional blind denoising network," *IEEE Commun. Lett.*, vol. 24, no. 1, pp. 95–98, Jan. 2020.

[316] G. Interdonato, E. Björnson, H. Quoc Ngo, P. Frenger, and E. G. Larsson, "Ubiquitous cell-free massive MIMO communications," *EURASIP J. Wireless Commun. Netw.*, vol. 2019, no. 1, p. 197, Dec. 2019.

[317] I. F. Akyildiz, C. Han, and S. Nie, "Combating the distance problem in the millimeter wave and terahertz frequency bands," *IEEE Commun. Mag.*, vol. 56, no. 6, pp. 102–108, Jun. 2018.

[318] H. Elayan, O. Amin, B. Shihada, R. M. Shubair, and M.-S. Alouini, "Terahertz band: The last piece of RF spectrum puzzle for communication systems," *IEEE Open J. Commun. Soc.*, vol. 1, pp. 1–32, 2020.

[319] Q. Xia, Z. Hossain, M. J. Medley, and J. M. Jornet, "A link-layer synchronization and medium access control protocol for terahertz-band communication networks," *IEEE Trans. Mobile Comput.*, to be published.

[320] K. Tekbıyık, A. R. Ekti, G. K. Kurt, and A. Görçin, "Terahertz band communication systems: Challenges, novelties and standardization efforts," *Phys. Commun.*, vol. 35, Aug. 2019, Art. no. 100700.

[321] H. Sarieddeen, M.-S. Alouini, and T. Y. Al-Naffouri, "Terahertz-band ultra-massive spatial modulation MIMO," *IEEE J. Sel. Areas Commun.*, vol. 37, no. 9, pp. 2040–2052, Sep. 2019.

[322] G. E. Moore, "Cramming more components onto integrated circuits," *Proc. IEEE*, vol. 86, no. 1, pp. 82–85, Jan. 1998.

[323] S. Cherry, "Edholm's law of bandwidth," *IEEE Spectr.*, vol. 41, no. 7, pp. 58–60, Jul. 2004.

[324] H. Elayan, O. Amin, R. M. Shubair, and M.-S. Alouini, "Terahertz communication: The opportunities of wireless technology beyond 5G," in *Proc. Int. Conf. Adv. Commun. Technol. Netw. (CommNet)*, Apr. 2018, pp. 1–5.

[325] J. W. Fleming, "High-resolution submillimeter-wave Fourier-transform spectrometry of gases," *IEEE Trans. Microw. Theory Techn.*, vol. MTT-22, no. 12, pp. 1023–1025, Dec. 1974.
[326] R. Piesiewicz, T. Kleine-Ostmann, N. Krumbholz, D. Mittleman, M. Koch, J. Schoebei, and T. Kurner, "Short-range ultra-broadband terahertz communications: Concepts and perspectives," *IEEE Antennas Propag. Mag.*, vol. 49, no. 6, pp. 24–39, Dec. 2007.
[327] S. Jia, X. Yu, H. Hu, J. Yu, T. Morioka, P. U. Jepsen, and L. K. Oxenlowe, "120 Gb/s multi-channel THz wireless transmission and THz receiver performance analysis," *IEEE Photon. Technol. Lett.*, vol. 29, no. 3, pp. 310–313, Feb. 1, 2017.
[328] A. Gasiewski, *Applications and Requirements for Environmental Remote Sensing*, document 15-11-0765-00-0thz, IEEE 802.15, Atlanta, GA, USA, Nov. 2011. [Online]. Available: https://mentor.ieee.org/802.15/dcn/11/15-11-0765-00-0thz-remote-sensing-applications-of-thz-bands.pdf
[329] A. Clegg, *Sharing Between Radio Astronomy and Active Services at THz Frequencies*, IEEE 802.15 Document 15-10-0829-00-0thz, Dallas, TX, USA, Nov. 2010. [Online]. Available: https://mentor.ieee.org//802.15/dcn/10/15-10-0829-00-0thz-sharing-between-active-and-passive-services-at-thz-frequencies.ppt
[330] C. Jastrow, K. Münter, R. Piesiewicz, T. Kürner, M. Koch, and T. Kleine-Ostmann, "300 GHz transmission system," *Electron. Lett.*, vol. 44, no. 3, pp. 213–214, 2008.
[331] C. Jastrow, S. Priebe, B. Spitschan, J. Hartmann, M. Jacob, T. Kürner, T. Schrader, and T. Kleine-Ostmann, "Wireless digital data transmission at 300 GHz," *Electron. Lett.*, vol. 46, no. 9, pp. 661–663, 2010.
[332] T. Nagatsuma, H. J. Song, Y. Fujimoto, K. Miyake, A. Hirata, K. Ajito, A. Wakatsuki, T. Furuta, N. Kukutsu, and Y. Kado, "Giga-bit wireless link using 300–400 GHz bands," in *Proc. Int. Top. Meeting Microw. Photon.*, Oct. 2009, pp. 1–4.
[333] S. Priebe, M. Jacob, and T. Kurner, "The impact of antenna directivities on THz indoor channel characteristics," in *Proc. 6th Eur. Conf. Antennas Propag. (EUCAP)*, Mar. 2012, pp. 478–482.
[334] J.-S. Rieh, *Current Status of Semiconductor Technologies and Circuits for THz Applications*, IEEE Standard 802:15-08-0437-00-0thz, Jul. 2008. [Online]. Available: https://mentor.ieee.org/ 802.15/dcn/08/15-08-0437-00-0thz-current-status-of-semiconductortechnologies-and-circuits-for-thz-applications.pdf
[335] R. W. Ridgway, *Millimeter-Wave Photonics for High Data Rate Wireless Communication Systems*, IEEE Standard 802:15-08-0433-00-0thz, Jul. 2008. [Online]. Available: https://mentor.ieee.org/802.15/dcn/08/15-08-0433-00-0thz-millimeter-wave-photonics-for-high-data-rate-wirelesscommunication-systems.pdf
[336] Resolution 950 (Rev.WRC-07). (2007). *Consideration of the Use of the Frequencies Between 275 and 3000 GHz*. [Online]. Available:https://www.itu.int/net/ITU-R/conferences/docs/ties/wrc-res-950-en.pdf
[337] X. Yu, J. Zhang, and K. B. Letaief, "A hardware-efficient analog network structure for hybrid precoding in millimeter wave systems," *IEEE J. Sel. Topics Signal Process.*, vol. 12, no. 2, pp. 282–297, May 2018.
[338] Z. Xu, X. Li, X. Zhao, M. H. Zhang, and Z. Wang, "DSRC versus 4G-LTE for connected vehicle applications: A study on field experiments of vehicular communication performance," *J. Adv. Transp.*, vol. 2017, pp. 1–10, 2017.
[339] J. Lorca, M. Hunukumbure, and Y. Wang, "On overcoming the impact of Doppler spectrum in millimeter-wave V2I communications," in *Proc. IEEE Globecom Workshops (GC Wkshps)*, Dec. 2017, pp. 1–6.

ANTHONY NGOZICHUKWUKA UWAECHIA received the B.Eng. and M.Sc. degrees in electrical and electronic engineering from Ahmadu Bello University, Zaria, Nigeria, in 2006 and 2013, respectively, and the Ph.D. degree in wireless and mobile systems from Universiti Sains Malaysia (USM), Malaysia, in 2018.

He has been a Postdoctoral Research Fellow with the School of Electrical and Electronic Engineering, USM, since 2019. His research interests include signal processing for communications and particularly focusing in the area of digital signal processing, sparse channel estimation, channel measurement, sparse representation, OFDM systems, robust precoding in massive MIMO systems, and mmWave communications.

Dr. Uwaechia was a recipient of the Graduate on Time Award for the completion of the Ph.D. degree in USM, and the Institute of Postgraduate Studies, Graduate Assistant Scheme Award in USM, Penang, Malaysia, during his Ph.D. studies. He was also a recipient of the Nigeria-Sao Tome and Principe Joint Development Postgraduate Scholarship Award during his M.Sc. degree programme.

NOR MUZLIFAH MAHYUDDIN (Member, IEEE) received the B.Eng. degree from Universiti Teknologi Malaysia, Malaysia, in 2005, the M.Sc. degree from Universiti Sains Malaysia, Malaysia, in 2006, and the Ph.D. degree from Newcastle University, Newcastle upon Tyne, U.K., in 2011.

She is currently an Associate Professor with the School of Electrical and Electronic Engineering, Universiti Sains Malaysia, Malaysia. Her research interests are in the field of RF and microwave engineering, reliability, signal integrity, sparse channel estimation, OFDM systems, massive MIMO systems, and mmWave communications.

Dr. Mahyuddin is currently a member of the IEEE Communications Society (ComSoc) and the IET, and a Professional Member of the Association for Computing Machinery (ACM). She is also registered with the Board of Engineers Malaysia (BEM).